UNIVERSITY OF CALIFORNIA SAN DIEGO

Mechanism of Parkinson's Disease-linked LRRK2 Microtubule Binding

A Dissertation submitted in partial satisfaction of the requirements
for the degree Doctor of Philosophy

in

Biology

by

Andrea Marie Dickey

Committee in charge:

Professor Samara L. Reck-Peterson, Chair
Professor Arshad B. Desai
Professor Tracy M. Handel
Professor Andres E. Leschziner
Professor Jill Cathleen Wildonger

2022

The Dissertation of Andrea Marie Dickey is approved, and it is acceptable in quality and form for publication on microfilm and electronically.

University of California San Diego

2022

DEDICATION

This dissertation is dedicated to my family:

my parents, Glenn and Charlene,

and my brother, William.

EPIGRAPH

Biology is the study of complicated things that have the appearance of having been designed with a purpose … The biologist's problem is the problem of complexity. The biologist tries to explain the workings, and the coming into existence, of complex things, in terms of simpler things. He can regard his task as done when he has arrived at entities so simple that they can safely be handed over to physicists.

— Richard Dawkins, *The Blind Watchmaker*

You may not control all the events that happen to you, but you can decide not to be reduced by them.

— Maya Angelou, *Letter to My Daughter*

TABLE OF CONTENTS

LIST OF FIGURES

LIST OF TABLES

LIST OF SUPPLEMENTAL VIDEOS

Video 1**:** KIF1C motility on microtubules.

Video 2: KIF1C motility on microtubules in the presence of Hook3.

Video 3: KIF1C$^{\Delta 794\text{-}807}$ motility on microtubules.

Video 4: KIF1C$^{\Delta 794\text{-}807}$ motility on microtubules in the presence of Hook3.

Video 5: KIF1C motility on microtubules in the presence of Hook3^{Hook2}.

Video 6: Motility of dynein, dynactin and Hook3 on microtubules.

Video 7: Example of motility of dynein, dynactin, Hook3, and KIF1C on microtubules.

Video 8: Example of motility of dynein, dynactin, Hook3, and KIF1C on microtubules.

ACKNOWLEDGEMENTS

Throughout the preparation of this dissertation, I have received an enormous amount of assistance and support.

Firstly, I would like to thank my advisor, Professor Samara Reck-Peterson. I thank her for giving me the freedom to explore my interests and drive my own projects while always keeping me on track to reach my goals and providing the tools to choose the right direction and successfully complete this dissertation. I will always admire her commitment to creating a collaborative and supportive lab environment where scientists like me are not just productive but thrive.

I would like to thank Professor Andres Leschziner for his support. This work would not have been possible without his guidance and collaboration.

I would also like to acknowledge the following people for their support in the research included in this dissertation: (1) The current and former members of the Reck-Peterson and Leschziner labs, including Aga, John, David, Mar, Yu Xuan, Janice, Eva, Salo, Rob, Jenna, Alex, Ameerah, Marta, Jaime, Sataree, Soojin, Swetha, Kavi, Liv, Joey, Jenny, Oscar, James, Adriana, Vinit, Morgan, Rachael, Kelly, and Zaw. Thank you all for your roles in shaping me into the scientist and person I am today. I will forever be grateful for the countless hours of scientific discussion, your friendship, and the joy you have brought to my life. (2) My thesis committee: Professor Arshad Desai, Professor Tracy Handel, Professor Andres Leschziner, Professor Samara Reck-Peterson, and Professor Jill Wildonger.

I would further like to acknowledge the UC San Diego Medical Scientist Training Program, the UC San Diego Department of Biological Sciences, and the Molecular Biophysics Training Grant for their unwavering support.

Finally, this dissertation would also not have been possible without the following people who I would like to thank, in no particular order: my parents, Glenn and Charlene, for their continual support; my brother, William, for his support and inspiration to never give up on my

dreams; my found family in San Diego for being my home away from home and giving me a space to express myself; Grisel, for her unmatched kindness and wisdom; Juan and Sarah, for reaching out no matter the distance between us and for their genuine friendship; and to all those who have accompanied me throughout this journey.

Chapter 2, in full, is a reprint of the material as it appears in Structural basis for Parkinson's Disease-linked LRRK2's binding to microtubules. David M. Snead*, Mariusz Matyszewski*, Andrea M. Dickey*, Yu Xuan Lin, Andres E. Leschziner, Samara L. Reck-Peterson, bioRxiv, 2022. The dissertation author was a co-author of this paper. * denotes equal contributions.

Chapter 3 contains unpublished material that may later be prepared for submission for publication co-authored with Janice Reimer, Yu Xuan Lin, Sebastian Mathea, Dario Alessi, Andres E. Leschziner, and Samara L. Reck-Peterson. The dissertation author was the primary author of this chapter.

Appendix A, in full, is a reprint of the material as it appears in Structural basis for Parkinson's Disease-linked LRRK2's binding to microtubules. David M. Snead*, Mariusz Matyszewski*, Andrea M. Dickey*, Yu Xuan Lin, Andres E. Leschziner, Samara L.Reck-Peterson, bioRxiv, 2022. The dissertation author was a co-author of this paper. * denotes equal contributions.

Appendix B, in part, is a reprint of the material as it appears in Hook3 is a scaffold for the opposite-polarity microtubule-based motors cytoplasmic dynein-1 and KIF1C. Agnieszka A. Kendrick, Andrea M. Dickey*, William B. Redwine*, Phuoc Tien Tran, Laura Pontano Vaites, Monika Dzieciatkowska, J. Wade Harper, Samara L. Reck-Peterson, Journal of Cell Biology, 2019. The dissertation author was a co-author of this paper. * denotes equal contributions.

VITA

2014 Bachelor of Science in Bioengineering, University of California Berkeley

2022 Doctor of Philosophy in Biology, University of California San Diego

ABSTRACT OF THE DISSERTATION

Mechanism of Parkinson's Disease-linked LRRK2 Microtubule Binding

by

Andrea Marie Dickey

Doctor of Philosophy in Biology

University of California San Diego, 2022

Professor Samara Reck-Peterson, Chair

Leucine-Rich Repeat Kinase 2 (*LRRK2*) is one of the most commonly mutated genes in familial Parkinson's Disease (PD). This neurodegenerative disease affects over 10 million people worldwide, and defects in LRRK2 function have also been linked to the sporadic form of the disease. LRRK2 is a large (286 kDa) multi-domain, predominantly cytosolic, protein and has been shown to have roles in membrane trafficking. While a subset of LRRK2 is localized to membranes in cells, LRRK2 has also been shown to colocalize with microtubules and form helical filaments that wrap around the microtubules. Intriguingly, many PD-linked mutations demonstrate an enhanced association with microtubules when expressed in cells. In vitro, microtubule-associated LRRK2 can act as a roadblock for the molecular motor proteins dynein and kinesin. However, many questions remain about the impact this microtubule-associated LRRK2 has on intracellular

transport and how these LRRK2 filaments form. In this dissertation, I present interdisciplinary work investigating the mechanisms by which LRRK2 filament formation occurs. Here, we report a cryo-electron microscopy structure of the catalytic half of LRRK2, containing its kinase, which is in a closed conformation, and GTPase domains, bound to microtubules. We also report a structure of the catalytic half of LRRK1, LRRK2's closest human homolog, which, while structurally similar to LRRK2, is not linked to PD and does not interact with microtubules. Guided by these structures, we identify amino acids in LRRK2's GTPase domain that mediate microtubule binding; mutating them disrupts microtubule binding in vitro and in cells without affecting LRRK2's kinase activity. Overall, this work provides important insights into the basis of LRRK2 binding to microtubules and presents novel mutants that will enable future work to better probe the physiological roles of the LRRK2/microtubule interaction in the pathogenesis of PD. Our results have implications for the design of therapeutic LRRK2 kinase inhibitors.

CHAPTER 1: INTRODUCTION

1.1 Background

In the early 2000s, *PARK8/LRRK2*, the gene encoding for leucine-rich repeat kinase 2 (LRRK2), was first linked to familial Parkinson's disease (PD)[1,2]. PD is a complex, progressive neurodegenerative disease whose symptoms, in part, are driven by the loss of dopaminergic neurons in the substantia nigra in the midbrain[3]. It is the second most common neurodegenerative disease, affecting an estimated 1-2% of people over 60 worldwide[4]. The major risk factor for PD is age, and key clinical features of this disease include motor deficits, rigidity, bradykinesia (slowness of movement), and tremor. First described in 1817 by James Parkinson[5], over 200 years later, this disease remains incurable, and the pathophysiology remains incompletely understood.

While the majority of cases of PD are idiopathic or sporadic, approximately 10% of cases are caused by familial genetic mutations. Mutations in the *LRRK2* gene are some of the most common causes of autosomally inherited PD, with at least nine missense mutations in *LRRK2* appearing to be sufficient to cause PD and many others affecting PD risk[6]. More recently, mutations in *LRRK2* have also been associated with increased risk for the sporadic form of the disease[7,8]. Pathogenic PD-linked mutations have been shown to lead to activation of LRRK2's kinase, and increased kinase activity of wild-type LRRK2 has also been observed in idiopathic cases of PD[9–13]. As such, LRRK2 has emerged recently as a promising target of disease-modifying PD therapeutics. At the time of writing this dissertation, LRRK2-specific kinase inhibitors have been developed and are in clinical trials (clinicaltrials.gov). Since its discovery, a considerable amount of effort has gone into uncovering the cellular functions of this complex protein; however, limitations in tools to study this protein have left many questions unanswered related to its molecular and cellular functions.

In addition to PD, LRRK2 has also been genetically linked to other human diseases. LRRK2 has been implicated in chronic inflammatory conditions, Crohn's disease (CD) and Hansen's disease (also known as leprosy), and cancer[14–17], suggesting that LRRK2 may also have important roles outside the central nervous system.

1.2 LRRK2 enzymatic activity and function

LRRK2 is a large (286 kDa) multi-domain protein with several protein-protein interactions domains, such as its amino-terminal repetitive protein interaction motifs (armadillo, ankyrin, and leucine-rich repeats (LRR)) and its carboxy-terminal WD40 domain. Between these domains, LRRK2 has two enzymatic domains, a Ras-like GTPase (Ras of complex, or ROC) and a kinase domain that are linked by a structural domain (carboxy-terminal of ROC, or COR) (Fig. 1.1a).

To date, most work investigating LRRK2's enzymatic functions has focused on its kinase activity. LRRK2 is a serine-threonine kinase that is capable of autophophorylating[12] itself in addition to other cellular substrates. Phosphoproteomics have recently revealed that a subset of small Rab GTPases are physiological substrates of LRRK2, including Rab3A/B/C/D, Rab8A/B, Rab10, Rab12, Rab29, Rab35, and Rab43[11]. LRRK2's GTPase activity has been less well characterized; however, there is evidence that there is crosstalk between the GTPase and kinase[18–25]. Dimerization of LRRK2 is required for maximal LRRK2 kinase activity[26], and the GTPase domain is proposed to be involved in regulating the switch between monomeric and dimeric forms of LRRK2[6].

While it remains unclear how LRRK2 drives PD, the best evidence for LRRK2's cellular functions points to a role in membrane trafficking[27–29]. Mutations in LRRK2 cause defects in trafficking of endosomes, lysosomes, autophagosomes, and mitochondria, and LRRK2 regulates lysosomal morphology[30–33]. The physiological substrates of LRRK2, Rab GTPases, are master regulators of membrane trafficking[34], and phosphorylation by LRRK2 has been shown to alter ciliogenesis[34–36] and endolysosomal trafficking[29]. In addition, LRRK2 has been linked to the

cytoskeleton, the tracks upon which membranous cargos are moved within the cell[37–40]. LRRK2 has been implicated in processes such as neurite outgrowth and the formation of cilia and centrosomes[41–44].

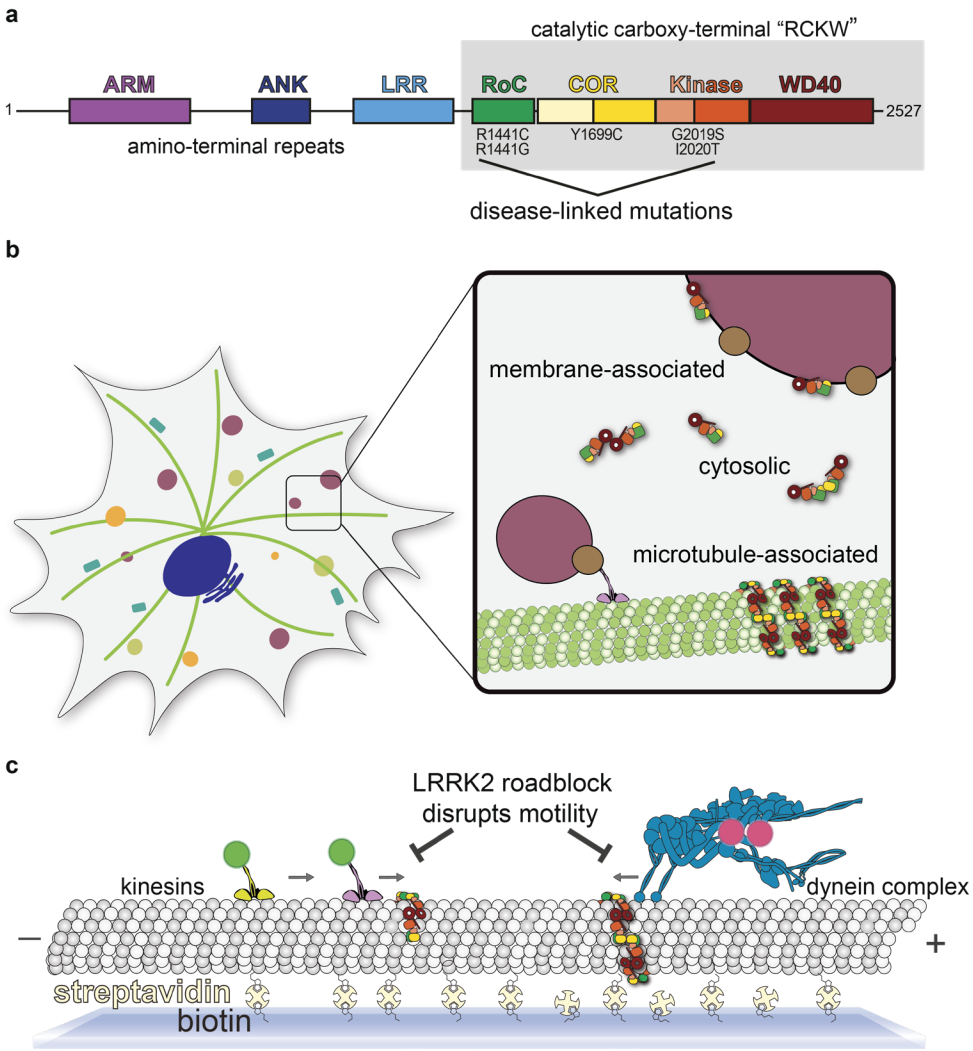

Figure 1.1: LRRK2 is a multi-domain protein found in various subcellular pools.
a, Primary structure of LRRK2 depicting the five major Parkinson's disease-linked mutations. Previous work showed the carboxy-terminal half of LRRK2 (LRRK2^{RCKW}) is sufficient to form microtubule-associated filaments in vitro (Deniston et al. 2020) and this construct was used in the biochemical studies presented here. **b,** LRRK2 is found in various subcellular pools. The majority of LRRK2 in the cell is found in the cytosol, however, LRRK2 can also associate with microtubules and membranes under some circumstances. LRRK2 is shown in cartoon form. This figure is adapted from Leschziner and Reck-Peterson, 2021. **c,** Purified LRRK2^{RCKW} binds to microtubules independent of other factors and can act as roadblocks for molecular motors in vitro. In single-molecule motility assays, fluorescently-labeled molecular motors are visualized walking along coverslip-tethered microtubules using total internal reflection fluorescence microscopy.

1.3 Subcellular localization of LRRK2

LRRK2's cellular functions remain largely unknown; this is, in part, due to technical limitations in the field that have resulted in a reliance on overexpression systems to study LRRK2 in cells. LRRK2 has very low expression levels in most cell types making a direct assessment of endogenous LRRK2 elusive. Very few studies have convincingly visualized endogenous levels of LRRK2 using microscopy, which is further complicated by studies indicating that early antibodies used to visualize LRRK2 lack specificity[45]. Thus far, there is strong evidence that, while the majority of LRRK2 is found in the cytosol, in some circumstances, LRRK2 may also be associated with membranes and microtubules in cells (Fig. 1.1b).

The vast majority of LRRK2 is found in the cytoplasm[35,46], where it can exist in a monomer or dimer state and interacts with homodimers of 14-3-3 proteins. 14-3-3 proteins are small adaptor proteins that are highly expressed in the brain and are thought to stabilize LRRK2 folding via binding to phosphorylated residues in LRRK2's ankyrin, LRR, and ROC domains[46–50]. Phosphorylation of these same residues have also been shown to be related to LRRK2 kinase activity[50].

LRRK2 has also been observed on various membranes within the cell, including membrane-bound vesicles and the *trans*-Golgi network[29]. An estimated 10% of LRRK2 in the cell is associated with membranes where it forms dimers and phosphorylates Rabs[41,46,51]. LRRK2's recruitment to membranes is seen in macrophage and microglial cells lines with stimulation of toll-like receptors by lipopolysaccharide (LPS), as well as with rapamycin treatment, which initiates autophagocytosis in these cells[51]. In addition, Rab29 has been shown to activate LRRK2 kinase activity and recruitment to the *trans*-Golgi network in the context of overexpression systems[35,52]. However, there are still many open questions regarding how membrane association leads to LRRK2 activation, though it seems that the identity of the membrane is not important for kinase activation[36].

Finally, LRRK2 has been strongly linked to the cytoskeleton and binds microtubules in cells under some conditions. Microtubules (MTs) are filamentous, polar structures, composed of tubulin dimers that act as tracks along which molecular motors traffic cargoes throughout the cell. When overexpressed in cells, LRRK2 has been shown to colocalize with microtubules and form filamentous structures[10,37]. Intriguingly, many PD-linked mutations demonstrate an enhanced association with microtubules[18,37]. It has also been well established that pharmacological inhibition with Type 1 kinase inhibitors causes rapid and reversible recruitment of LRRK2 to microtubules[18,53,54]. Furthermore, microtubule-associated LRRK2 can act as a roadblock (Fig. 1.1c), interfering with the motor motility of both dynein and kinesin motors in vitro[39]. These motors are responsible for the long-distance transport of Rab-marked vesicles throughout the cells, and these molecular motors can also bind directly or indirectly to some Rabs[55]. Though the physiological relevance of direct interaction between microtubules and LRRK2 remains to be established, it is clear that LRRK2 plays a role in regulating transport along these intracellular tracks.

1.4 Structure of LRRK2

Despite the growing interest in targeting LRRK2 and the development of small molecule therapeutics, until recently, very little was known about LRRK2 structure and function. Prior to 2020, structural information about LRRK2 was limited, with only two high-resolution structures of human LRRK2 published, one of the isolated ROC domain[56] and one of the WD40 domain[57]. In addition, though structures of full-length LRRK2 had been previously reported, resolution was limited and prevented the description of LRRK2 at a chemical level[58,59].

Recent studies reporting on the structures of soluble[39,60] and microtubule-associated LRRK2[38] have provided major steps forward in our understanding of this enigmatic protein (Fig.2a). Firstly, a 3.5Å structure of the carboxy-terminal half of LRRK2 ($LRRK2^{RCKW}$) showed that

the catalytic half of the protein forms a J-shape that places the kinase and GTPase domains in close proximity[39]. Subsequently, a 3.5Å structure of full-length LRRK2 revealed that the amino-terminal repeat domains wrap around the catalytic half of the protein in what appears to be an autoinhibited conformation[60]. In addition, using *in situ* cryo-electron tomography (cryo-ET), a 14Å structure of microtubule-associated full-length LRRK2 (I2020T) revealed that LRRK2 can oligomerize into helical filaments wrapping around the microtubule[38]. The cryo-ET map was used

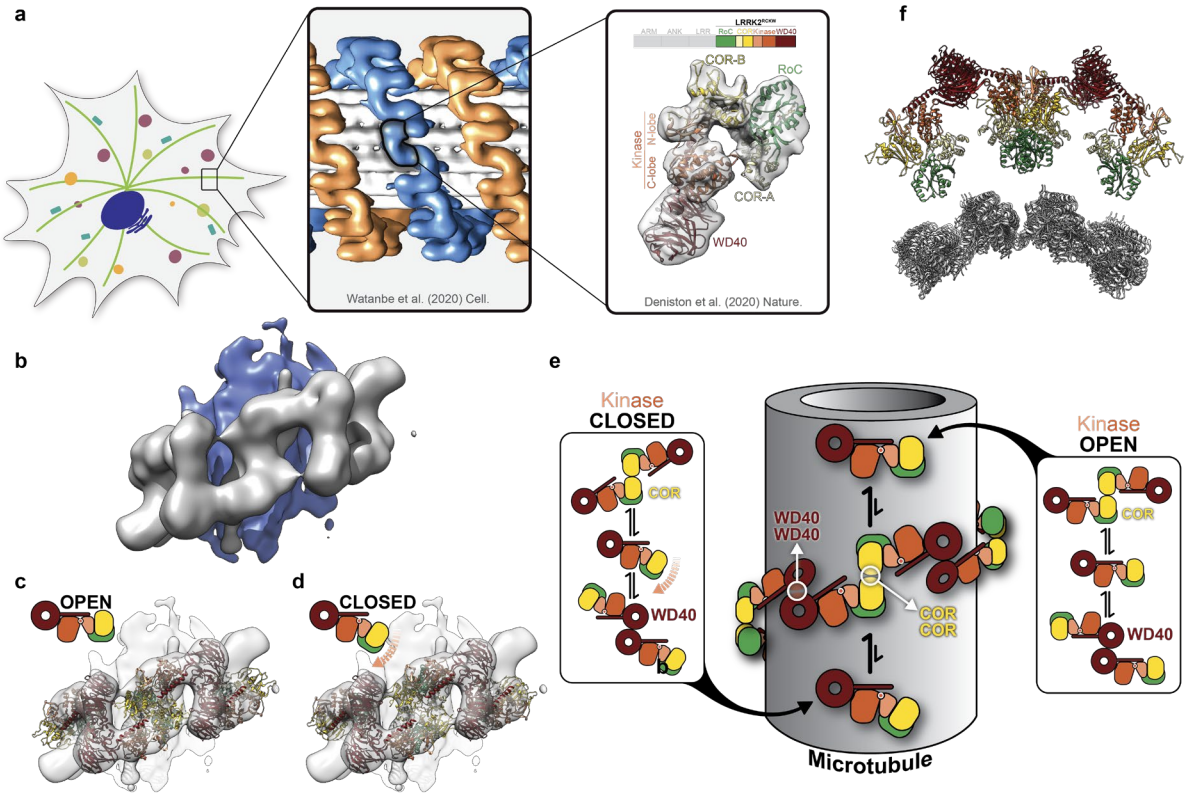

Figure 1.2: Structural studies of LRRK2 and modelling of MT-associated filaments. **a, b,** A 14 Å cryo-ET map of a segment of microtubule-associated LRRK2 filaments in cells. The LRRK2 filament is shown in grey and microtubule in blue. **c,** Fitting of the LRRK2^{RCKW} structure, which has its kinase domain in the open conformation, into the cryo-ET map shown in (b). **d,** Fitting of the closed-kinase model of LRRK2^{RCKW} into the cryo-ET map shown in (b). Closing of the kinase domain significantly reduced clashes at dimer interfaces compared to the open kinase modeled in (c). **e,** Schematic of hypothesis for microtubule-associated LRRK2 filaments presented in Denison et al. (2020). The LRRK2 kinase can be in an open or closed conformation with the kinase-closed form of LRRK2 favoring oligomerization onto microtubules. **f,** Molecular model of microtubule-associated LRRK2RCKW filaments resulting from docking a fragment of the microtubule structure into the corresponding density in the sub-tomogram average in (b). This figure is adapted from Deniston et al. (2020) and Watanbe et al. (2020).

to guide integrative modeling, resulting in a molecular model for the carboxy-terminal half of LRRK2 bound to microtubules[39]. In order to fit the high-resolution LRRK2^{RCKW} structure into the tomographic density, the kinase had to be modeled in the closed conformation[39] (Fig.2b-d). This resulted in a proposed model by which LRRK2's kinase had to be in the closed conformation in order for filaments to form[39] (Fig. 2e). Based on the fact that the ROC GTPase domain points toward the microtubule surface (Fig. 2f), it was suggested that this domain mediates binding to microtubules. However, no direct contact density between the ROC domain and tubulin was observed in the cryo-ET map[38]. Additionally, the pitch and handedness of the right-handed LRRK2 filaments does not match the underlying left-handed tubulin lattice, suggesting the microtubule may act as a non-specific scaffold for LRRK2 filament formation[38,39]. Protomer interfaces in the filament structure were shown to be mediated by successive COR/COR and WD40/WD40 interfaces[39], though the overall resolution was too low to model with confidence the specific residues involved. Despite these insights, the structural basis for the formation of LRRK2 filaments and how they interact with microtubules were not clear.

1.5 Outstanding questions and summary of dissertation

The overarching goal of the work presented in this dissertation is to understand the mechanisms by which LRRK2 filaments form on microtubules. Though this interaction is robust in overexpression systems, the physiological implications of this interaction are still unknown. The ability to perturb LRRK2's association with microtubules will be critical for understanding the implications of the LRRK2/microtubule interaction in the pathogenesis of PD. The subject of chapter 2 is to summarize the current state of our findings on the molecular interactions important for LRRK2 microtubule association[61]. Using reconstituted MT-associated LRRK2 filaments in vitro with purified MTs and LRRK2^{RCKW}, we obtained a higher resolution structure of these filaments that shows clear connecting density between LRRK2^{RCKW} and tubulin, as well as more detailed structural information about the protomer interfaces. Guided by this new filament structure, we

have been able to identify residues in LRRK2 that are important for its association with microtubules. We found that the homotypic dimer interfaces of LRRK2 are essential for the formation of microtubule-bound LRRK2 filaments in cells. We further identified basic residues within LRRK2's ROC domain that are necessary for the binding of LRRK2 to microtubules both in vitro and in cells. With these tools, we will now be able to further dissect the importance of LRRK2-microtubule binding in health and disease and isolate different populations of LRRK2 within the cell to study the various functions of this complex protein. In chapter 3, we address plans to explore the importance of LRRK2's binding to microtubules in cells and answer the outstanding question: what is the function of microtubule-associated LRRK2 in cells? We also discuss structure-guided studies of LRRK1, LRRK2's closest homolog, which is not linked to PD but to its own set of human diseases. Comparative studies between these two Roco family proteins (proteins that contain a combination of a GTPase and kinase[62]) will be critical in elucidating how and why LRRK1 and LRRK2 mechanistically differ and will help delineate how LRRK proteins are involved in the pathogenesis of their associated diseases.

CHAPTER 2: STRUCTURAL BASIS FOR PARKINSON'S DISEASE-LINKED LRRK2'S BINDING TO MICROTUBULES

2.1 Contributions

Mariusz Matyszewski collected and processed the LRRK2 cryo-EM data. David M. Snead and Mariusz Matyszewski collected and processed the LRRK1 cryo-EM data. Yu Xuan Lin, David M. Snead, Andrea M. Dickey and Mariusz Matyszewski purified proteins for Cryo-EM and biochemistry experiments. David M. Snead and Andrea M. Dickey performed the biochemical and single-molecule assays with the help of Yu Xuan Lin. Andrea M. Dickey performed the cellular assays. Samara L.Reck-Peterson. and Andres E. Leschziner. directed and supervised the research.

2.2 Abstract

Leucine Rich Repeat Kinase 2 (*LRRK2*) is one of the most commonly mutated genes in familial Parkinson's Disease (PD). Under some circumstances, LRRK2 co-localizes with microtubules in cells, an association enhanced by PD mutations. We report a cryo-electron microscopy structure of the catalytic half of LRRK2, containing its kinase, which is in a closed conformation, and GTPase domains, bound to microtubules. We also report a structure of the catalytic half of LRRK1, which is closely related to LRRK2, but is not linked to PD. LRRK1's structure is similar to LRRK2, but LRRK1 does not interact with microtubules. Guided by these structures, we identify amino acids in LRRK2's GTPase domain that mediate microtubule binding; mutating them disrupts microtubule binding in vitro and in cells, without affecting LRRK2's kinase activity. Our results have implications for the design of therapeutic LRRK2 kinase inhibitors.

2.3 Introduction

Parkinson's Disease (PD) is the second most common neurodegenerative disease, affecting over 10 million people worldwide. Autosomal dominant missense mutations in Leucine

Rich Repeat Kinase 2 (*LRRK2*) are a major cause of familial PD[1,2,63,64], and mutations in *LRRK2* are also linked to sporadic cases of PD[7,8]. All PD-linked mutations in LRRK2 increase its kinase activity[9–12]and increased LRRK2 kinase activity in the context of a wild-type protein is also associated with sporadic cases[13]. LRRK2-specific kinase inhibitors have been developed to treat PD and are in clinical trials (clinicaltrials.gov).

While it remains unclear how LRRK2 drives PD, LRRK2 has been functionally linked to membrane trafficking[27–29]. Mutant LRRK2 causes defects in endo/lysosomal, autophagosomal, and mitochondrial trafficking[65–69], and LRRK2 regulates lysosomal morphology[30–33]. Although the bulk of LRRK2 is found in the cytosol, it can also associate with membranes under some conditions[30,31,35,36,46]. A subset of Rab GTPases, which are master regulators of membrane trafficking[34], are phosphorylated by LRRK2, and PD-linked LRRK2 mutations increase Rab phosphorylation in cells[11,41]. Phosphorylation of Rabs by LRRK2 is linked to alterations in ciliogenesis[34–36] and defects in endolysosomal trafficking[29]. LRRK2 also co-localizes with microtubules in cells and in vitro[37–40]. Cellular localization of LRRK2 with microtubules is seen with elevated expression levels and this is enhanced by Type-1 LRRK2-specific kinase inhibitors[37–39,70,71]. In vitro, the catalytic half of LRRK2 alone can bind to microtubules[39]. In addition, many PD-linked mutations (R1441C, R1441G, Y1699C, and I2020T) increase microtubule association in cells[37,70]. It is currently not understood how LRRK2 perturbs cellular trafficking or how the cellular localization of LRRK2—cytosolic, membrane-associated, and/or microtubule-bound—contributes to its function and to PD pathology. Developing tools that control the localization of LRRK2 in cells will be crucial for determining LRRK2's cellular function and for understanding the molecular basis of PD.

To develop such tools, structural information about LRRK2 is essential. LRRK2 is a large, multidomain protein (Fig. 2.1a). The amino-terminal half contains armadillo, ankyrin, and leucine-rich repeat domains. The carboxy-terminal half contains LRRK2's enzymatic domains—both a Roco family GTPase (Ras-Of-Complex, or ROC domain) and a kinase—as well as a scaffolding

domain (C-terminal Of Roc, or COR) and a WD40 protein interaction domain. The COR domain is further subdivided into COR-A and COR-B moieties. Here we refer to the catalytic half of LRRK2 as LRRK2^{RCKW}, named for its ROC, COR, kinase and WD40 domains. Recent structures of LRRK2 have revealed the architecture of LRRK2 at near-atomic resolution[39,60]. A 3.5Å structure of LRRK2^{RCKW} showed that LRRK2's catalytic half is J-shaped, placing the kinase and GTPase domains in close proximity[39]. Later, a 3.5Å structure of full-length LRRK2 revealed that the N-terminal half of LRRK2 wraps around its enzymatic half, with the leucine rich repeats blocking the kinase's active site in what appears to be an autoinhibited state[60]. In addition to these structures of soluble LRRK2, a 14Å structure of LRRK2 carrying the I2020T PD mutation bound to microtubules in cells was obtained using cryo-electron tomography (cryo-ET)[38]. The cryo-ET map was used to guide integrative modeling, leading to a molecular model for the enzymatic half of LRRK2 bound to microtubules[38]. This model was refined when the 3.5Å cryo-EM structure of LRRK2's catalytic half was docked into the cryo-ET structure[38]. In these models the C-terminal half of LRRK2 (LRRK2^{RCKW}) wraps around the microtubule using two dimerization interfaces, one between WD40 domains and the other between COR-B domains[39]. In addition, in the models the ROC GTPase domain faces the microtubule, although the cryo-ET structure did not reveal any direct interactions between LRRK2 and the microtubule[38]. An isolated ROC domain has also been shown to interact with alpha and beta-tubulin heterodimers[72].

To investigate the possible functional consequences of LRRK2's interaction with microtubules, we previously looked at the impact of LRRK2 on the movement of microtubule-based motor proteins in vitro[39]. Dynein and kinesin motors move on microtubules, with dynein moving in one direction (towards the microtubule minus end) and kinesin generally moving in the opposite direction (towards the microtubule plus end). Both dynein and kinesin motors interact with their membranous cargos directly or indirectly via connections to Rab GTPases, including those Rabs phosphorylated by LRRK2[73–76]. Using single-molecule assays, we showed that low nanomolar concentrations of LRRK2^{RCKW} blocked the movement of both dynein and kinesin on

microtubules[39]. Furthermore, we showed that the conformation of LRRK2's kinase domain was critical for this effect[39]. LRRK2 predicted to have its kinase domain "closed" (the canonical active conformation) by LRRK2-specific Type-1 kinase inhibitors blocked motility[39], in agreement with studies showing that these inhibitors enhance the association of LRRK2 with microtubules in cells[37–39,70,71]. In contrast, LRRK2 no longer robustly blocked the movement of dynein or kinesin when its kinase domain was predicted to be in an "open" or inactive conformation (in the presence of Type-2 kinase inhibitors)[39].

Despite these insights, the structural basis for the formation of LRRK2 filaments and how they interact with microtubules remains unknown. Here, we report a range of cryo-EM structures capturing different levels of detail of the microtubule-bound filaments formed by the C-terminal half of LRRK2 (LRRK2^{RCKW}). By focusing our refinements, we were able to resolve the kinase at 4.5Å resolution, the interactions between the ROC domain and the microtubule at 5.0Å, and a LRRK2^{RCKW} tetramer revealing dimerization interfaces at 5.9Å. Our structure reveals direct interactions between LRRK2's ROC domain and the microtubule. We show that microtubule binding is mediated by electrostatic interactions and requires the negatively charged, glutamate rich carboxy-terminal tubulin tails. We also present a 5.8Å map of the carboxy-terminal half of LRRK1 (LRRK1^{RCKW}), LRRK2's closest human homolog. Despite the structural similarity to LRRK2^{RCKW}, we show that LRRK1^{RCKW} does not bind to microtubules. Based on our structure of microtubule-bound LRRK2^{RCKW} and a comparison of our LRRK2^{RCKW} and LRRK1^{RCKW} structures, we identify microtubule-facing basic amino acids that are only conserved in LRRK2's ROC domain and are required for LRRK2's interaction with microtubules in vitro and in cells. Mutation of these amino acids reduces LRRK2's ability to block the movement of kinesin motors in vitro. Together, our work reveals the structural basis for LRRK2's ability to form filaments and interact with microtubules and identifies mutations that perturb LRRK2's ability to form filaments and localize to microtubules in cells. These are essential tools for determining the cellular functions of LRRK2 and for the further development of therapeutic LRRK2 kinase inhibitors.

2.4 Results

Cryo-EM structure of microtubule-associated LRRK2^{RCKW}

To understand, structurally and mechanistically, how LRRK2 oligomerizes around and interacts with microtubules, we set out to obtain a higher resolution structure of microtubule-associated LRRK2 filaments using an in vitro reconstituted system and single-particle cryo-EM approaches. We chose to work with LRRK2^{RCKW} because it is sufficient to from filaments in vitro[39] and it accounted for the density observed in the cryo-ET reconstruction of full-length LRRK2 filaments in cells[38].

As previously observed[39], copolymerization of tubulin with LRRK2^{RCKW}—either wild type (WT), or carrying the PD-linked mutations G2019S or I2020T—yielded microtubules decorated with LRRK2^{RCKW} (Fig. A.1a). Diffraction patterns calculated from images of these filaments showed layer lines indicating the presence of ordered filaments (Fig. A.1a). In the presence of MLi-2 we saw an additional layer line of lower frequency for all three constructs, suggesting that the filaments had longer-range order (Fig. A.1a). Unlike WT and G2019S, I2020T showed this additional layer line in the absence of MLi-2 as well (Fig. A.1a). Given these observations, we chose to focus on the LRRK2^{RCKW} [I2020T] filaments formed in the presence of MLi-2 for our cryo-EM work. The symmetry mismatch between microtubules, which are polar left-handed helices, and the LRRK2 filaments, which are right-handed and have pseudo-two-fold axes of symmetry perpendicular to the microtubule, required that we largely uncouple their processing (Fig. A.1b,c and Methods). Our cryo-EM analysis resulted in several maps originating from an initial reconstruction of the filaments (Fig. 2.1b): a map of a LRRK2^{RCKW} tetramer that includes density for two microtubule protofilaments (6.6Å) (Fig. 2.1c); a higher resolution map of the same LRRK2^{RCKW} tetramer that excludes the microtubule (5.9Å) (Fig. A.3g-i); maps of pseudo-two-fold symmetry-related LRRK2^{RCKW} monomers along a filament that face either the minus (“-“) (5.2Å) or plus (“+”) (5.0Å) end of the microtubule, which revealed their different contacts with the

microtubule (Fig. 2.1e,f and Fig. A.1c); and a consensus structure of LRRK2^{RCKW} that gave the highest resolution for the kinase domain (4.5Å) (Fig. A.1c).

The LRRK2^{RCKW} filaments are formed by two different homotypic dimer interfaces, involving either COR-B:COR-B or WD40:WD40 interactions (Fig. 2.1c), in agreement with what had been predicted by modeling[38,39]. Each interface has a pseudo-two-fold axis of symmetry perpendicular to the microtubule axis. The ROC domain points toward and contacts the microtubule (Fig. 2.1c-f). Interestingly, our in vitro reconstituted filaments of LRRK2^{RCKW} differ from

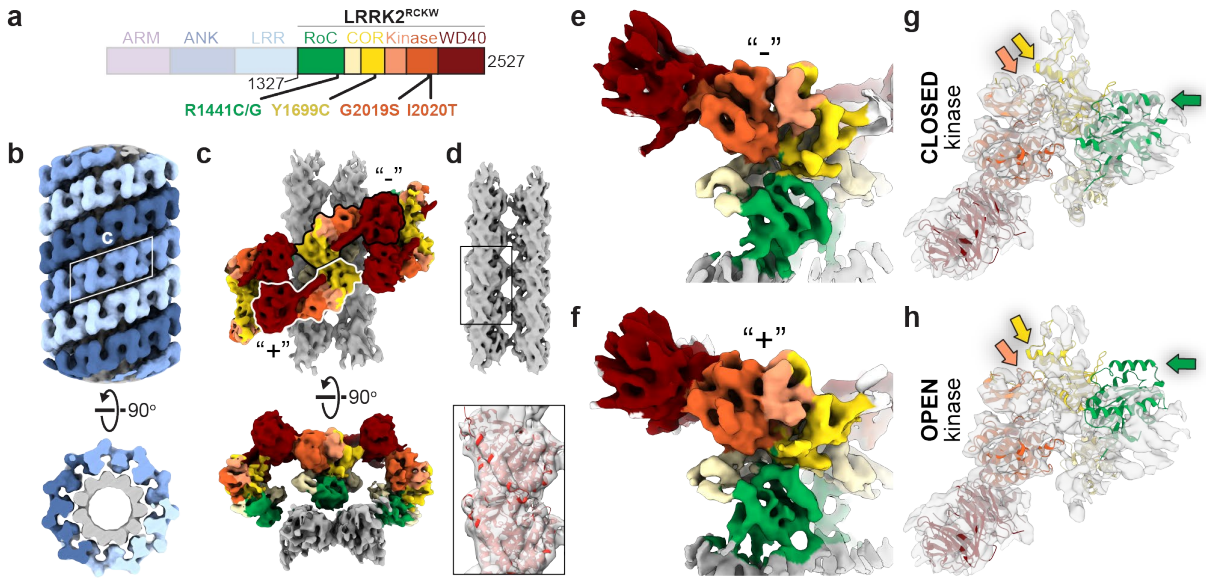

Figure 2.1: Cryo-EM structure of microtubule-associated LRRK2^{RCKW}[I2020T].
a, Primary structure of LRRK2. The N-terminal half of LRRK2, absent from the construct used in our cryo-EM studies, is shown in dim colors. The same color-coding of domains is used throughout the Article. **b,** Helical reconstruction (18Å) of LRRK2^{RCKW}[I2020T] filaments bound to a microtubule in the presence of MLi-2. The three LRRK2^{RCKW}[I2020T] helices are indicated in different shades of blue. **c,** Cryo-EM reconstruction (6.6Å) of a LRRK2^{RCKW} tetramer and associated microtubule (2 protofilaments), as indicated by the white rhomboid in (b). **d**, Focused refinement of the microtubule in (c) to improve its resolution and determine its polarity. An α/β tubulin dimer (from PDB: 6O2R) was docked into the density (black rectangle and inset below). **e,f,** Focused refinement of the "-" (5.2Å) and "+" (5.0Å) LRRK2^{RCKW}[I2020T] monomers (as labeled in (c)). **g,** The LRRK2^{RCKW} domains (ROC, COR-A, COR-B, Kinase N-lobe, Kinase C-lobe, WD40) (PDB:6VNO) were fitted individually into the 4.5 Å cryo-EM map. **h,** The full LRRK2^{RCKW} model (PDB:6VNO) was aligned to the C-lobe of the kinase as docked in (g). The colored arrows in (g) and (h) point to parts of the model (PDB:6VNO) that fit into the cryo-EM density when domains are docked individually, allowing the kinase to be closed, (g) but protrude from it when the full model is used, which has its kinase in an open conformation (h).

those formed by full length LRRK2 in cells[38], with LRRK2^{RCKW} forming a triple (rather than double) helix, with the strands packed closer together. Despite these differences, the pitch of the helix is the similar in both cases (see Methods and Table A.2).

We previously hypothesized that LRRK2's kinase must adopt a closed conformation to form filaments around microtubules[39]. Our current structure agrees with this prediction (Fig. 2.1g,h). To determine whether the closed conformation of the kinase was a consequence of the presence of MLi-2, which would be expected to stabilize that state, we solved a structure of microtubule-associated LRRK2^{RCKW} filaments in its absence (Fig. A.2). Although these filaments are less well ordered than those formed in the presence of MLi-2 (Fig. A.1a) and thus resulted in a lower resolution reconstruction (7.0Å), the final map still fit a closed-kinase model of LRRK2^{RCKW} better than its open form (Fig. A.3a,b). Finally, the conformation of the kinase in the microtubule-associated LRRK2^{RCKW}[I2020T] filaments appears to be somewhat more closed than that predicted by AlphaFold[77,78] for the active state of full-length LRRK2 (Fig. A.3c-f). We cannot determine at this point whether this difference is a consequence of the absence of the amino-terminal half of LRRK2, the presence of the I2020T mutation in our filaments, a small difference in the AlphaFold modeling, or a consequence of the formation of the filaments themselves.

It was previously proposed that the ROC domain would mediate binding of LRRK2 to microtubules due to its proximity to the microtubule surface in the cryo-ET map of the filaments in cells[30]. However, no density was seen connecting the ROC domain, or any other domain, to the microtubule in the cryo-ET map[38]. In contrast, our cryo-EM map showed clear density connecting LRRK2^{RCKW} and the microtubule (Fig. 2.1e,f). As mentioned above, the polar nature of the microtubule means that the ROC domains, which would otherwise be related by a two-fold symmetry axis perpendicular to the microtubule, are in different local environments. In agreement with this, their connections to the microtubule only became apparent when LRRK2^{RCKW} monomers were refined individually (Fig. 2.1c and e,f, and Fig. A.1).

LRRK2's dimer interfaces are important for microtubule association

We next sought to examine in more detail the role played by the WD40- and COR-B-mediated dimer interfaces in LRRK2's ability to associate with microtubules. To build a model of the LRRK2^{RCKW} filament we used rigid-body docking of individual domains from the LRRK2^{RCKW} structure (PDB: 6VNO)[39] (Fig. 2.2a, b). This revealed WD40:WD40 and COR-B:COR-B interfaces very similar to those seen previously with isolated WD40 domains[57], full-length LRRK2 COR-B:COR-B dimers[60], and LRRK2^{RCKW} dimers in the absence of microtubules[39]. However, small differences exist when domains (ROC, COR-A/B and the N-lobe of the kinase), individually fitted into our cryo-EM map of the filaments, are compared with the corresponding portion of the COR-B-mediated dimer of full-length-LRRK2[60] (Fig. A.3g-j). It remains to be seen whether these differences are due to the absence of the N-terminal half of LRRK2 in the microtubule-associated filaments, or to small conformational changes associated with filament formation.

Based on our model, we made mutants designed to disrupt both interfaces and then tested their ability to form filaments in cells and to bind microtubules or inhibit the motility of kinesin in vitro. At the WD40:WD40 interface we mutated leucine 2343 or serine 2345 to aspartic acid (L2343D or S2345D; Fig. 2.2a), designed to introduce a charge clash. At the COR-B:COR-B dimer interface we mutated arginine 1731 to leucine or aspartic acid (R1731L or R1731D; Fig. 2.2b), designed to disrupt the salt bridge with glutamic acid 1681. All mutant alleles expressed similarly to WT LRRK2 when transfected into 293T cells (Fig. A.4a,b,d,e). We also tested to each mutant for its ability to phosphorylate Rab10 in cells and found that the WD40 dimerization interface mutants had no effect on LRRK2's kinase activity, while the COR-B dimerization interface mutants elevated it by ~2X (Fig. A.4c,f). Next, we tested the ability of these mutations to disrupt filament formation by full-length LRRK2 (WT except for the interface mutations) in cells, which is induced by MLi-2[39,70,71] (Fig. 2.2c and Fig. A.4a,d). As previously shown, mutation of either the WD40:WD40 interface[38] or the COR-B:COR-B interface[60] reduced filament formation in cells. We found that S2345D, R1731L and R1731D all significantly decreased MLi-2-induced

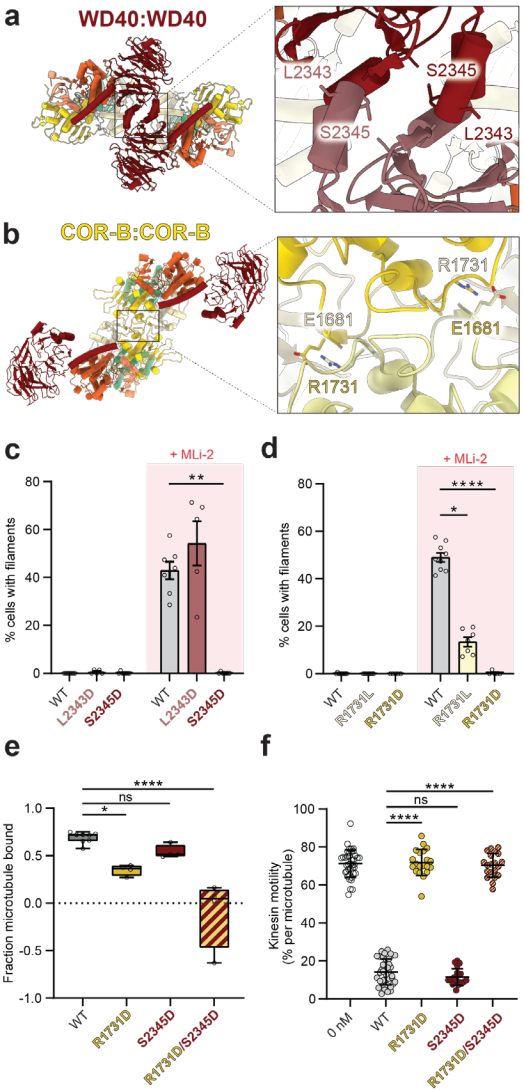

Figure 2.2: Effect of mutations in LRRK2's WD40 and COR-B domains on filament formation and microtubule binding.

a, b, Dimer interfaces (WD40:WD40 and COR-B:COR-B) involved in filament formation, and location of residues tested in this work. **c,** Effect of mutations in residues in the WD40 domain (L2343D or S2345D) that have been shown to reduce dimerization of the isolated domain in vitro on the formation of MLi-2-induced filaments in cells. Cells (293T) were treated with MLi-2 (500 nM) or DMSO as a control for 2 h. Data are mean ± s.e.m. **p=0.0076, Kruskal-Wallis test with Dunn's post hoc for multiple comparisons. **d,** Effect of mutations (R1731L/D) in a residue at the COR-B:COR-B interface on the formation of MLi-2-induced filaments in cells. Data are mean ± s.e.m. *p=0.0205, ****p<0.0001, Kruskal-Wallis test with Dunn's post hoc for multiple comparisons. **e,** Effect of mutations in the WD40 and/or WD40 and COR-B domains on the binding of $LRRK2^{RCKW}$ to microtubules in a pelleting assay. Tubulin concentration was 0.700 µM. Box and whisker plot center line denotes the median value, whiskers denote min and max values. *p=0.0111, ****p<0.0001, one-way ANOVA with Dunnett's multiple comparisons test. **f,** Effect of mutations in the WD40 or WD40 and/or COR-B domains on the inhibition of kinesin motility in vitro by 50 nM $LRRK2^{RCKW}$. Inhibition of kinesin motility was quantified as percentage of motile events per microtubule. Data are mean ± s.d. ****p<0.0001, Kruskal-Wallis test with Dunn's post hoc for multiple comparisons.

LRRK2 filament formation, with S2345D and R1731D completely abolishing our ability to detect filaments in cells (Fig. 2.2c,d). Surprisingly, although the L2343D mutation was previously shown to decrease dimerization in the context of a purified WD40 domain[57] it did not reduce the formation of LRRK2 filaments in the presence of MLi-2 (Fig. 2.2c).

Next, we examined the effects of the mutations at the LRRK2 dimerization interfaces on LRRK2's ability to bind microtubules or inhibit kinesin motility in vitro. To investigate LRRK2's ability to bind microtubules in vitro, we incubated pure LRRK2^{RCKW} with in vitro assembled, taxol-stabilized microtubules and quantified the fraction of LRRK2 that pelleted with microtubules after centrifugation. While a point mutation at the WD40 dimerization interface (S2345D) did not affect LRRK2^{RCKW}'s ability to pellet with microtubules, a point mutation at the COR-B interface (R1731D) reduced microtubule binding by about 50% (Fig. 2.2e and Fig. A.4g). Combining these mutations (R1731D/S2345D) largely abolished LRRK2^{RCKW}'s interaction with microtubules (Fig. 2.2e and Fig. A.4g). Cryo-EM imaging of microtubules incubated with the different mutants agreed with the binding data: we observed the layer lines diagnostic of filament formation with LRRK2^{RCKW}[S2345D], but not with the R1731D or R1731D/S2345D mutants (Fig. A.4h). Previously, we showed that low nanomolar concentrations of LRRK2^{RCKW} blocked the movement of dynein and kinesin motors in vitro[39]. To determine if the dimerization interfaces are required for this inhibitory effect, we monitored the motility of single GFP-tagged human kinesin-1 ("kinesin" here) molecules using total internal reflection fluorescence (TIRF) microscopy. As in the microtubule binding experiments, we found that a single point mutation at the WD40 dimerization interface (S2345D) blocked kinesin motility similarly to wild-type LRRK2^{RCKW}, while a single mutant at the COR-B interface (R1731D) or the double mutant designed to disrupt both dimerization interfaces (R1731D/S2345D) no longer inhibited kinesin motility in vitro (Fig. 2.2f and Fig. A.4i,j). Importantly, 2D averages from cryo-EM images of LRRK2^{RCKW}[R1731D/S2345D] showed that the mutations do not significantly alter the structure of the protein (Fig. A.4k).

Electrostatic interactions drive binding of LRRK2^{RCKW} to microtubules

We next sought to test the hypothesis that binding of LRRK2 to microtubules is mediated by electrostatic interactions between the negatively charged surface of the microtubule and basic residues in LRRK2's ROC domain. In addition to the observed charge complementarity between our model of the LRRK2 filaments and the microtubule (Fig. 2.3a and Deniston et al.[39]), other data support this hypothesis: (1) the symmetry mismatch between microtubules and the LRRK2 filaments suggests that there cannot be a single LRRK2-microtubule interface[38], (2) the cryo-ET reconstruction of filaments in cells showed no clear direct contact between LRRK2 and tubulin[38], and (3) the connections in our reconstruction only became apparent when LRRK2^{RCKW} monomers were refined individually (Fig. 2.1c and e,f, and Fig. A.1). To directly test this hypothesis, we developed a fluorescence-based assay to monitor binding of LRRK2^{RCKW} to microtubules in vitro. To do this, we randomly chemically labeled primary amines of LRRK2^{RCKW} with BODIPY TMR-X ("TMR" here) and used widefield fluorescence microscopy to quantify the association of TMR-LRRK2^{RCKW} with Alexa Fluor 488-labeled microtubules tethered to a coverslip. Chemical labeling did not significantly impair LRRK2^{RCKW} kinase activity as assessed by Rab8a phosphorylation in vitro (Fig. A.4l,m). In our indirect assay of filament formation, TMR-LRRK2^{RCKW} also inhibited the microtubule-based motility of kinesin (Fig. A.4n). Titration of increasing concentrations of TMR-LRRK2^{RCKW} to microtubules led to a dose-dependent increase in microtubule binding (Fig. 2.3b,c). Notably, LRRK2^{RCKW} binds to microtubules at low nanomolar concentrations, in agreement with our previous observations that low nanomolar concentrations of LRRK2^{RCKW} inhibit the motility of kinesin and dynein[39]. Unlabeled LRRK2^{RCKW} also binds microtubules in a bulk microtubule co-sedimentation assay (Fig. A.4o,p).

To determine whether electrostatic interactions contribute to the binding of LRRK2^{RCKW} to microtubules, we tested the effect of increasing concentrations of sodium chloride on this binding. We observed a dose-dependent decrease in microtubule binding (Fig. 2.3d and Fig. A.4q). We

also observed a salt-dependent decrease in microtubule binding for unlabeled LRRK2^{RCKW} as measured by bulk co-sedimentation with microtubules (Fig. A.4o,p).

Tubulin carries an overall negative charge, and the disordered, negatively charged, glutamate-rich carboxy-terminal tails of tubulin are known to contribute to microtubule binding by many microtubule-associated proteins[79]. We tested the contribution of the tubulin tails to the LRRK2^{RCKW}-microtubule interaction by removing them with the protease subtilisin, which cleaves tubulin near its carboxy-terminus[80]. Cleavage of tubulin tails decreased LRRK2^{RCKW}'s ability to

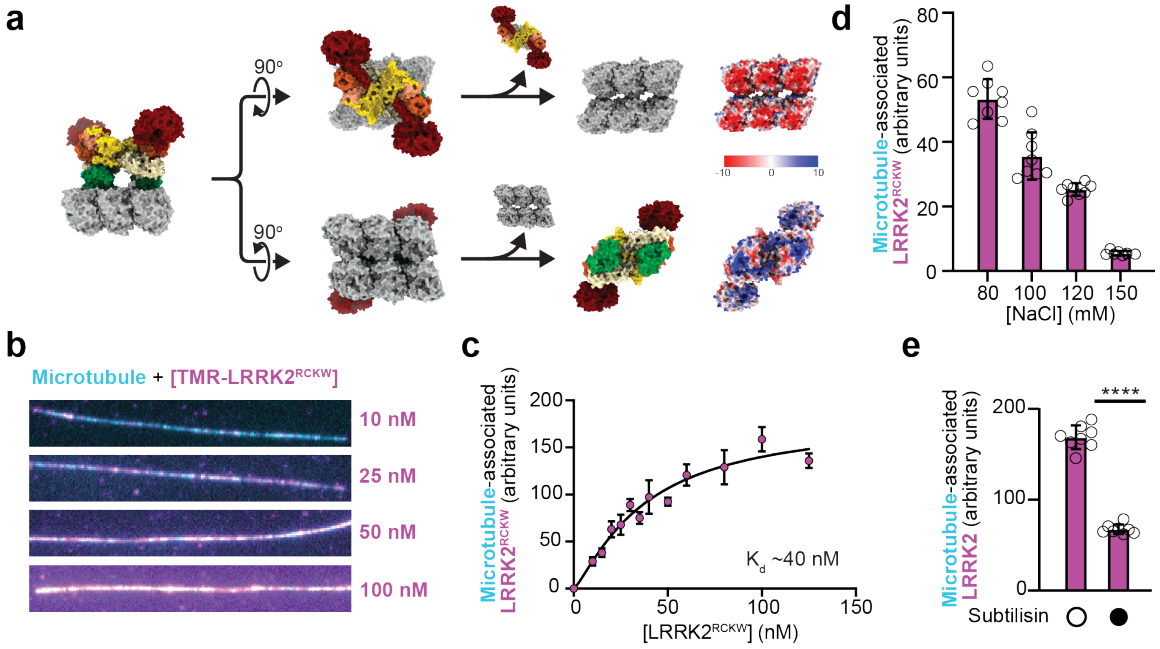

Figure 2.3: LRRK2^{RCKW} interacts with the microtubule via electrostatic interactions. **a,** Charge distribution in the molecular model for microtubule-associated LRRK2^{RCKW} filaments (Fig. 2.1). The model is shown in surface representation on the left and is then split to reveal the microtubule surface facing LRRK2^{RCKW} (top) or the LRRK2^{RCKW} surface facing the microtubule (bottom). The Coulomb potential of those surfaces is shown on the right. The acidic C-terminal tubulin tails that further contribute negative charge density to the microtubule are disordered in our structure and not included here. **b,** Representative images of randomly labeled TMR-LRRK2^{RCKW} (magenta), bound to microtubules labeled with Alexa Fluor 488 and tethered to a coverslip (cyan). The concentrations of TMR-LRRK2^{RCKW} are indicated on the right. **c,** Quantification of data represented in (b). Images were flatfield corrected, average TMR-fluorescence intensity was measured along each microtubule in a given field of view, and an average value per field of view was calculated, normalized for microtubule length. Data are mean ± s.d., n=8 fields of view. **d,** Binding of 100 nM TMR-LRRK2^{RCKW} to microtubules in the presence of increasing concentrations of sodium chloride, quantified from the assay exemplified by (b). **e,** Binding of 50 nM TMR-LRRK2^{RCKW} to microtubules untreated or pre-treated with subtilisin, quantified from the assay exemplified by (b). Data are mean ± s.d., n=8 fields of view. ****p<0.0001, unpaired t-test with Welch's correction.

bind microtubules by ~50% (Fig. 2.3e and Fig. A.4r). Together, these results show that LRRK2's interaction with the microtubule is driven by electrostatic interactions and is mediated in part by the carboxy-terminal tails of tubulin.

LRRK1^{RCKW} adopts a similar overall fold to LRRK2^{RCKW}

To home in on specific residues in LRRK2 that might be important for mediating its interaction with microtubules, we used a comparative approach with its closest homolog, LRRK1. While LRRK2 has been linked to both familial and sporadic PD[1,2,63,64,7,8], LRRK1 is not clinically associated with PD[81], but instead is implicated in metabolic bone disease and osteopetrosis[82–85]. Many of LRRK1's domains are relatively well conserved with LRRK2, with 41%, 48%, 46%, and 50% similarity between the leucine-rich repeat (LRR), ROC, COR, and kinase domains, respectively. The amino- and carboxy-termini of LRRK1 and LRRK2 are more divergent; LRRK1 lacks the amino-terminal armadillo repeats, and it is unclear based on sequence analyses whether LRRK1, like LRRK2, contains a WD40 domain, with only 27% sequence similarity in this region.

We began by solving a structure of LRRK1 using cryo-EM (Fig. 2.4a and Fig. A.5a). To do so, we expressed and purified the amino acids in LRRK1 that corresponded to LRRK2^{RCKW} (residues 631 to 2015; referred to as LRRK1^{RCKW}; Fig. 2.4a). The resolution of the LRRK1^{RCKW} monomer (5.8Å) was limited by the same strong preferred orientation we had observed for the LRRK2^{RCKW} monomer[39]. While LRRK2^{RCKW} forms trimers, which allowed us to solve its high-resolution structure[39], we saw no evidence of trimer formation by LRRK1^{RCKW}. Our structure, obtained in the presence of GDP but in the absence of ATP, shows that LRRK1^{RCKW} adopts a similar overall J-shaped domain organization as that of LRRK2^{RCKW} and does contain a WD40 domain (Fig. 2.4a,b). Our map revealed that the αC helix in the N-lobe of LRRK1's kinase is ~4 turns longer than that in LRRK2 (Fig. 2.4c), a feature that was correctly predicted by the AlphaFold[77,78] model of LRRK1. Our structure also revealed a density corresponding to a carboxy-terminal helix extending from the WD40 domain and lining the back of the kinase domain, as is

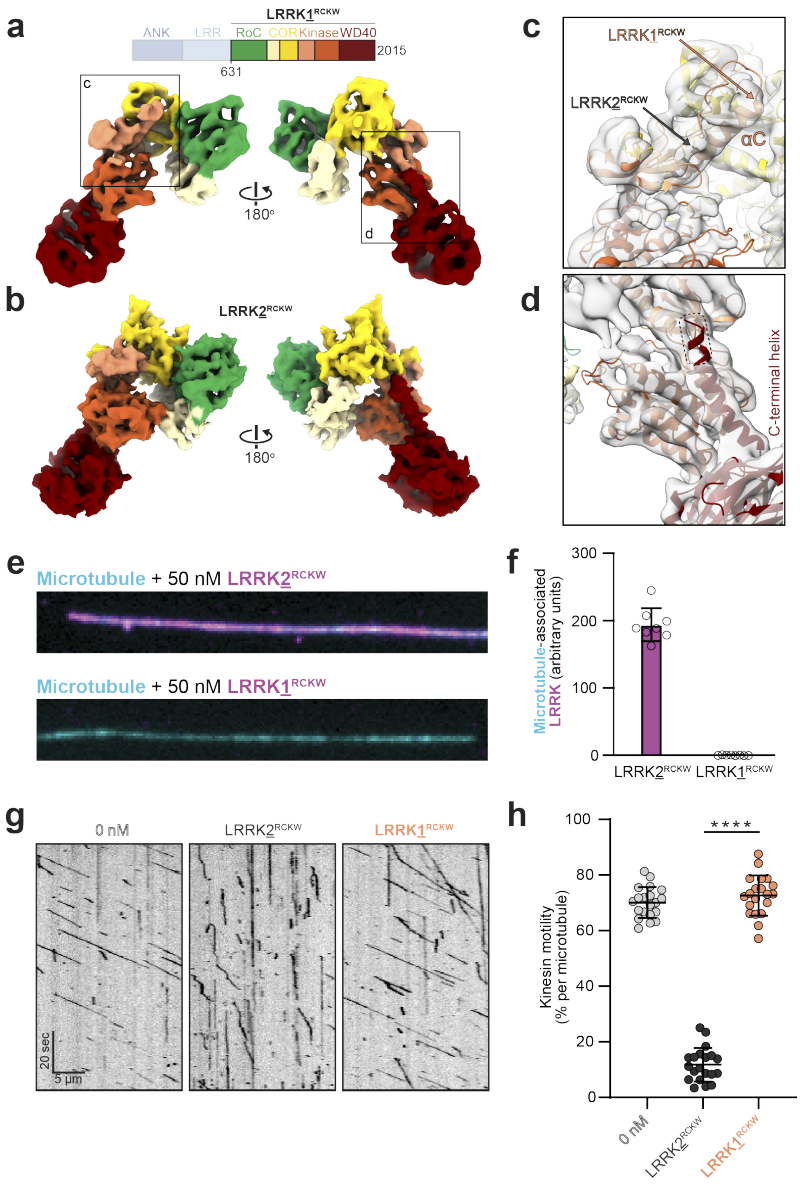

Figure 2.4: LRRK1^{RCKW} is structurally similar to LRRK2^{RCKW} but does not bind to microtubules.

a, Cryo-EM map (5.8Å) of a LRRK1^{RCKW} monomer, with domains colored according to the scheme shown above. **b,** The molecular model for LRRK2^{RCKW} (PDB:6VNO) is shown as a calculated 6Å density (molmap command in ChimeraX), in the same orientations used for LRRK1^{RCKW} in (a). **c,d,** Close ups of the LRRK1^{RCKW} map shown in (a) with the AlphaFold model of LRRK1 docked into it. These close ups highlight the difference in length in the αC helix between LRRK1 and LRRK2 (c), and a difference between our experimental map of LRRK1^{RCKW} and the AlphaFold model of LRRK1 (d). **e,** Representative images of Alexa Fluor 488-labeled microtubules (cyan) incubated with 50nM of either LRRK2^{RCKW} (magenta, top) or LRRK1^{RCKW} (magenta, bottom). **f,** Quantification of data exemplified by (e), as outlined in Figure 2.3, above. Data are mean ± s.d., n=8 fields of view. **g,** Example kymographs for single-molecule kinesin motility assays alone or in the presence of 100nM of either LRRK2^{RCKW} or LRRK1^{RCKW}. **h,** Quantification of data exemplified by (g) as percentage of motile kinesin events per microtubule. Data are mean ± s.d. ****p<0.0001, Kruskal-Wallis test with Dunn's post hoc for multiple comparisons.

the case for LRRK2, but the LRRK1 carboxy-terminal helix appears to be shorter (Fig. 2.4d). Our map disagrees with the LRRK1 structure predicted by AlphaFold, which has a longer C-terminal helix (Fig. 2.4d). The significance of this difference is not clear at this time as the AlphaFold structure was modeled in the active conformation (closed kinase), while our cryo-EM map of LRRK1^{RCKW} is in an inactive, open kinase conformation and lacks the N-terminal repeats. At the current resolution, LRRK2^{RCKW} and LRRK1^{RCKW} are otherwise very similar, confirming that the overall domain organization is conserved between these two proteins.

LRRK1^{RCKW} does not bind microtubules

Given the structural similarity between LRRK1 and LRRK2 (Fig. 2.4a,b), we wondered whether LRRK1 could also bind microtubules. To assess this, we randomly chemically labeled LRRK1^{RCKW} with BODIPY TMR-X and used widefield fluorescence microscopy to quantify microtubule-binding in vitro. We did not observe association of TMR-LRRK1^{RCKW} with microtubules (Fig. 2.4e,f), suggesting that, unlike LRRK2^{RCKW}, LRRK1^{RCKW} does not bind microtubules. As an alternative way of testing LRRK1^{RCKW}'s binding to microtubules, we measured the effect of unlabeled LRRK1^{RCKW} on kinesin motility. Unlike LRRK2^{RCKW}, LRRK1^{RCKW} had no effect on kinesin motility even at a concentration of 100nM, consistent with its inability to bind microtubules (Fig. 2.4g,h and Fig. A.5b). In addition, unlabeled LRRK1^{RCKW} did not co-sediment with microtubules (Fig. A.5c,d). Together these data show that, in contrast to LRRK2, LRRK1 does not interact with microtubules.

Basic residues in LRRK2's ROC domain are important for microtubule binding

Next, we sought to use our discovery that LRRK1^{RCKW} and LRRK2^{RCKW} share a similar overall structure, but only LRRK2^{RCKW} binds microtubules, to identify specific amino acids in LRRK2 that are important for microtubule binding. A sequence alignment of LRRK1 and LRRK2 revealed several basic patches in LRRK2 that are not well conserved in LRRK1 (Fig. A.5e). These

basic patches create a positively charged surface on the part of LRRK2's ROC domain facing the microtubule that is absent in LRRK1 (Fig. 2.5a,b). The patches correspond to residues 1356-1359 (KTKK in human LRRK2), 1383-1386 (KRKR in human LRRK2), and 1499-1502 (KLRK in human LRRK2). In our highest resolution maps, where we refined individual LRRK2^{RCKW} monomers in the filament and their contacts with the microtubule (Fig. 2.1e,f), the strongest density connecting LRRK2^{RCKW} to tubulin involves the 1356-1359 and 1383-1386 basic patches (Fig. 2.5c and Fig. A.5f). To determine if these basic patches are required for LRRK2's interaction with microtubules, we mutated two basic residues to alanine in each patch in the context of LRRK2^{RCKW} (K1358A/K1359A or R1384A/K1385A) and tested the mutants' ability to bind to microtubules in vitro. Both mutants showed a significant decrease in microtubule binding in a microtubule co-sedimentation assay compared with wild-type LRRK2^{RCKW} (Fig. 2.5d). We also tested the ability of LRRK2^{RCKW}[K1358A/K1359A] to inhibit kinesin motility in vitro (Fig. 2.5e and Fig. A.5g,h) and found that it showed a significant reduction in its inhibition compared to wild-type LRRK2^{RCKW}. Finally, we introduced full-length GFP-LRRK2 carrying either of the two basic patch mutations into human 293T cells and quantified microtubule-association in the absence or presence of MLi-2. In the absence of MLi-2, all three constructs (wild-type and the two basic patch mutants) formed little or no filaments in cells (Fig. 2.5f and Fig. A.5i). Treatment with MLi-2 resulted in the appearance of filaments in a significant percentage of cells carrying wild-type LRRK2 but failed to induce filament formation in cells carrying the basic patch mutants (Fig. 2.5f and Fig. A.5i). We also tested whether GFP-LRRK2 carrying the PD-linked I2020T mutation, which is known to result in filament formation in cells in the absence of MLi-2[39,70,71] (Fig. 2.5g), is sensitive to a basic patch mutation. Indeed, GFP-LRRK2[I2020T] no longer formed microtubule-associated filaments in cells when also carrying the K1358A/K1359A mutation (Fig. 2.5g and Fig. A.5j). In agreement with our data on microtubule binding in vitro and filament formation in cells, cryo-EM imaging of microtubules incubated with LRRK2^{RCKW} carrying either of the two basic patch mutants did not show the layer lines diagnostic of filament formation (Fig. A.4h). Class averages

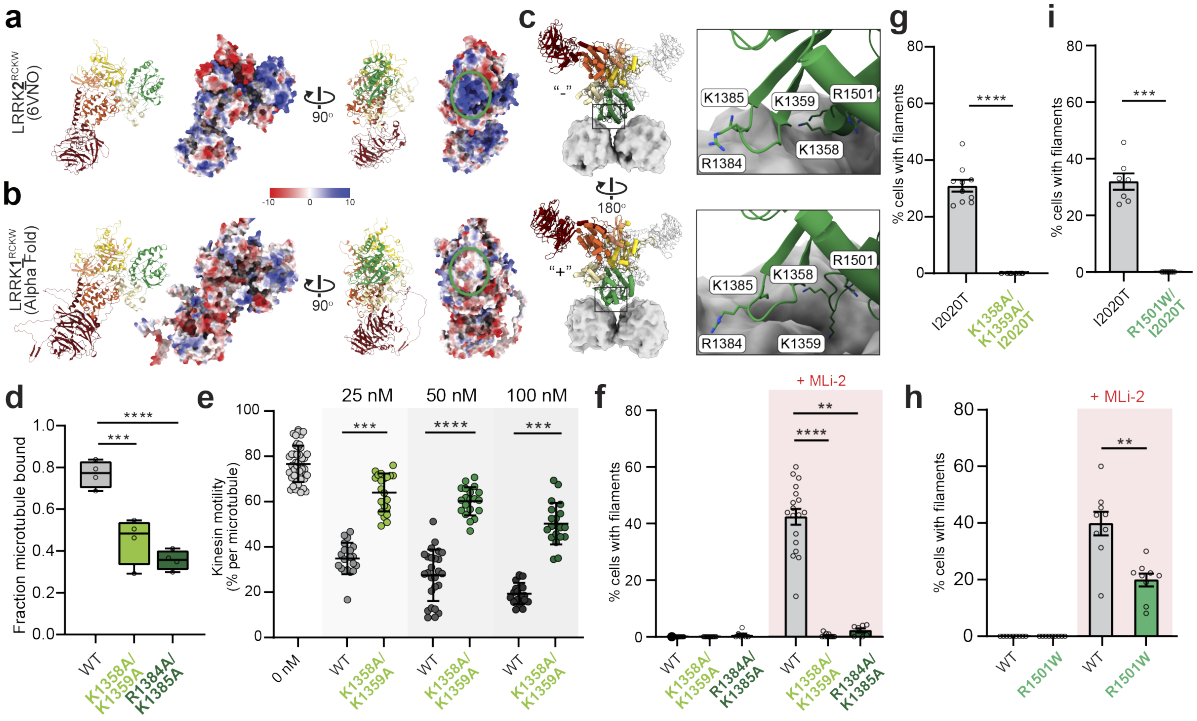

Figure 2.5: Basic patches in the ROC domain are involved in LRRK2's binding to microtubules.

a,b, Surface charge distribution (Coulomb potential) for LRRK2^{RCKW} (PDB:6VNO) (a) and the AlphaFold model for LRRK1 (b). The green oval on the right highlights the region in the ROC domain, which faces the microtubule in the filament structure, where basic patches are present (and conserve) in LRRK2 but absent in LRRK1. **c,** Molecular model of the microtubule-bound LRRK2^{RCKW} filament with tubulin shown in surface representation. "Top" and "bottom" show the two monomers in a dimer, along with close ups highlighting basic residues near the microtubule surface tested here. **d,** Binding of LRRK2^{RCKW}, wild-type or carrying mutations in the ROC domain's basic patches, to microtubules using a pelleting assay. Tubulin concentration was 0.432 μM. Box and whisker plot center line denotes the median value, whiskers denote min and max values.***p=0.0006, ****p<0.0001, one-way ANOVA with Dunnett's multiple comparisons test. **e,** Single-molecule motility assays for kinesin alone or in the presence of increasing concentrations of LRRK2^{RCKW}, either wild-type or carrying mutation in the ROC domain. Inhibition of kinesin motility was quantified as percentage of motile events per microtubule. Data are mean ± s.d. ***p=0.0001, ****p<0.0001, ***p=0.0002, Kruskal-Wallis test with Dunn's post hoc for multiple comparisons. **f,** Quantification of microtubule-associated filament formation in cells for wild-type or basic patch mutant GFP-LRRK2 in the absence or presence of MLi-2. DMSO was used as a control for MLi-2. Data are mean ± s.e.m. **p=0.0022, ****p<0.0001, Kruskal-Wallis test with Dunn's post hoc for multiple comparisons. **g,** Quantification of microtubule-associated filament formation in cells expressing GFP-LRRK2(I2020T) and basic patch mutant GFP-LRRK2[K1358A/K1359A/I2020T]. Data are mean ± s.e.m. ***p<0.0001, Mann-Whitney test. **h,** Same as for (f) for a recently identified PD-linked mutation in the ROC domain (R1501W). Data are mean ± s.e.m. **p=0.0017, Mann-Whitney test. **i,** Same as for (g) for GFP-LRRK2[I2020T] and GFP-LRRK2[R1501W/I2020T]. Data are mean ± s.e.m. ***p=0.0002, Mann-Whitney test.

from cryo-EM images of those mutants also showed that the mutations do not significantly alter the structure of the protein (Fig. A.4k).

While none of the most common PD-linked mutations in LRRK2 are found in these basic patch regions, the recently reported R1501W variant[86] is found in the ROC domain facing the microtubule, near the basic patches we identified (Fig. 2.5c). To determine whether R1501W alters LRRK2's interaction with microtubules we expressed GFP-LRRK2[R1501W] in 293T cells. In the presence of MLi-2, LRRK2[R1501W] showed a ~50% reduction in the fraction of cells containing microtubule-bound filaments compared to wild-type LRRK2 (Fig. 2.5h and Fig. A.5k). While the effect of the R1501W mutation was milder than that of the basic patch mutations in the context of wild-type LRRK2, it was as extreme as the basic patch mutants when combined with the I2020T mutation, where it also abolished filament formation (Fig. 2.5i and Fig. A.5j).

Importantly, none of the effects described above are due to changes in protein expression levels (Fig. A.5l) or to changes in the kinase activity of LRRK2 (Fig. A.5l,m). The basic patch mutants and R1501W all show similar levels of Rab10 phosphorylation in cells compared with wild-type LRRK2, and they do not alter the increased Rab10 phosphorylation seen in the context of I2020T (Fig. A.5l,m).

2.5 Discussion

Here we report a structure of LRRK2^{RCKW} filaments bound to microtubules. Our structure (4.5Å in the best parts of our map) was obtained by reconstituting the filaments in vitro using pure components and is of much higher resolution than a previously reported cryo-ET structure of LRRK2 filaments bound to microtubules in cells (14Å)[38]. This new structure allowed us to build better models of the WD40:WD40 and COR-B:COR-B dimerization interfaces and it confirmed our previous proposal that filament formation by LRRK2 requires its kinase to be in a closed (active) conformation[39]. This provides a structural explanation for the observation that LRRK2-specific Type 1 kinase inhibitors, which are expected to stabilize the closed conformation of the

kinase, induce filament formation in cells[38,39,71]. We also report a structure of the catalytic half of LRRK1 (LRRK1^{RCKW}), LRRK2's closest homologue. While of modest resolution (5.8Å), this structure shows that the overall fold of the ROC, COR, Kinase and WD40 domains, and their spatial arrangement, are similar in both LRRK proteins. We also undertook a comparative analysis of the two proteins with respect to microtubule interactions. We found that LRRK1 does not bind to microtubules in vitro, while LRRK2 does so with high affinity (K_d ~ 40 nM). As shown previously[38], the ROC domain of LRRK2 faces the microtubule in the filament. By comparing the sequences and structures of LRRK1^{RCKW} and LRRK2^{RCKW} we identified several microtubule-facing basic patches in the ROC domain of LRRK2 that are not well conserved in LRRK1. These basic patches were in regions where we observed density connecting LRRK2^{RCKW} to the microtubule in our cryo-EM map. We discovered that mutating two basic amino acids in LRRK2's ROC domain was sufficient to block microtubule binding both in cells and in vitro. We also showed that a PD-linked variant (R1501W)[86], which is located in the same region of the ROC domain, decreased microtubule binding in cells. Together, this work provides important insights and tools for probing the cellular function and localization of LRRK2 and for designing LRRK2-specific kinase inhibitors.

The symmetry mismatch between the LRRK2 filaments and the microtubule, first seen in the cryo-ET reconstruction of the filaments in cells[38], remains one of the most striking features of the structure. The previous reconstruction, at 14Å, did not show any density connecting LRRK2 to the microtubule; therefore, how the two interacted despite the symmetry mismatch remained a mystery. The higher resolution of our map, and our ability to process LRRK2^{RCKW} monomers individually, allowed us to show that LRRK2^{RCKW} monomers that are related by (pseudo)two-fold symmetry in the filament are indeed not truly symmetric and interact with the microtubule differently. This explains why those connections had not been seen before; any processing that imposes helical symmetry to the filaments would average out non-symmetric features. Understanding whether these differences in the interaction with the microtubule translate into other changes throughout LRRK2 will require higher resolutions. Higher resolutions would also

allow us to determine whether filament formation alters the structure of LRRK2 relative to its soluble forms; the fact that rigid body docking of domains into our map led to small, but detectable differences with either soluble LRRK2 dimers[60] or the AlphaFold predicted LRRK2 structure[78] suggests this could be the case.

A major difference between our structure of microtubule bound LRRK2^{RCKW} filaments in vitro and that of LRRK2 filaments in cells was in the number and closeness of those filaments; filaments in cells were double-helical while those we presented here are triple-helical and packed closer together. Despite these differences, the helical parameters are very similar between the structures, suggesting that the underlying structure of the filaments is similar as well. The most likely explanation for the differences is the absence of the amino-terminal repeats in our structure of the LRRK2^{RCKW} filaments. Although disordered and absent from the final map, the amino-terminal half of LRRK2 was present in the filaments reconstructed in cells[38]. Placing the AlphaFold model of LRRK2 into the cryo-ET map of filaments in cells showed major clashes between the filament itself (formed by the RCKW domains) and the amino-terminal repeats (Fig. A.6). Therefore, the filaments could not form unless the amino-terminal repeats were undocked from the rest of the protein, explaining why they were not visible in the cryo-ET map. Their presence, albeit in a flexible state, could explain the larger spacing, and thus lower number of helices, seen in LRRK2 vs LRRK2^{RCKW} filaments; the disordered amino-terminal repeats could act as “spacers” that prevent the filaments from packing closer together.

Although we could visualize the connections between LRRK2’s ROC domain and the microtubule in our reconstruction, its resolution is not high enough to build a model into the density. We identified key residues in this interaction by comparing, at the structural and sequence level, LRRK1^{RCKW} and LRRK2^{RCKW}. The structure of LRRK1^{RCKW}, although of modest resolution, revealed that the two proteins are very similar. Key differences in the charge distribution on the ROC domain facing the microtubule, and the observation that LRRK1^{RCKW} does not interact with microtubules in our assays, provided a path for identifying mutations that could abolish

microtubule binding in LRRK2 without affecting its structure or kinase activity. These will be invaluable tools to probe the significance of microtubule binding by LRRK2 in relevant cell types. Finally, the general features of the filaments—their curvature and basic patches facing a negatively charged surface (the microtubule)—raise the possibility that a similar geometry could be involved in the interaction between LRRK2 and membranes.

The data we presented here suggest that LRRK2 can bind microtubules without forming filaments, which we would define as oligomers that are long enough to completely wrap around a microtubule. The data also indicate that this binding mode is likely to be the preponderant one at the low concentrations we use in our in vitro single-molecule assays. These observations stem from comparing the ability of mutants designed to disrupt dimerization interfaces (COR-B and WD40) to bind microtubules and inhibit kinesin motility in vitro, and to form filaments in cells. Any mutant that completely abolishes a dimerization interface would allow LRRK2 to form dimers (via the other interface) but would prevent the formation of longer oligomers. While mutants predicted to break either the COR-B (R1731D) or WD40 (S2345D) interfaces abolished formation of LRRK2 filaments in cells, their effects on microtubule binding in vitro were far less extreme, with R1731D resulting in a ~50% decrease and S2345D having no significant effect. It should be noted that the S2345D mutant likely does not fully disrupt the WD40 interface since it is able to form some filaments, albeit less well-ordered ones, under the high concentrations used for cryo-EM. The mutants' affinity for microtubules correlates with their ability to inhibit kinesin motility: R1731D is unable to inhibit the motor, while S2345D inhibits motility as much as WT does. Taken together, these data suggest that small LRRK2 oligomers, as small as a dimer, could act as roadblocks for microtubule-based transport. This possibility, along with the fact that Type 1 inhibitors stabilize the conformation of LRRK2 that favors microtubule binding, should be taken into account when designing LRRK2 inhibitors.

While LRRK2 readily binds microtubules at low concentrations in vitro, whether LRRK2 binds to and/or forms filaments around microtubules in cells expressing endogenous levels of

LRRK2 remains an open question. Although the only reports of LRRK2 interacting with microtubules in cells so far have been under overexpression conditions[18,37,39,68,71], only a limited number of cell types have been imaged for LRRK2 localization and to our knowledge there are no reports of live-cell imaging of endogenous LRRK2. Thus, an important future goal will be to determine the localization and dynamics of LRRK2 expressed at endogenous levels in PD-relevant cell types. A recent report suggests that a noncoding *LRRK2* PD variant leads to increased *LRRK2* expression in induced-microglia[87]. In addition, *LRRK2* expression levels are elevated in a variety of immune cells in PD patients compared to age matched healthy controls[88,89]. These findings raise the possibility that increased expression of wild-type *LRRK2* could be linked to PD. Our finding that the interaction of wild-type LRRK2^{RCKW} with microtubules acts as a potent roadblock for the microtubule-based motors dynein and kinesin[39] suggests a mechanism for how increased *LRRK2* expression levels could be detrimental for membrane trafficking. All of the membrane cargos that LRRK2 has been implicated in trafficking—including lysosomes, endo-lysosomes, autophagosomes, and mitochondria[29]—are moved by dynein and kinesin[90–92]. Elevated LRRK2 kinase activity leading to the phosphorylation of Rab GTPases is also linked to changes in membrane trafficking and specifically in the recruitment of adaptor proteins that can bind dynein and kinesin motors[93,94]. Thus, examining the effects of increased *LRRK2* expression in combination with increased LRRK2 kinase activity may be relevant for understanding the molecular basis of Parkinson's Disease.

2.6 Methods

Cloning, plasmid construction, and mutagenesis

LRRK2^{RCKW} and Rab8a protein expression vectors were cloned as previously described[39]. The LRRK1 sequence was codon optimized for expression in *Spodoptera frugiperda* (Sf9) cells and synthesized by Epoch Life Science. The DNA coding for wild-type LRRK1 residues 631-2015 (LRRK1^{RCKW}) was cloned through Gibson assembly into the pKL baculoviral expression vector,

with an N-terminal His_6-Z-tag and TEV protease cleavage site. LRRK2 mutants were cloned using QuikChange site-directed mutagenesis (Agilent), or Q5 site-directed mutagenesis (New England Biolabs) following manufacturer's instructions. As previously described for $LRRK2^{RCKW}$[39], the $LRRK1^{RCKW}$ plasmid was used for the generation of recombinant baculoviruses according to bac-to-bac expression system protocols (Invitrogen).

For mammalian expression, GFP-LRRK2 was cloned into the pDEST53 vector (Addgene 25044) as previously described[39]. LRRK2 mutants were cloned using QuikChange site-directed mutagenesis (Agilent) using standard protocols, with the exception that liquid cultures of *E. coli* were grown at 30°C. EGFP-Rab10[95] was obtained from Addgene (#49472) and pET17b-Kif5b(1-560)-GFP-His[96] was obtained from Addgene (#15219).

$LRRK2^{RCKW}$ and $LRRK1^{RCKW}$ expression and purification

N-terminally His_6-Z-tagged $LRRK2^{RCKW}$ was expressed in Sf9 insect cells and purified as previously described[39]. Briefly, ~1L insect cells were infected with baculovirus and grown at 27°C for 3 days. Pelleted Sf9 cells were resuspended in lysis buffer (50 mM HEPES pH 7.4, 500 mM NaCl, 20 mM imidazole, 0.5 mM TCEP, 5% glycerol, 5 mM $MgCl_2$, 20 µM GDP, 0.5 mM Pefabloc, and protease inhibitor cocktail tablets) and lysed by Dounce homogenization. Clarified lysate was incubated with Ni-NTA agarose beads (Qiagen), extensively washed with lysis buffer, and eluted in buffer containing 300 mM imidazole. Protein eluate was diluted 2-fold in buffer containing no NaCl, loaded onto an SP Sepharose column, and eluted with a 250 mM to 2.5 M NaCl gradient. Protein was cleaved by TEV protease overnight. Cleaved protein was isolated by running over a second Ni-NTA column. Protein was concentrated and run on an S200 gel filtration column equilibrated in storage buffer (20 mM HEPES pH 7.4, 700 mM NaCl, 0.5 mM TCEP, 5% glycerol, 2.5 mM $MgCl_2$, 20 µM GDP). Final protein was concentrated to ~20-30 µM as estimated by absorbance at 280 nm using an extinction coefficient of 140150 $M^{-1}cm^{-1}$.

Purification of molecular motors

Human KIF5B$^{1-560}$(K560)-GFP was purified from *E. coli* using an adapted protocol previously described (Nicholas et al. 2014). All protein purification steps were performed at 4°C unless otherwise noted. pET17b-Kif5b(1-560)-GFP-His was transformed into BL-21[DE3]RIPL cells (New England Biolabs) until an optical density at 600 nm of 0.6-0.8 and expression was induced with 0.5 mM isopropyl-β-d-thiogalactoside (IPTG) for 16h at 18°C. Frozen pellets from 7.5 liters of culture were resuspended in 120 ml lysis buffer (50 mM Tris, 300 mM NaCl, 5 mM $MgCl_2$, 0.2 M sucrose, 1 mM dithiothreitol (DTT), 0.1 mM Mg-ATP, and 0.5 mM Pefabloc, pH 7.5) supplemented with one cOmplete EDTA-free protease inhibitor cocktail tablet (Roche) per 50 ml and 1 mg/ml lysozyme. The resuspension was incubated on ice for 30 min and lysed by sonication. Sonicate was supplied with 0.5 mM PMSF and clarified by centrifugation at 40,000 rcf for 60 min in a Type 70 Ti rotor (Beckman). The clarified supernatant was incubated with 15 ml Ni-NTA agarose (Qiagen) and rotated in a nutator for 1 h. The mixture was washed with 100 ml wash buffer (50 mM Tris, 300 mM NaCl, 5 mM $MgCl_2$, 0.2 M sucrose, 10 mM imidazole, 1 mM dithiothreitol (DTT), 0.1 mM Mg-ATP, and 0.5 mM Pefabloc, pH 7.5) by gravity flow. Beads were resuspended in elution buffer (50 mM Tris, 300 mM NaCl, 5 mM $MgCl_2$, 0.2 M sucrose, 250 mM imidazole, 0.1 mM Mg-ATP, and 5 mM βME, pH 8.0), incubated for 5 min, and eluted stepwise in 0.5 mL increments. Peak fractions were combined, and buffer exchanged on a PD-10 desalting column (GE Healthcare) equilibrated in storage buffer (80 mM PIPES, 2 mM $MgCl_2$, 1 mM EGTA, 0.2 M sucrose, 1 mM DTT, and 0.1 mM Mg-ATP, pH 7.0). Peak fractions of motor solution were either flash-frozen at -80°C until further use or immediately subjected to microtubule bind and release purification. A total of 1 ml motor solution was incubated with 1 mM AMP-PNP and 20 μM taxol on ice in the dark for 5 min and subsequently warmed to room temperature. For microtubule bind and release, polymerized bovine brain tubulin was centrifuged through a glycerol cushion (80 mM PIPES, 2 mM $MgCl_2$, 1 mM EGTA, and 60% glycerol (v/v) with 20 μM taxol and 1 mM DTT) and resuspended as previously described[97] incubated with the motor solution in the dark for

15 min at room temperature. The motor-microtubule mixture was laid on top of a glycerol cushion and centrifuged in a TLA120.2 rotor at 80,000 rpm (278088*g)* for 12 min at room temperature. Final pellet (kinesin-bound microtubules) was washed with BRB80 (80 mM PIPES, 2 mM $MgCl_2$, and 1 mM EGTA, pH 7.0) and incubated in 100 µl of release buffer (80 mM PIPES, 2 mM $MgCl_2$, 1 mM EGTA, and 300 mM KCl, pH 7 with 7.5 mM Mg-ATP) for 5 min at room temperature. The kinesin release solution was spun at 72,000 rpm (225252*g*) in TLA100 for 7 minutes at room temperature. The supernatant containing released kinesin was supplied with 660 mM sucrose and flash frozen. A typical kinesin prep in the lab yielded 0.5 to 1.5 µM K560-GFP dimer.

Rab8a expression and purification

Rab8a was expressed and purified as previously described[39]. Briefly, N-terminally His_6-ZZ tagged Rab8a was expressed in BL21(DE3) *E. coli* cells by addition of 0.5 mM IPTG for 18 hours at 18°C. Cells were pelleted, resuspended in lysis buffer (50 mM HEPES pH 7.4, 200 mM NaCl, 2 mM DTT, 10% glycerol, 5 mM $MgCl_2$, 0.5 mM Pefabloc, and protease inhibitor cocktail tablets), and lysed by sonication on ice. Clarified lysate was incubated with Ni-NTA agarose (Qiagen). Protein was washed with wash buffer (50 mM HEPES pH 7.4, 150 mM NaCl, 2 mM DTT, 10% glycerol, 5 mM $MgCl_2$) and eluted in buffer containing 300 mM imidazole. Eluate was incubated with IgG Sepharose 6 fast flow beads. Following further washing, Rab8a was cleaved off IgG Sepharose beads by incubation with TEV protease at 4°C overnight. Cleaved Rab8a was isolated by incubation with Ni-NTA agarose beads followed by washing with buffer containing 25 mM imidazole. Purified Rab8a was run on an S200 gel filtration column equilibrated in S200 buffer (50 mM HEPES pH 7.4, 200 mM NaCl, 2 mM DTT, 1% glycerol, 5 mM $MgCl_2$). Protein was then concentrated and exchanged into 10% glycerol for storage.

Cryo-electron microscopy: sample preparation and imaging of filaments

LRRK2^{RCKW} filaments were prepared as previously described[39] with the exception that 10% glycerol was used instead of 10% DMSO in all the samples save for the one that led to the initial data set ("19dec14f"), as glycerol promotes the formation of 11 and 12-protofilament microtubules. For "+MLi-2" samples, we added MLi-2 to LRRK2^{RCKW} to a final concentration of 5μM after incubating them with tubulin. The updated protocol is also available at protocols.io (http://dx.doi.org/10.17504/protocols.io.bpnrmmd6).

Cryo-EM data were collected on a Talos Arctica (FEI) operated at 200 kV, equipped with a K2 Summit direct electron detector (Gatan). Automated data collection was performed using Leginon[98] with a custom-made plug-in to automate the targeting to areas of the sample that contained LRRK2^{RCKW} filaments. The only exception was the first data set ("19dec14f"), which was collected using Leginon's regular raster target finder. The "19dec14f" dataset was subsequently used for training the machine learning component of the custom-made plug-in used for all other datasets. The code for the plug-in is available at (https://github.com/matyszm/filfinder).

The "Apo" reconstruction was obtained using two datasets: 836 micrographs from "19dec14f" and 1010 micrographs from "20aug12b". The "MLi-2" reconstruction was also obtained from two datasets: 926 micrographs from "20sep10b" and 1430 micrographs from "20sep30c". Final micrograph counts only include micrographs with at least one usable LRRK2^{RCKW} filament. The dose per dataset varied between 5 and 5.5 electrons Å−2 s−1. To accommodate for that range, we varied the exposure time between 10 and 11 seconds, with 200-ms frames, for a total number of frames between 50 and 55, and a total dose of 55 electrons Å−2. The images were collected at the nominal magnification of 36,000x, resulting in an object pixel size of 1.16 Å. The defocus was set to -1.5 μm, with a final range of defoci from -0.5 to -2.5 μm due to the nature of the lacey carbon grids and the collection strategy used. All datasets are available on EMPIAR (Table A.1).

Cryo-electron microscopy: reconstruction of LRRK2^{RCKW} bound to a microtubule

Movie frames were aligned using UCSF MotionCor2[99] with the dose-weighting option on. CTF estimation was done with CTFFIND4[100] using the non-dose-weighted aligned micrographs. All micrographs containing filaments were kept regardless of the CTF estimated resolution. Data processing up to the symmetry expansion step is detailed in the protocol available in protocols.io (http://dx.doi.org/10.17504/protocols.io.bwwnpfde). In brief, manual selected filaments from a subset of micrographs were 2D classified (Relion 3.1)[101], with the best classes then acting as a reference for automated filament picking (Relion 3.1). The separation distance of the particles was set to 30 Å, which ensures each particle contains one new LRRK2^{RCKW} dimer per strand. These particles were then filtered first by classifying based on whether a microtubule is present, then followed up by another 2D classification focusing on the presence of ordered LRRK2^{RCKW} filaments if MLi-2 was present, or a blurred, disordered layer if working with apo filaments. The selected particles were then 3D classified into 6 classes (Relion 3.1), each one corresponding to a specifically sized microtubule (from 11 to 16-protofilaments). This step is inspired by MiRP[102] and used their provided reference scaled to the appropriate pixel size. Filaments with MLi-2 present tend to favor 11-protofilament microtubules, while the apo filaments favored larger sizes. We kept all the 11-protofilament microtubules for the MLi-2 dataset and all the 12-protofilament microtubules for the apo dataset.

In order to more accurately reconstruct the LRRK2^{RCKW} filaments, the microtubule had to be digitally subtracted from the particles. To accomplish this, we refined the structure of the microtubule for each dataset (Relion 3.1) and subtracted it from the particles (Relion 3.1, using legacy subtraction mode). This allowed us to 2D classify (Relion 3.1) focusing on LRRK2^{RCKW} filaments. Particles falling into ordered 2D classes were further 3D classified (Relion 3.1). The initial reference for each subgroup (with or without MLi-2) was always a featureless cylinder and was initialized with the helical symmetry reported for microtubule-associated LRRK2 filaments in cells[30]. Subsequent rounds used the output as the reference and were allowed to refine the

symmetry, often showing multiple classes (Fig. A.1b and Table A.2). Once the symmetry was found, a local refinement was done with the original un-subtracted particles to give us a LRRK2^{RCKW} filament containing some of the original microtubule density. Since our LRRK2^{RCKW} filaments each have three strands, we used symmetry expansion to extract an individual dimer from each strand. We centered the new particles on the subtraction mask and decreased the box size to 300 pixels while keeping the Å/px scale the same. This step was performed with the new subtraction function in Relion 3.1. This resulted in 206,649 particles for the MLi-2 dataset and 49,629 particles for the apo dataset. See Figs. A.1b,c and A.2 for the data processing workflow. A more detailed protocol can be found in protocols.io (http://dx.doi.org/10.17504/protocols.io.bwwnpfde). After symmetry expansion, the newly generated particles were exclusively processed in CryoSPARC version 3.2.0. The first step was always to align the particles to the centered subtraction mask in order to align the particles to each other. For the particles coming from the MLi-2 dataset we were able to compare the Psi Euler angle to the original angle assigned during the microtubule only alignment. Since the particles were allowed to be flipped during the LRRK2^{RCKW} refinement, only particles showing 0+/-20 degrees and 180+/-20 degrees were kept. Particles with a ~180 flip were flipped back to align them to the microtubule. This left us with 133,246 particles for the MLi-2 dataset. This step was skipped for the apo particles due to the lower particle count.

The MLi-2 dataset was processed in two different ways, resulting in different levels of detail in either the kinase or ROC regions. The first processing strategy was designed to achieve a better kinase reconstruction. Here, we allowed the filtered particles to be freely aligned again, ignoring the microtubule orientation. This was followed by two local refinements: the first focused on a LRRK2^{RCKW} tetramer, and the second on a single LRRK2^{RCKW} monomer. The second strategy was designed to better resolve the contacts between the ROC domain and the microtubule. Here, we only performed local refinements on the particles with the fixed microtubule orientation. To make sure the microtubule was properly aligned, we performed a local refinement focusing only

on the microtubule, which resulted in a map with no ambiguity in the tubulin orientation. We then did a local refinement focused on a LRRK2^{RCKW} dimer, followed by a 3D Variability Analysis (3DVA, in cryoSPARC)[103] focused on a single LRRK2^{RCKW} monomer with the goal of being able to separate particles that have intact LRRK2^{RCKW} in them. We analyzed the components generated and determined that components 1 and 2 ranged from a well formed LRRK2^{RCKW} to having discontinuities or weak densities. We only kept particles with a negative value for at least one of the two components. Following that, we did another refinement for a LRRK2^{RCKW} dimer using the filtered particles, and then used a smaller mask to cover either the "+" or "-" LRRK2^{RCKW} (see Fig. A.1c) along with a small part of the microtubule. This resulted in maps showing the ROC domains interacting with the microtubule.

For the apo sample, only the freely aligned approach was used as the particle count and resolution was too low to filter the particles by microtubule orientation. After freely aligning the particles to the recentered subtraction mask, we performed a local refinement focused on the LRRK2^{RCKW} tetramer. To help the alignment, we used a 20 Å low-passed LRRK2^{RCKW} tetramer reference built by rigid body fitting 4 copies of LRRK2^{RCKW} into the early 9 Å reconstruction. This new reconstruction was still noisy, most likely due to multiple conformations being present. While Relion Class3D did not work on this dataset, we were able to use 3DVA again to help us find a component to separate apo LRRK2^{RCKW} into classes. Component 1 resulted in more a detailed reconstruction at both positive and negative ends of the spectra than the starting structure. We reconstructed both sets, and while both were able to reach ~7 Å resolution, the data with the positive component 1 resulted in a more continuous map and was chosen as the final map.

Model creation and refinement: LRRK2 ROC domain interacting with the microtubule

For modeling we used the maps where the refinement had been focused on the interactions of the ROC domain with the microtubule, facing either towards the plus or minus end of the microtubule. For the initial model, we used LRRK2's AlphaFold[77,78] model (Q5S007) as it

had the most complete loops available for the ROC domain (using residues 1332-1525). Since AlphaFold models lack ligands, we added GDP based on the placement in previous structures[39,60]. Because the ROC domain only occupies a small portion of the map and some microtubule density is present, we added tubulin dimers (PDB code: 1TUB) to provide a restraint during refinement. Initial refinement was done using Rosetta (ver 3.13) and Frank DiMaio's cryo-EM refinement scripts. 200 models were generated from each map. Tubulin dimers were removed from the model before further quantification. Models with the best energy score and fit to the density were manually inspected. Small modeling errors were corrected in Isolde by hand and refined one more time in Rosetta using Relax with the map density loaded in as a restraint. 5 models were selected for each map and converted to poly-alanine models except for residues of interest (K1358, K1359, R1384, K1385, R1501).

Cryo-electron microscopy: sample preparation and imaging of LRRK1^{RCKW}

The protocol for preparing LRRK1^{RCKW} grids is available at protocols.io (http://dx.doi.org/10.17504/protocols.io.b3rqqm5w). Briefly, the protein was spun down after thawing, and kept on ice until grid making. We used UltrAuFoil Holey Gold 1.2/1.3 300 mesh grids and plasma cleaned them in a Solarus II (Gatan) using the QuantiFoil Au preset. Immediately before freezing, LRRK1^{RCKW} was added to "LRRK2 buffer" (20 mM HEPES pH 7.4, 80 mM NaCl, 0.5 mM TCEP, 2.5 mM $MgCl_2$, 20 μM GDP) to the desired concentration (2-6 μM protein). We used a Vitrobot Mark IV (FEI) to freeze our samples.

Cryo-EM data were collected on a Talos Arctica (FEI) operated at 200 kV, equipped with a K2 Summit direct electron detector (Gatan). Automated data collection was performed using Leginon.[98] Reconstruction was done with 4 datasets ("19dec11a": 847 micrographs, "19dec21c":926 micrographs, "20sep11a": 904 micrographs, and "21jan18d": 952 micrographs). One of the datasets ("20sep11a") was collected at a 20° tilt. The exposure of the micrographs varied to achieve a total dose of 55 electrons Å−2. The images were collected at a nominal

magnification of 36,000x, resulting in an object pixel size of 1.16 Å. The defocus was set to -1.5 µm, which gave a range of defoci of -0.8 to -1.8 µm over all datasets. All datasets are available on EMPIAR (Table A.1).

Cryo-electron microscopy: reconstruction of LRRK1^{RCKW}

Movie frames were aligned in cryoSPARC using the "patch motion correction" program. CTF estimation was also done in cryoSPARC using the "patch CTF estimation" program. Images were manually screened for any obvious defects and removed from further processing if defects were found. Particle picking was done with a mixture of a crYOLO[104] set previously trained for LRRK2^{RCKW},[39] and simple blob picking followed by a round of 2D classification to remove obvious contaminants. Both methods gave similar results, and both were used depending on whether the picking was done on the fly (blob picker) or later (crYOLO). The final particle count was 645,743.

At this point, 2D classification was used on the combined particles. Only classes showing an intact RCKW-like shape were kept. Using ab-initio reconstruction gave us 2 classes, with 2/3 of the particles ending in the intact class. We recovered additional intact particles from the broken class after another round of 2D classification. Combining class 1 and the good 2D classes gave us 131,821 particles, from which we were able to obtain a 5.8 Å map with some stretched features, likely due to preferred orientation. To lower the impact of preferred orientation, we used "Rebalance 2D" with the rebalance factor set to 0.7, making sure the smallest supergroup is at least 70% of the size of the largest. While the resolution dropped to 6.5 Å, the severity of the stretching was reduced.

Despite this improvement, the map contained discontinuous density on the edges of the mask, suggesting problems with the automatically generated mask. We remade the mask by basing it on homology models of LRRK1^{RCKW} domains (ROC, COR, and Kinase; SWISS model[105],) and LRRK2's WD40 domain that we rigid body fitted into the current best LRRK1^{RCKW} density and used molmap in ChimeraX[106] to create a map to serve as the mask. This map was

low-passed to 15 Å, dilated by 8 px, and soft padded by another 8 px. This was then used to refine the structure one more time. This new map still contained artifacts in the ROC and COR-A region. We used 3DVA to analyze the structure and found a component showing slight movement of these domains. We selected to focus on particles in the more “closed” state. Refining these new particles gave us a better-defined map without artifacts at 5.8 Å resolution after using cryoSPARC’s Non-Uniform Refinement.

Single-molecule microscopy and motility assays

Single-molecule kinesin motility assays were performed as previously described[39]. Imaging was performed with an inverted microscope (Ti-E Eclipse; Nikon) equipped with a 100x 1.49 NA oil immersion objective (Plano Apo; Nikon). The microscope was equipped with a LU-NV laser launch (Nikon), with 405 nm, 488 nm, 532 nm, 561 nm, and 640 nm laser lines. The excitation and emission paths were filtered using appropriate single bandpass filter cubes (Chroma). The emitted signals were detected using an electron multiplying CCD camera (Andor Technology, iXon Ultra 888). The xy position of the stage was controlled by ProScan linear motor stage controller (Prior). Illumination and image acquisition were controlled by NIS Elements Advanced Research software (Nikon).

Single-molecule motility assays were performed in flow chambers assembled as previously described[107]. Biotin-PEG-functionalized coverslips (Microsurfaces) were adhered to glass slides using double-sided scotch tape. Each slide contained four flow-chambers. Taxol-stabilized microtubules (approximately 15 mg ml^{-1}) with 10% biotin-tubulin and 10% Alexa 405-tubulin were prepared as previously described[107]. For each motility experiment, 1 mg ml^{-1} streptavidin (in 30 mM HEPES, 2 mM magnesium acetate, 1 mM EGTA, 10% glycerol) was incubated in the flow chamber for 3 min. A 1:150 dilution of taxol-stabilized microtubules in motility assay buffer (30 mM HEPES, 50 mM potassium acetate, 2 mM magnesium acetate, 1 mM EGTA, 10% glycerol, 1 mM DTT and 20 μM Taxol, pH 7.4) was added to the flow chamber for 3 min to

adhere polymerized microtubules to the coverslip. Flow chambers containing adhered microtubules were washed twice with LRRK2 buffer (20 mM HEPES pH 7.4, 80 mM NaCl, 0.5 mM TCEP, 5% glycerol, 2.5 mM $MgCl_2$ and 20 μM GDP). Flow chambers were then incubated for 5 min with either LRRK2 buffer alone or LRRK2 buffer containing the indicated concentration of wildtype or mutant $LRRK2^{RCKW}$. Before the addition of kinesin motors, the flow chambers were washed three times with motility assay buffer containing 1 mg ml^{-1} casein. The final imaging buffer for motors contained motility assay buffer supplemented with 71.5 mM βME, 1 mM Mg-ATP, and an oxygen scavenger system, 0.4% glucose, 45 μg/ml glucose catalase (Sigma-Aldrich), and 1.15 mg/ml glucose oxidase (Sigma-Aldrich). The final concentration of kinesin in the motility chamber was 1 nM. K560–GFP was imaged every 500 ms for 2 min with 25% laser (488) power at 150 ms exposure time. Each sample was imaged no longer than 15 min. Each technical replicate consisted of movies from at least two fields of view containing between 5 and 10 microtubules each.

Single-molecule motility assay analysis

Kymographs were generated from motility movies using ImageJ macros as described previously[107]. Specifically, maximum-intensity projections were generated from time-lapse sequences to define the trajectory of particles on a single microtubule. The segmented line tool was used to trace the trajectories and map them onto the original video sequence, which was subsequently re-sliced to generate a kymograph. Brightness and contrast were adjusted in ImageJ for all videos and kymographs. Motile and immotile events (>1 s) were manually traced using ImageJ and quantified for run lengths and percent motility. Run-length measurements were calculated from motile events only. For percent motility per microtubule measurements, motile events (>1 s and >785 nm) were divided by total events per kymograph. Bright aggregates, which were less than 5% of the population, were excluded from the analysis. Data visualization and

statistical analyses were performed in GraphPad Prism (9.2; GraphPad Software) and ImageJ (2.0).

Microtubule sedimentation binding assay

Porcine brain tubulin was purchased from Cytoskeleton, Inc. Taxol-stabilized microtubules were polymerized at a final concentration of ~ 2.5 mg/mL, and free tubulin was removed by ultracentrifugation at 108628 x g for 15 min at 37°C through a 64% glycerol cushion. The resulting microtubule pellet was resuspended in LRRK2 binding buffer (20 mM HEPES pH 7.4, 110 mM NaCl, 0.5 mM TCEP, 5% glycerol, 2.5 mM $MgCl_2$, 20 μM GDP and 20 μM Taxol). Tubulin concentration was determined by comparison of the polymerized microtubule stock to actin standards on SDS-PAGE.

For a typical $LRRK^{RCKW}$ microtubule cosedimentation assay, 200 nM $LRRK^{RCKW}$ was incubated at room temperature for 10 minutes with varied concentrations of microtubules in buffer containing 20 mM Hepes pH 7.4, 110 mM NaCl, 0.5 mM $MgCl_2$, 0.5 mM TCEP, 5% glycerol, 20 μM GDP, 20 μM taxol. Microtubules were then pelleted by ultracentrifugation (15 minutes, 108628 g, 25 degrees). To quantify the depletion of $LRRK2^{RCKW}$, samples of the supernatant were taken and boiled for 10 min in SDS buffer. Samples were run on 4-12% polyacrylamide gels (NuPage, Invitrogen) and stained with SYPRO-Red Protein Gel Stain (ThermoFisher) for protein detection. Binding curves were fit in GraphPad Prism (9.2; GraphPad Software) with a nonlinear regression hyperbolic curve.

TMR labeling

BODIPY TMR-X NHS Ester (ThermoFisher) was used to fluorescently label $LRRK2^{RCKW}$ and $LRRK1^{RCKW}$. For a typical 40 uL labeling reaction, dye was added at a ratio of 1:1 to ~20 uM $LRRK2^{RCKW}$, followed by incubation at room temperature for 1 hour. Excess dye was removed by two consecutive buffer exchanges through Micro Bio-Spin P-6 desalting columns (Bio-Rad).

Protein concentration and labeling efficiency were estimated using a NanoDrop Microvolume Spectrophotometer.

Widefield fluorescence microtubule binding assay

Imaging was performed with an inverted microscope (Nikon, Ti-E Eclipse) equipped as described above (single-molecule microscopy and motility assays).

$LRRK2^{RCKW}$ microtubule-binding experiments were performed in flow chambers made as described above (single-molecule microscopy and motility assays). $LRRK^{RCKW}$ was labeled with TMR (TMR labeling, above); taxol-stabilized microtubules were polymerized from a mixture of unmodified, biotinylated, and Alexa-488 labeled bovine tubulin, as previously described (REF). To attach microtubules to the coverslip, flow chambers were incubated with 0.5 mg/mL streptavidin for 3 minutes, washed twice in buffer (30 mM Hepes pH7.4, 50 mM KOAc, 2 mM MgOAc, 1 mM EGTA, 10% glyercol, 1 mM DTT, and 0.2 mM taxol), and then incubated with microtubules for 3 minutes. Microtubules were washed twice in buffer (20 mM Hepes pH 7.4, 80 mM NaCl, 0.5 mM $MgCl_2$, 0.5 mM TCEP, 5% glycerol, 20 μM GDP), and then incubated with varied concentrations of $LRRK2^{RCKW}$ (6.25 nM – 50 nM) for 5 minutes. Multiple fields of view were imaged along the flow chamber with the objective in widefield illumination, with successive excitation at 488 nm (15% laser power, 100 ms exposure) and 561 nm (25% laser power, 100 ms exposure).

Image analysis was performed with ImageJ. Average TMR-$LRRK2^{RCKW}$ fluorescence intensity per microtubule was calculated from a 1 pixel-wide line drawn along the long axis of the microtubule; overall average background fluorescence intensity was subtracted. These background-subtracted intensities were averaged over all microtubules per field of view, normalized by microtubule length, to yield a single data point. Eight fields of view at each concentration of $LRRK2^{RKCW}$ were then averaged.

In vitro Rab8a phosphorylation

LRRK kinase assays were performed as previously described[39] with $LRRK^{RCKW}$ and Rab8a purified as described above. For a typical kinase reaction, 38 nM $LRRK^{RCKW}$ was incubated with 3.8 μM Rab8a for 30 minutes at 30 degrees in buffer containing 50 mM Hepes pH 7.4, 80 mM NaCl, 10 mM MgCl2, 1 mM ATP, 200 uM GDP, 0.5 mM TCEP. Phosphorylation of Rab8a at residue T72 by $LRRK^{RCKW}$ was monitored by western blot using a commercially available antibody (Abcam antibody MJF-R20) as previously described[39,108].

Immunofluorescence, confocal microscopy, and image analysis

LRRK2 filament assays were performed as previously described[39]. Briefly, cells were plated on fibronectin-coated glass coverslips and grown for 24 h before transfection with PEI. Cells were transfected with 500 ng of indicated GFP-LRRK2 plasmids. After 24-48 h, cells were incubated at 37°C with DMSO or MLi-2 (500 nM) for 2 h. Stocks of the kinase inhibitor MLi-2 (10 mM; Tocris) were stored in DMSO at -20°C.

Cells were rinsed briefly with ice-cold 1x PBS on ice, the fixed with ice-cold 4% PFA, 90% methanol, 5 MM sodium bicarbonate for 10 min at -20°C. Coverslips were subsequently washed three times with ice-cold PBS and then incubated with blocking buffer (1% BSA, 5% normal goat serum, 0.3% Triton X-100 in 1x PBS) for 1 h at room temperature. Primary antibodies were diluted in antibody dilution buffer (1% BSA, 0.1% Triton X-100 in 1x PBS) and incubated at 4°C overnight. The following day, coverslips were washed three times with 1x PBS and incubated with secondary antibodies diluted in antibody dilution buffer for 1 h at room temperature. After secondary incubation, coverslips were washed three times with 1x PBS. Cells were briefly rinsed in ddH_2O and mounted on glass slides using CitiFluor AF-1 mounting media (TedPella). Coverslips were sealed with nail polish and stored at 4°C. Antibodies used for immunofluorescence were used at a 1:500 dilution and included: chicken anti-GFP (Aves Labs) and goat anti-chicken-Alexa 488

(ThermoFisher). DAPI was used at 1:5000 according to the manufacturer's recommendation (ThermoFisher).

For the LRRK2 filament analysis, experimenters were blinded to conditions for both the imaging acquisition and analysis. Cells were imaged using a Yokogawa W1 confocal scanhead mounted to a Nikon Ti2 microscope with an Apo 60x 1.49 NA objective. The microscope was run with NIS Elements using the 488nm and 405nm lines of a six-line (405nm, 445nm, 488nm, 515nm, 561nm, and 640nm) LUN-F-XL laser engine and a Prime95B camera (Photometrics).

ImageJ was used to quantify the percentage of cells with LRRK2 filaments as previously described . Maximum-intensity projections were generated from *z*-stack confocal images. Using the GFP immunofluorescence signal, transfected cells were identified. Cells were scored for the presence or absence of filaments using both the *z*-projection and *z*-stack micrographs as a guide. To calculate the percentage cells with filaments, the number of cells with filaments was divided by the total number of transfected cells per technical replicate (defined as one 24-well coverslip). Per coverslip, eight fields of view were imaged containing a total of 50 and 150 cells per replicate. The quantification of all cellular experiments come from compiled data collected on at least three separate days. All statistical analyses were performed in GraphPad Prism (9.2; GraphPad Software).

Western blot analysis and antibodies

For western blot quantification of LRRK2 protein expression and Rab10 phosphorylation, cells were plated on 6-well dishes (200,000 cells per well) 24 h before transfection. Cells were transfected with 500 ng of GFP-LRRK2 construct and 500 ng of GFP-Rab10 using polyethylenimine (PEI, Polysciences). After 36 h, cells were rinsed with ice-cold 1x PBS, pH 7.4 and lysed on ice in RIPA buffer (50 nM Tris pH7.5, 150 mM NaCl, 0.2% Triton X-100, 0.1% SDS, with cOmplete protease inhibitor cocktail and PhoStop phosphatase inhibitor). Lysates were rotated for 15 min at 4°C and clarified by centrifugation at maximum speed in a 4°C

microcentrifuge for 15 min. Supernatants were then boiled for 10 minutes in SDS buffer. Experiments were performed in duplicate or triplicate and repeated on at least 3 separate days. Lysates were run on 4-12% polyacrylamide gels (NuPage, Invitrogen) for 50 minutes at 180V and transferred to polyvinylidene difluoride (Immobilon-FL, EMD Millipore) for 4 h at 200 mA constant current. Blots were rinsed briefly in MilliQ water and dried at room temperature for at least 30 min. Membranes were briefly reactivated with methanol and blocked for 1 h at room temperature in 5% milk (w/v) in TBS. Antibodies were diluted in 1% milk in TBS with 0.1% Tween-20 (TBST). Primary antibodies used for immunoblots were as follows: mouse anti-GFP (Santa Cruz, 1:2500 dilution), rabbit anti-LRRK2 (Abcam, 1:5000 dilution), rabbit anti-GAPDH (Cell Signaling Technology, 1:3000 dilution), and rabbit anti-phospho-T73-RAB10 (Abcam, 1:2500 dilution). Secondary antibodies (1:15000) used for western blots were IRDye goat anti-mouse 680RD and IRDye goat anti-rabbit 780RD (Li-COR). Primary antibodies were incubated overnight at 4°C, and secondary antibodies were incubated at room temperature for 1 h. For quantification, blots were imaged on an Odyssey CLx controlled by Imaging Studio software (v.5.2), and intensity of bands quantified using Image Studio Lite software (v.5.2).

Cell line

Human 293T cells were obtained from ATCC (CRL-3216) and maintained at 37°C with 5% CO_2 in Dulbecco's Modified Eagle Medium (DMEM, Corning) supplemented with 10% fetal bovine serum (FBS, Gibco) and 1% penicillin/streptomycin (PenStrep; Corning). Cells were routinely tested for mycoplasma contamination and were not authenticated after purchase.

Sequence alignment

Protein sequences of LRRK2 and LRRK1 were obtained from UniProt. Sequence alignments were performed with Clustal Omega web services and annotated using Jalview[109].

Data availability Statement

Data that support this study can be found in Table A.1, which lists EMD and EMPIAR codes for the structural biology data.

2.7 Acknowledgements

We thank our funders: the Howard Hughes Medical Institute (where Samara L.Reck-Peterson is an Investigator); Aligning Science Across Parkinson's (Samara L. Reck-Peterson and Andres E. Leschziner) the Michael J. Fox Foundation (grant number 18321 to Samara L. Reck-Peterson and Andres E. Leschziner); the A.P. Giannini Foundation (postdoctoral fellowship to David M. Snead); the Molecular Biophysics Training Grant at UC San Diego (NIH Grant T32 GM008326 supported Andrea M. Dickey); the National Institutes of Health (R01GM121772 to Samara L. Reck-Peterson and R01GM107214 to Andres E. Leschziner). We also thank the UC San Diego Cryo-EM Facility, the Nikon Imaging Center at UC San Diego and Eric Griffis, and the UC San Diego Physics Computing Facility for IT support.

Chapter 2, in full, is a reprint of the material as it appears in Structural basis for Parkinson's Disease-linked LRRK2's binding to microtubules. David M. Snead*, Mariusz Matyszewski*, Andrea M. Dickey*, Yu Xuan Lin, Andres E. Leschziner, Samara L. Reck-Peterson, bioRxiv, 2022. The dissertation author was a co-author of this paper. * denotes equal contributions.

CHAPTER 3: CONCLUSIONS AND FUTURE DIRECTIONS

In this chapter, I will summarize our findings on how LRRK2 binds to microtubules and discuss future directions our insights have led to. Although recent breakthroughs have been made in our understanding of LRRK2 function, there is still much that is unknown about LRRK2's molecular and cellular roles, including open questions relating to how the varied cellular localization of LRRK2 – cytosolic, membrane-associated, and microtubule-associated – contributes to its function and PD pathology.

3.1 Factors determining LRRK2's interaction with microtubules

Previous data suggested the closed conformation LRRK2's kinase favors filament formation and binding to microtubules is mediated by the ROC domain. In chapter 2, we reported on a higher resolution structure of LRRK2 filaments that confirms this conformation of the kinase, binding via the ROC domain, and provides for higher precision mapping of the LRRK2-LRRK2 domain interactions in these filaments. We also report a structure of the catalytic half of LRRK1. Guided by these structures, we identify residues in the ROC domain that mediate LRRK2 binding. We also show that the charged, unstructured carboxy-terminal tails of tubulin are important for microtubule binding.

Using mutagenesis, we disrupted both the WD40/WD40 and COR/COR dimer interfaces and showed that breaking these interfaces abolished LRRK2 filament formation in cells. In vitro, we measured microtubule binding and inhibition of kinesin motor motility, the effects of these dimer interface mutations were less extreme, with our COR/COR mutants decreasing microtubule binding by ~50% and our WD40/WD40 mutants have no effect. Taken together, our data suggests that small LRRK2 oligomers, as small as a dimer, could act as a roadblock and disrupt microtubule motor motility.

It remains unclear what the physiological role of this interaction may be and how it contributes to LRRK2 function and dysfunction in human disease. However, we now have better

tools to parse the role of microtubule-associated LRRK2. A key question to answer next is how LRRK2's function is impacted when it is no longer capable of interacting with the microtubule cytoskeleton.

3.2 Future directions and speculation

We have now identified multiple residues within the ROC domain of LRRK2 that mediate interaction with MTs and resist filament formation even in the presence of kinase inhibitors that drive wild type protein to MTs. However, a current limitation to our studies with these novel structure-based mutants is the reliance on transient overexpression systems in mammalian cells. As such, our future plans include the generation of cell lines with endogenous levels of LRRK2 ROC domain basic patch mutants. Given the high expression and identified LRRK2 roles in cells of the nervous and immune systems, we plan to generate these mutant lines in human iPSCs, which we will be able to differentiate into neuron and macrophage cells. We have obtained LRRK2 KO iPSC lines, as well as isogenic iPSCs that contain all the major PD mutations[110]. Using CRISPR or other stable expression integration systems, we will introduce our mutants into these cells. These cell lines will be used to answer important questions about how the cellular localization of LRRK2 relates to its function as these cells will be deficient in LRRK2-microtubule binding. As mentioned above, LRRK2 exists in the cell in three pools – cytosolic, membrane-bound, and MT-bound. Using phosphospecific antibodies, we will be also be able to monitor phosphorylation of LRRK2 itself and its substrates (Rabs 3, 8, and 10) phosphorylation and cilia formation (a process that has been linked to LRRK2 function[41,42]) in these cell lines. We may also monitor for defects in Rab-trafficking in these cells. Microtubule-associated LRRK2 can act as a roadblock for molecular motors in vitro[39] and motors are responsible for the long-distance transport of Rab-marked vesicles throughout the cells. These molecular motors can also bind directly or indirectly to some Rabs[55], using in vitro reconstitution systems (such as those described in Appendix B), we can explore the transport of these cargoes by motors and how microtubule-

bound LRRK2 acts as a roadblock. These and many more experiments will allow us to address how microtubule-bound LRRK2 may be contributing to disease pathogenesis.

Furthermore, with these ROC basic patch mutants, we aim to remove LRRK2 from the microtubule and assess how shifting LRRK2 cellular localization alters its protein interactome and phosphoproteome. We will use proximity-dependent biotinlyation (BioID), as previously described[97,111,112], to identify LRRK2's cellular partners. Briefly, we will fuse a promiscuous biotin ligase to wild-type and mutant LRRK2. Proteins within a radius of labeling of approximately 10 nm of the tagged subunits are biotinylated on primary amines and the identity of these marked proteins determined with mass spectrometry (Fig 3.1). By characterizing the interactomes of the various cellular pools of LRRK2 we aim to answer the question of whether these pools have

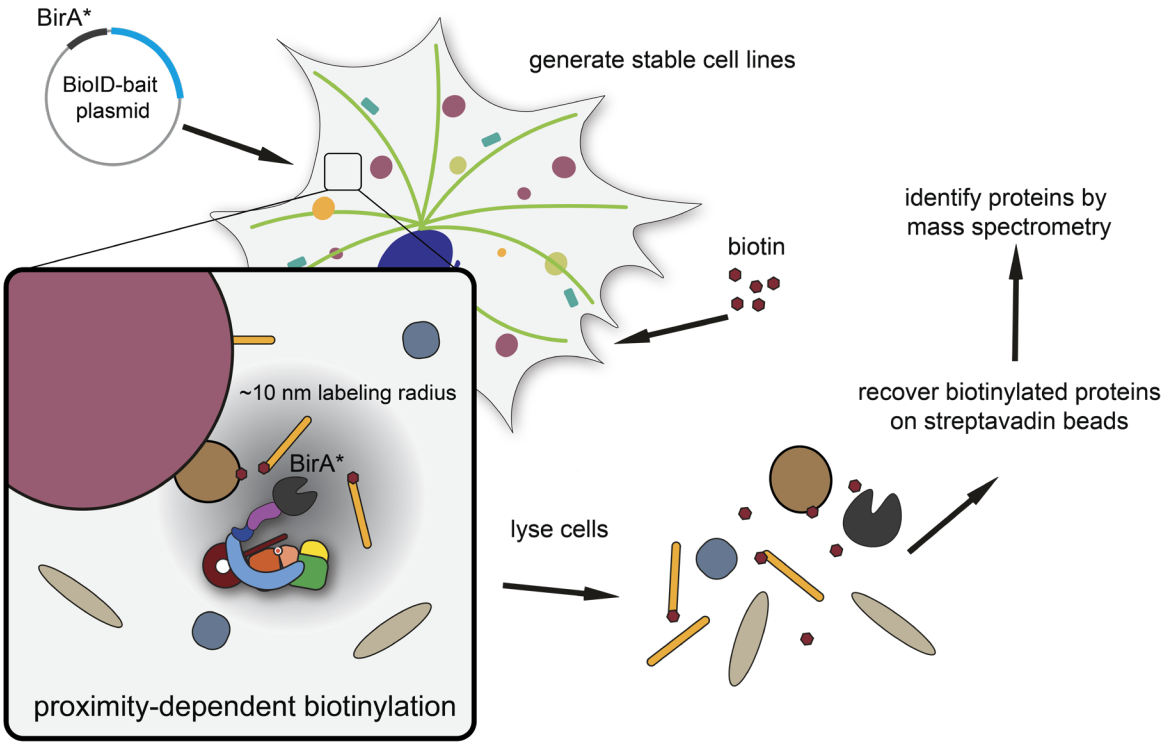

Figure 3.1: Schematic for proximity-dependent biotinylation workflow.
A promiscuous biotin ligase (BioID) is fused to a protein of interest and expressed in 293T cells. The promiscuous biotin ligase covalently modifies the primary amines of proximal proteins within ~10 nm labeling radius (Kim et al. 2014). The cells are lysed, biotinylated proximal proteins are isolated using streptavidin beads and identified by tandem mass spectrometry. BioID technique can report on transient interactions as well as spatial information of the interactors (Roux et al. 2012).

different functions. Furthermore, preliminary data using conditionally-immortalized murine macrophages[113] (Figure 3.2), demonstrate the high endogenous expression of LRRK2 in immune cells and the increased expression upon stimulation of an immune response by treatment with lipopolysaccharides (LPS). It has also previously been shown that LRRK2 can be recruited to membranes in macrophages and microglia cells that are stimulated with LPS[51]. It will be interesting to observe if the basic patch LRRK2 mutants will still be recruited to membranes upon stimulation and if microtubule-association plays a role in these immune pathways.

In addition to follow-up work with our basic patch mutants in iPS cells at endogenous levels, there is also further work that may be done in our current overexpression systems. Interestingly, it appears that mutation of the RoC domain basic patches in the background of the PD mutation (I2020T) may reduce the phosphorylation of Rab10 in cells compared to the I2020T mutation alone. This is intriguing because I2020T is one of the major PD mutations that has been shown to have increased association with microtubule when overexpressed in cells[37]. This brings up the possibility that microtubule association, though not fully accounting for, may partially account for the increased kinase activity seen in the I2020T mutation. We will also want to test the kinase activity of the basic patch mutants in the background of the other PD-linked hyperactive mutants (R1441C and Y1699C), and as an important comparison, in the background of the PD-linked G2019S mutation. The G2019S mutation displays increased kinase activity in cells, but does not have increased microtubule-associated LRRK2 filament formation[37].

In addition to alterations in inhibitor-induced LRRK2 filament formation by the various mutations detailed in chapter 2 of this dissertation, it will be important in the future to assess the possible localization defects of these LRRK2 mutants. It has previously been shown that Rab29, another LRRK2 substrate, recruits LRRK2 to the trans-Golgi network and stimulates kinase activity and that pathogenic LRRK2 is recruited more efficiently[35,114,115]. Intriguingly, the pathogenic LRRK2 mutants used in these studies were the same mutants that enhance LRRK2 microtubule association. We wonder if removing LRRK2's interactions with microtubules will alter

this phenotype. To assess this, a future experiment will be to co-express the ROC domain of LRRK2 mutants with Rab29 and determine if these mutants colocalize with Rab29 and disperse Golgi membranes using an established immunofluorescence assay[35]. We may also further

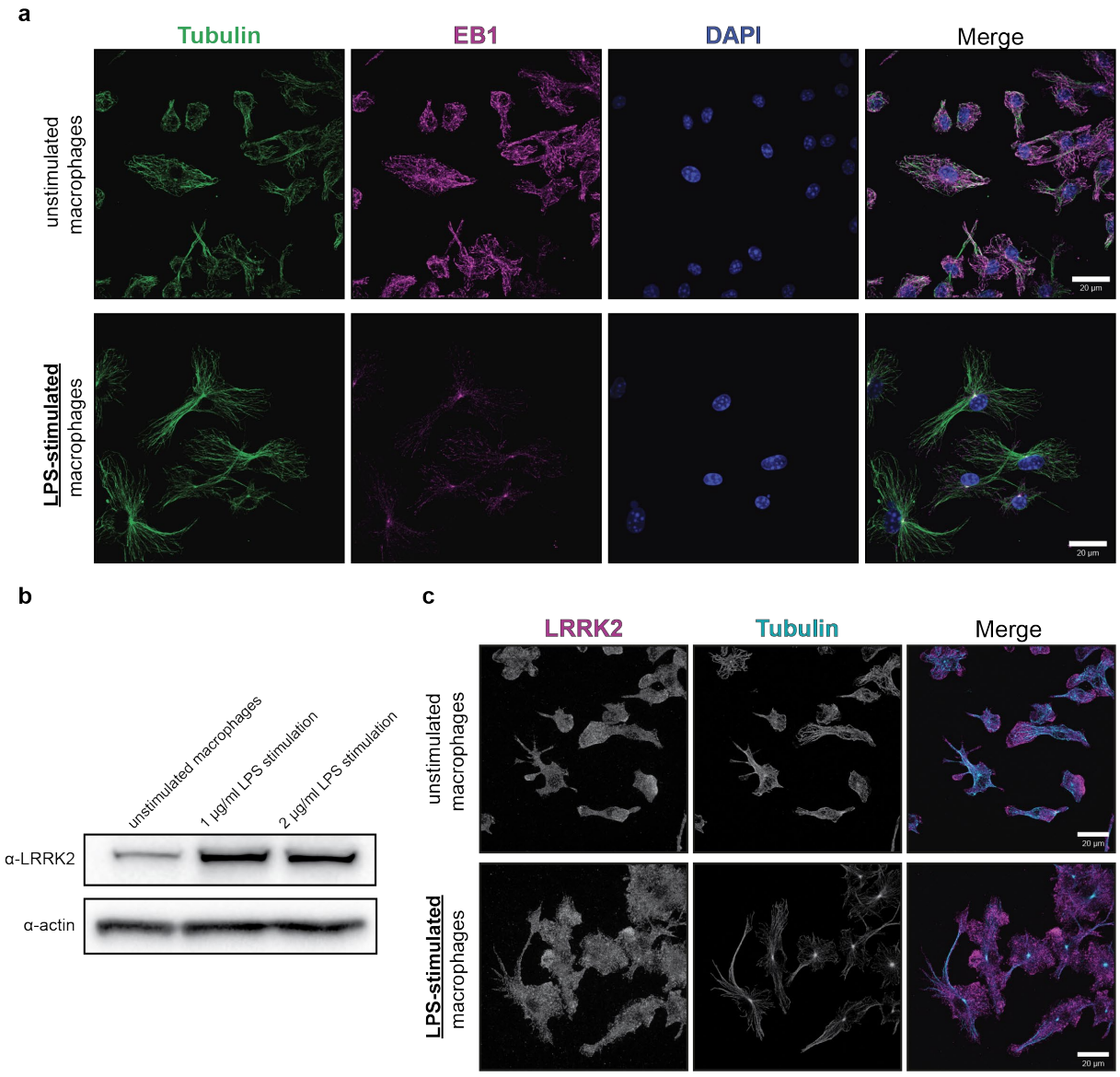

Figure 3.2: LRRK2 in stimulated and unstimulated macrophages.
a, Conditionally-immortalized murine macrophages (CIMs) were grown on fibronectin coated coverslips and stimulated with lipopolysaccharide (LPS) for 16 hours. The cells were fixed with a 3.7% paraformaldehyde/90% methanol/5mM sodium bicarbonate solution for 10 minutes at -20°C, permeabilized with 0.1% Triton X-100, and blocked with 1% BSA for 1 hour. Cells were labeled with antibodies against alpha-tubulin and EB1. Nuclear counterstain is DAPI. **b,** CIMs were treated with indicated concentrations of LPS, after 16 hours stimulated and unstimulated cells were lysed and immunoblotted for LRRK2 and actin. **c,** CIMs were plated, treated, and fixed as in (a). Cells were labeled with antibodies again alpha-tubulin and LRRK2. The images in (a) and (c) were captured at 100X magnification.

investigate the impact these basic patch mutations have on LRRK2 autophosphorylation or phosphorylation of other physiological substrates. In the studies presented here, we measured kinase activity by monitoring Rab10 phosphorylation, but it will be interesting to see if other LRRK2 substrates are phosphorylated to similar levels. We may also want to investigate if these mutations to the ROC domain impact 14-3-3 binding, as 14-3-3 proteins are highly expressed in the brain and known to bind to LRRK2.

Finally, though we have uncovered properties of LRRK2 that are important for microtubule binding and have shown that the carboxy-terminal tails of tubulin are important for LRRK2/microtubule interaction, there is still much to explore in what properties of the microtubules themselves may impact LRRK2 association. For example, it remains unclear if LRRK2 associates with stable or dynamic microtubules and if post-translational modifications (PTMs) on tubulin play a role in LRRK2 microtubule binding in cells[18,68]. Using microtubule binding assays, we can begin to determine if specific post-translational modifications are important for LRRK2 binding. Using enzymes that add or remove PTMs, such as deacetylases, tubulin-tyrosine ligases, and tubulin acetylases, to generate populations of microtubules enriched for individual PTMs and measure LRRK2 binding. We may also generate single PTM microtubules by purifying recombinant tubulin[116]. We can then compare the function of the wild-type LRRK2 to LRRK2 carrying PD-linked mutations to determine if these properties of LRRK2 change in disease.

3.3 LRRK1: Comparing LRRK2's closest homolog

In addition to LRRK2, mammals possess a second homolog of the leucine-rich repeat kinase called LRRK1[117]. LRRK2 has been clearly linked to both familial and sporadic Parkinson's disease[6,118–120]. Interestingly, LRRK1 does not seem clinically associated with PD, instead appearing to have roles in regulating bone biology, and is implicated in metabolic bone disorders

Figure 3.3: LRRK1 structure-guided mutagenesis.
a, Schematic of LRRK1 domain organization. **b, c,** Cryo-EM maps of monomeric and dimeric LRRK1, respectively, with cartoon depictions. **d,** Schematic of possible activation of LRRK1 suggested by structural studies. **e,f,** Rab7 phosphorylation in 293T cells overexpressing WT LRRK1 or LRRK1 carrying indicated mutations. LRRK1(K746G), which is known to increase Rab7 phosphorylation in cells, and LRRK1(D1409A), which is known to be kinase inactive, were tested as well. 293T cells were transiently transfected with the indicated plasmids encoding for FLAG-LRRK1 (wild type or mutant) and GFP-Rab7. Thirty-six hours post-transfection the cells were lysed, immunoblotted for phosphor-Rab7 (pS72), total GFP-Rab7, and total LRRK1, and developed with LI-COR Odyssey CLx imaging system, Quantification of data in (e) is shown in (f), normalized to wild-type, as mean ± s.e.m. Individual data points represent separate populations of cells obtained across three independent experiments. **g,h,** Rab7 phosphorylation in 293T cells overexpressing WT LRRK1 or LRRK1 carrying indicated mutations. 293T cells were transiently transfected with the indicated plasmids encoding for GFP-LRRK1 (wild type or mutant) and GFP-Rab7. 293T cells were treated as in (e). Quantification of data in (g) is shown in (h), normalized to wild-type, as mean ± s.e.m. Preliminary data taken from a single population of cells.

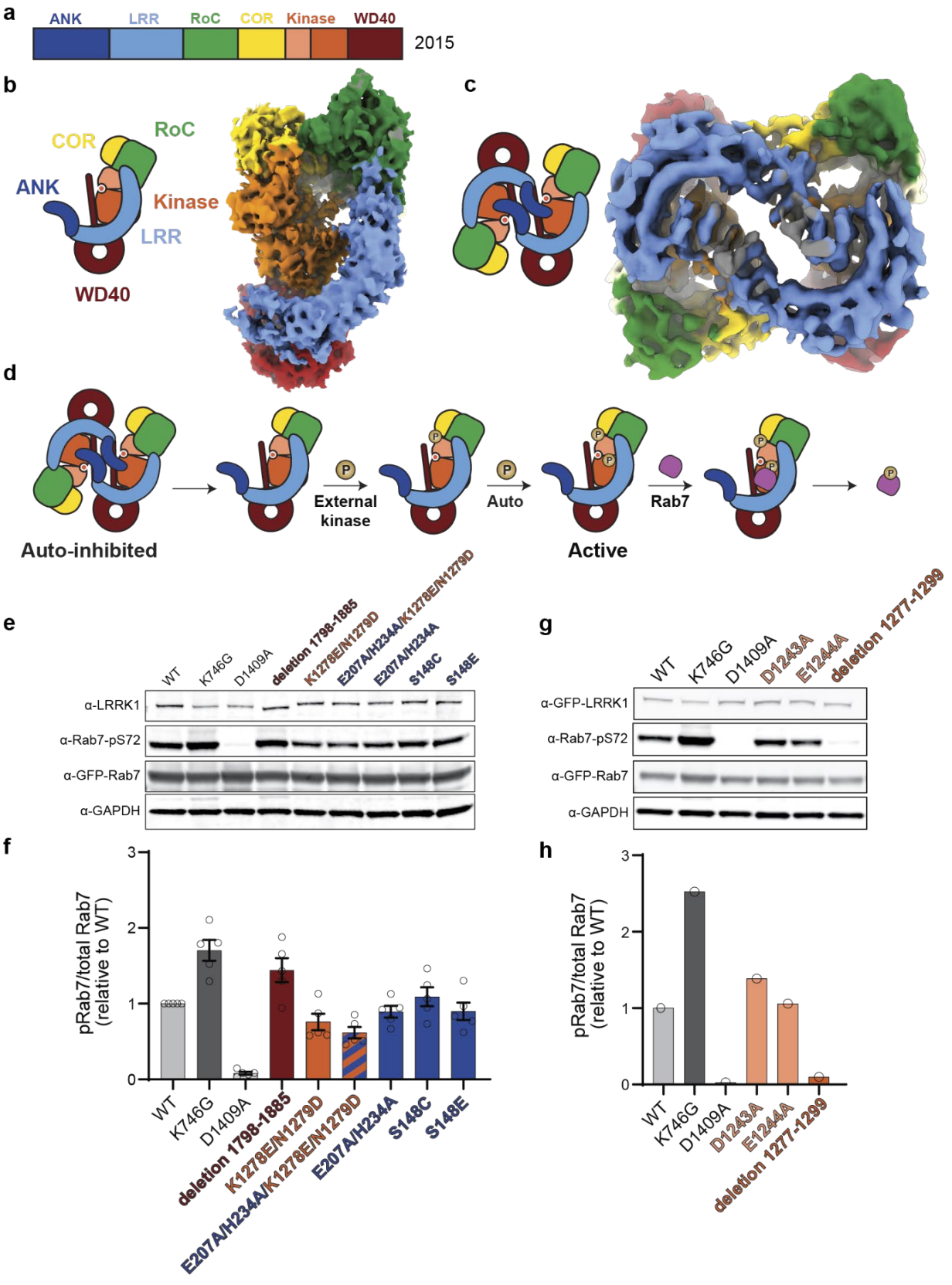
a
ANK
LRR
RoC
COR
Kinase
WD40
2015
b
COR
RoC
ANK
Kinase
LRR
WD40
c
d
Auto-inhibited
External kinase
Auto
Active
Rab7
e
WT
K746G
D1409A
deletion 1798-1885
K1278E/N1279D
E207A/H234A/K1278E/N1279D
E207A/H234A
S148C
S148E
α-LRRK1
α-Rab7-pS72
α-GFP-Rab7
α-GAPDH
g
WT
K746G
D1409A
D1243A
E1244A
deletion 1277-1299
α-GFP-LRRK1
α-Rab7-pS72
α-GFP-Rab7
α-GAPDH
f
pRab7/total Rab7 (relative to WT)
0
1
2
3
WT
K746G
D1409A
deletion 1798-1885
K1278E/N1279D
E207A/H234A/K1278E/N1279D
E207A/H234A
S148C
S148E
h
pRab7/total Rab7 (relative to WT)
0
1
2
3
WT
K746G
D1409A
D1243A
E1244A
deletion 1277-1299

and osteopetrosis[83,84,121,122]. The central domains of LRRK1 are somewhat well conserved with LRRK2, with 41%, 48%, 46%, and 50% similarity between the LRR domains, RoC, COR, and kinase domains, respectively[59]. The amino- and carboxy-termini of LRRK1 and LRRK2 are more divergent, with LRRK1 lacking amino-terminal armadillo repeats and only 27% sequence similarity in the region corresponding to LRRK2's WD40 domain (Fig. 3.3a). Structural information for LRRK1 has been more limited than LRRK2, with only a single published low-resolution cryo-EM

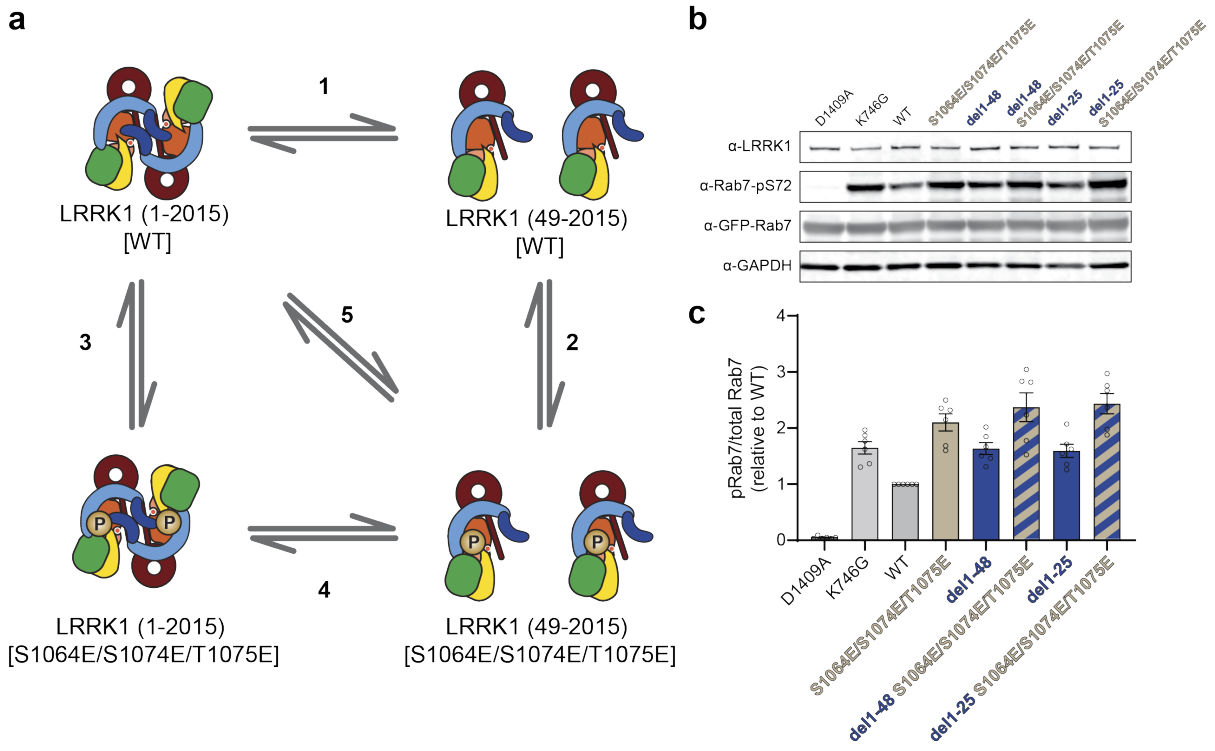

Figure 3.4: Working model of LRRK1 autoinhibition.
a, Schematic of possible mechanisms of LRRK1 autoinhibition. A loop in the COR-B domain contains multiple phosphorylation sites which may be connected to the monomer/dimer state. Proposed phosphomimetic mutations and truncation mutations designed to tease apart the factors responsible for LRRK1 autoinhibition. **b,c,** Rab7 phosphorylation in 293T cells overexpressing WT LRRK1 or LRRK1 carrying indicated mutations. LRRK1(K746G), which is known to increase Rab7 phosphorylation in cells, and LRRK1(D1409A), which is known to be kinase inactive, were tested as well. 293T cells were transiently transfected with the indicated plasmids encoding for LRRK1 (wild type or mutant) and GFP-Rab7. Thirty-six hours post-transfection the cells were lysed, immunoblotted for phosphor-Rab7 (pS72), total GFP-Rab7, and total LRRK1, and developed with LI-COR Odyssey CLx imaging system, Quantification of data in (b) is shown in (c), normalized to wild-type, as mean ± s.e.m. Individual data points represent separate populations of cells obtained across three independent experiments.

map of the full-length protein[59]. Prior to the work presented in chapter 2, where we report a cryo-EM structure of the carboxy-terminal half of LRRK1 (residues 631 to 2015), it was unclear whether LRRK1 contains a WD40 domain. Our cryo-EM structure unambiguously shows LRRK1 does indeed have a WD40 domain despite sequence divergence with LRRK2. We have now turned our focus to solving the structure of full-length LRRK1. We have solved initial structures of LRRK1 in both monomeric and dimeric states (Fig. 3.3b,c). Similar to LRRK2, we observe that the catalytic half of LRRK1 forms a J shape with the kinase domain C-lobe connecting to the ROC-COR domains. While LRRK1 is known to dimerize in solution, it is unknown how this dimerization affects kinase activity. Based on our structures, it seems likely that the dimer represents an autoinhibited state as the ankyrin domain of one LRRK1 monomer blocks access to the kinase active site of the other LRRK1 (Fig 3.3d). Guided by these structures, we have begun to make mutations in LRRK1 that we believe will break the dimer interfaces and will monitor phosphorylation of Rab7, a LRRK1 substrate (Fig 3.3e-h).

Furthermore, LRRK1, like LRRK2, has multiple serine and threonine residues that may be phosphorylated and may be involved in regulation of LRRK1's activity. In particular, there are three phosphorylatable residues in the COR-B domain of LRRK1 that, using mutagenesis, we have begun to explore as possibly being important for LRRK1 autoinhibition. We have monitored the phosphorylation of LRRK1's substrate, Rab7, (Fig. 3.4) and using a newly available phosphospecific antibody for phosphoS72 Rab7, we will also be able to monitor how phosphorylation by our LRRK1 mutants may impact Rab7 localization in cells (Fig 3.5). Overall, by comparing LRRK1 and LRRK2 structure and function, we aim to gain a better understanding of each protein and answer the outstanding questions: Why is LRRK1 not linked to PD pathogenesis? What features of LRRK2 underlie its pathogenic role?

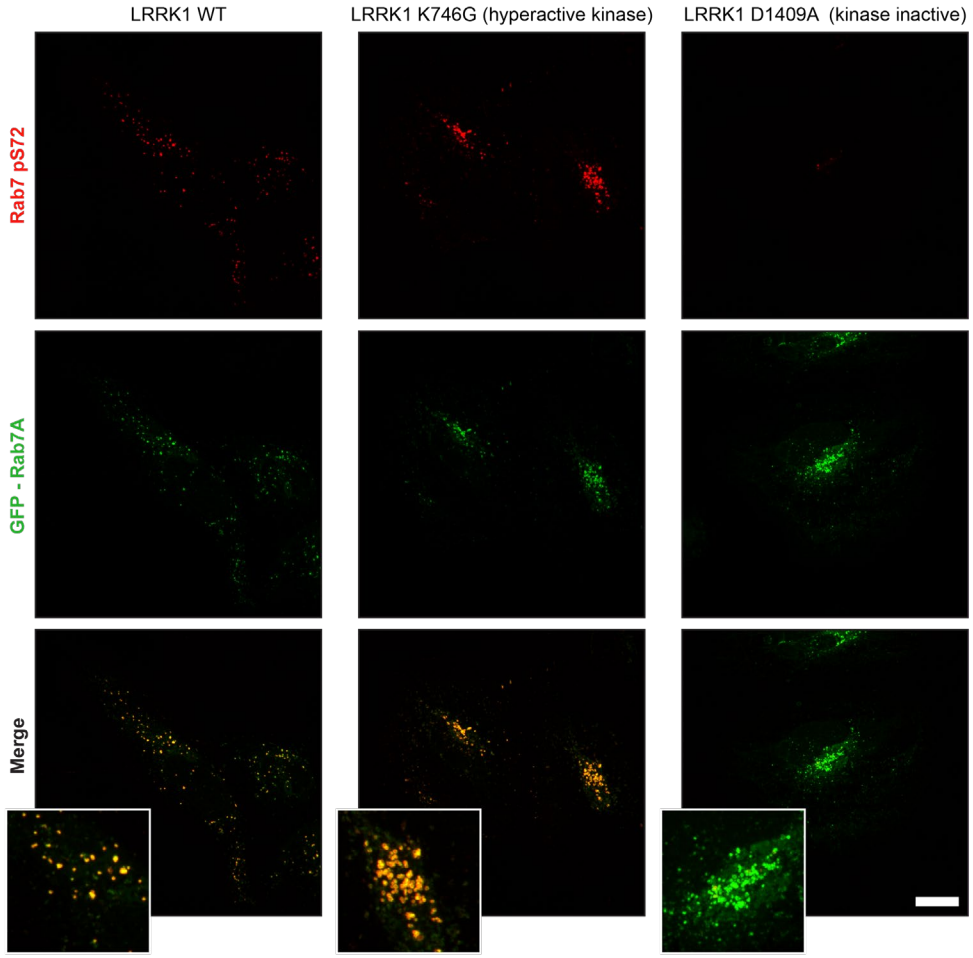

Figure 3.5: Immunofluorescent analysis of phospho S72 Rab7A in HeLa cells.
Hela cells transiently overexpressing GFP-Rab7A and indicated FLAG-LRRK1 constructs and labeled with anti-Rab7A (phospho S72) antibody (red). The cells were fixed with 4% paraformaldehyde for 20 minutes, permeabilized with 0.1% Triton X-100, and blocked with 1% BSA for 1 hour. Cells were labeled with 5 µg/mL of anti-Rab7A (phsopho S72) antibody overnight at 4°C, followed by goat anti-rabbit IgG (H&L, Alexa Fluor 647) secondary antibody at 1/500 dilution. GFP-Rab7A signal is shown in green. The images were captured at 100X magnification. Scale bar is 20 µm.

3.4 Concluding remarks

In summary, the results I presented in this dissertation highlight that LRRK2's interaction with microtubules is encoded in its dimer interfaces and basic residues of the ROC domain. Our identification of point mutations that can break these various interfaces and disrupt microtubule binding provide an invaluable tool moving forward to study the role of this microtubule-associated LRRK2 in cells. The ability to selectively perturb the microtuble-LRRK2 interaction while retaining

kinase function, will help to parse out the importance of cytoskeleton localization and its contribution to LRRK2's function and dysfunction in human health.

Chapter 3 contains unpublished material that may later be prepared for submission for publication co-authored with Janice Reimer, Yu Xuan Lin, Sebastian Mathea, Dario Alessi, Andres E. Leschziner, and Samara L. Reck-Peterson. The dissertation author was the primary author of this chapter.

APPENDIX A: SUPPLEMENTARY INFORMATION FOR CHAPTER 2

A.1 Supplementary figures for Chapter 2

Figure A.1: Cryo-EM structure determination of microtubule-associated filaments of LRRK2^{RCKW}[I2020T] in the presence of MLi-2.
a, Optimization of in vitro reconstituted microtubule-associated LRRK2^{RCKW} filaments. Top row, cryo-EM images of an individual microtubule (left) or individual microtubule-associated LRRK2^{RCKW} filaments. Middle, Diffraction patterns calculated from the images above. Arrowheads point to layer lines arising from the microtubule (white) or from the LRRK2^{RCKW} filaments (grey). Bottom, 2D class averages from multiple images equivalent to those shown at the top. The type of LRRK2^{RCKW} (WT, G2019S, or I2020T) and the presence or absence of MLi-2 during filament reconstitution are indicated on top. **b,c,** Schematic of data processing pipeline used to obtain the different reconstructions of the microtubule-associated LRRK2^{RCKW}[I2020T] filaments in the presence of MLi-2 (see Methods for details). Local resolution maps, Fourier Shell Correlation plots, and the distribution of voxel resolutions are shown for all reconstructions discussed in the text.

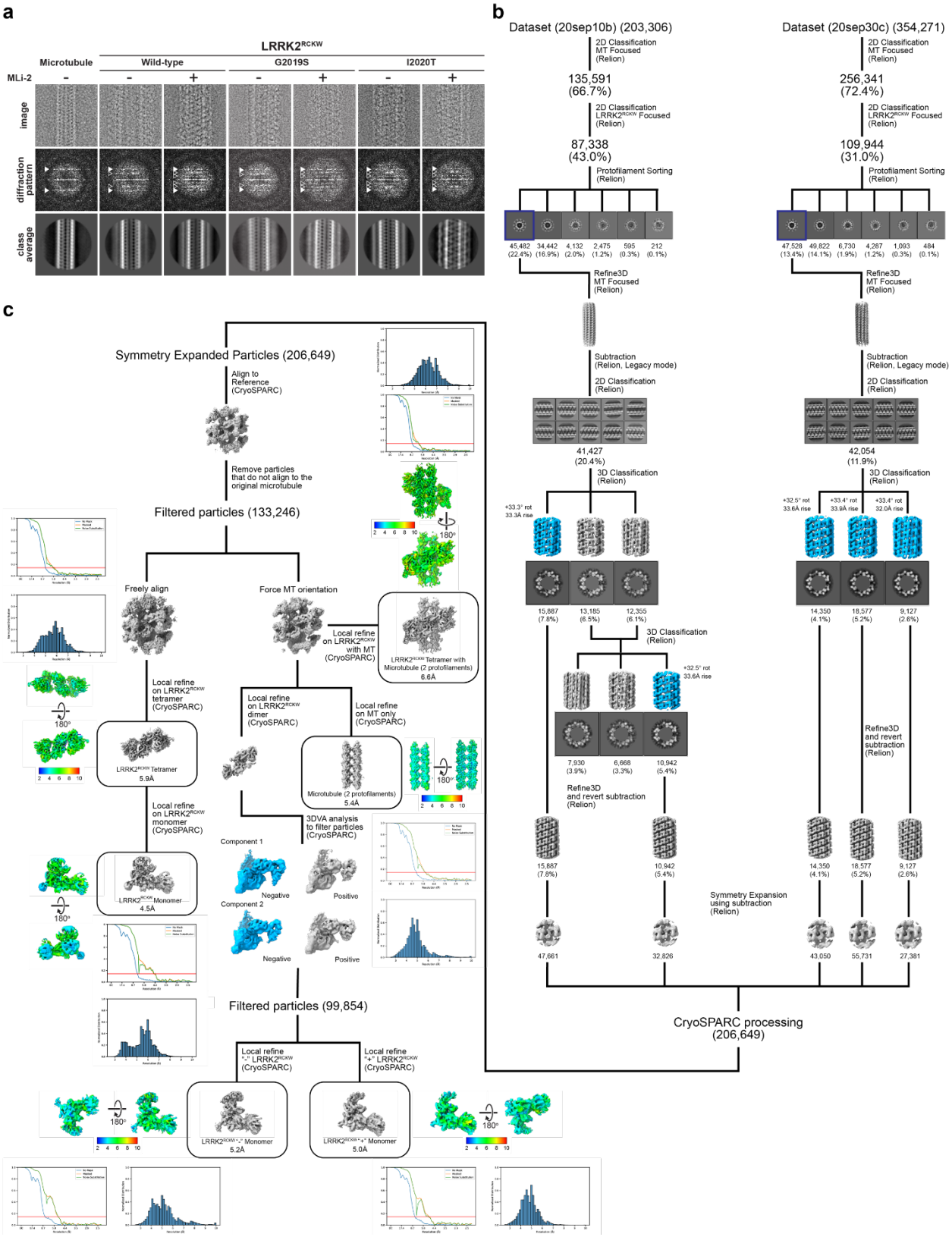
a
LRRK2RCKW
Microtubule
Wild-type
G2019S
I2020T
MLi-2
image
diffraction pattern
class average
b
Dataset (20sep10b) (203,306)
2D Classification MT Focused (Relion)
135,591 (66.7%)
2D Classification LRRK2RCKW Focused (Relion)
87,338 (43.0%)
Protofilament Sorting (Relion)
45,482 (22.4%)
34,442 (16.9%)
4,132 (2.0%)
2,475 (1.2%)
595 (0.3%)
212 (0.1%)
Refine3D MT Focused (Relion)
Subtraction (Relion, Legacy mode)
2D Classification (Relion)
41,427 (20.4%)
3D Classification (Relion)
+33.3° rot 33.3Å rise
15,887 (7.8%)
13,185 (6.5%)
12,355 (6.1%)
3D Classification (Relion)
+32.5° rot 33.6Å rise
7,930 (3.9%)
6,668 (3.3%)
10,942 (5.4%)
Refine3D and revert subtraction (Relion)
15,887 (7.8%)
10,942 (5.4%)
47,661
32,826
Dataset (20sep30c) (354,271)
2D Classification MT Focused (Relion)
256,341 (72.4%)
2D Classification LRRK2RCKW Focused (Relion)
109,944 (31.0%)
Protofilament Sorting (Relion)
47,528 (13.4%)
49,822 (14.1%)
6,730 (1.9%)
4,287 (1.2%)
1,093 (0.3%)
484 (0.1%)
Refine3D MT Focused (Relion)
Subtraction (Relion, Legacy mode)
2D Classification (Relion)
42,054 (11.9%)
3D Classification (Relion)
+32.5° rot 33.6Å rise
+33.4° rot 33.9Å rise
+33.4° rot 32.0Å rise
14,350 (4.1%)
18,577 (5.2%)
9,127 (2.6%)
Refine3D and revert subtraction (Relion)
14,350 (4.1%)
18,577 (5.2%)
9,127 (2.6%)
43,050
55,731
27,381
Symmetry Expansion using subtraction (Relion)
CryoSPARC processing (206,649)
c
Symmetry Expanded Particles (206,649)
Align to Reference (CryoSPARC)
Remove particles that do not align to the original microtubule
Filtered particles (133,246)
Freely align
Force MT orientation
Local refine on LRRK2RCKW with MT (CryoSPARC)
LRRK2RCKW Tetramer with Microtubule (2 protofilaments) 6.6Å
Local refine on LRRK2RCKW tetramer (CryoSPARC)
Local refine on LRRK2RCKW dimer (CryoSPARC)
Local refine on MT only (CryoSPARC)
LRRK2RCKW Tetramer 5.9Å
Microtubule (2 protofilaments) 5.4Å
Local refine on LRRK2RCKW monomer (CryoSPARC)
3DVA analysis to filter particles (CryoSPARC)
Component 1
Component 2
Negative
Positive
LRRK2RCKW Monomer 4.5Å
Filtered particles (99,854)
Local refine "-" LRRK2RCKW (CryoSPARC)
Local refine "+" LRRK2RCKW (CryoSPARC)
LRRK2RCKW "-" Monomer 5.2Å
LRRK2RCKW "+" Monomer 5.0Å
180°

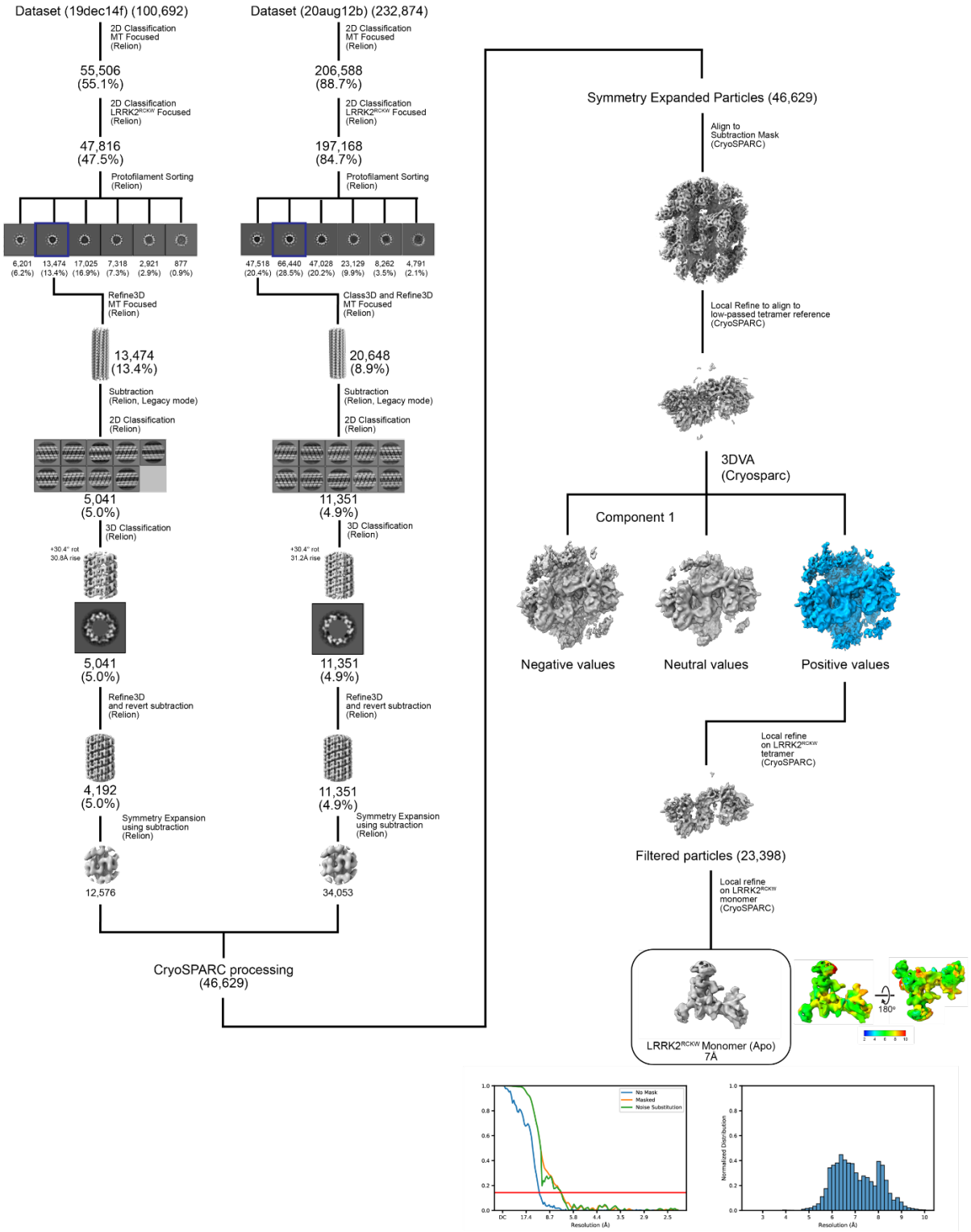

Figure A.2: Cryo-EM structure determination of microtubule-associated filaments of LRRK2^{RCKW}[I2020T] in the absence of MLi-2.

Schematic of data processing pipeline used to obtain the reconstruction of microtubule-associated LRRK2^{RCKW}[I2020T] filaments in the absence of MLi-2 (see Methods for details). Local resolution maps, Fourier Shell Correlation plots, and the distribution of voxel resolutions are shown.

Figure A.3: Structural analysis of microtubule-associated filaments of LRRK2^{RCKW}[I2020T]. **a,** A model for LRRK2^{RCKW}[I2020T] with a closed kinase, obtained by docking the individual domains into the cryo-EM map of LRRK2^{RCKW}[I2020T] filaments obtained in the presence of MLi-2, was docked into a cryo-EM map (7Å) of filaments obtained in the absence of the inhibitor (Fig. A.2). **b,** A model for LRRK2^{RCKW} with an open kinase (PDB:6VNO) was docked into the same map. The colored arrows in (a) and (b) highlight structural elements in the model that protrude from the density when the kinase is in an open conformation. **c,** The LRRK2^{RCKW} domains (ROC, COR-A, COR-B, Kinase N-lobe, Kinase C-lobe, WD40) (PDB:6VNO) were fitted individually into one of the monomers in the cryo-EM map of microtubule-bound LRRK2^{RCKW}[I2020T] formed in the presence of MLi-2. **d,** The LRRK2^{RCKW} portion of the AlphaFold model of LRRK2 was aligned to the COR-B domain in (c) and is shown here inside the same cryo-EM map. The colored arrows highlight regions where part of the model protrudes from the density. (Note: there is no arrow pointing to the loop in the ROC domain as this loop was not seen or modeled in the microtubule-bound structure.) **e,** The kinase from the AlphaFold model of LRRK2 was fitted into the cryo-EM map (same as in (d)) and is shown here superimposed on the N- and C-lobes of the kinase as fitted in (c). Note that while the C-lobes superimpose well, the N-lobe fitted individually in (c) is more closed than that modeled in the AlphaFold LRRK2. **f,** The N- and C-lobed of the kinase from the AlphaFold LRRK2 model were now fitted individually into the cryo-EM map (as in (c)), and are shown superimposed on the N- and C-lobes of LRRK2^{RCKW} from (a). The blue arrow between panels (e) and (f) highlights the downward movement of the N-lobe of AlphaFold's LRRK2 when the two lobes are fitted individually into the cryo-EM map. **g,** The LRRK2^{RCKW} domains (ROC, COR-A, COR-B, Kinase N-lobe, Kinase C-lobe, WD40) (PDB:6VNO) were fitted individually into the central dimer of the cryo-EM map of a tetramer of microtubule-bound LRRK2^{RCKW}[I2020T] obtained in the presence of MLi-2. **h,i,** Different closeup views of the map in (g), showing either (h) the ROC, COR-A, COR-B and kinase N-lobe from the LRRK2^{RCKW} model (PDB:6VNO), or (i) the corresponding portion from the structure of full-length LRRK2 (PDB:7LHT) docked as a single body into the cryo-EM map. The colored arrows highlight parts of the model that fit the cryo-EM density better when the domains are fitted in individually (h) rather than as a rigid body (i). **j,** Superposition of the model used in (i) and the COR-B domain from (h) to show that the differences among the ROC, COR-A and N-lobe of the kinase between the two models ((h) and (i)) is not due to major differences at the COR-B:COR-B interface, which is similar.

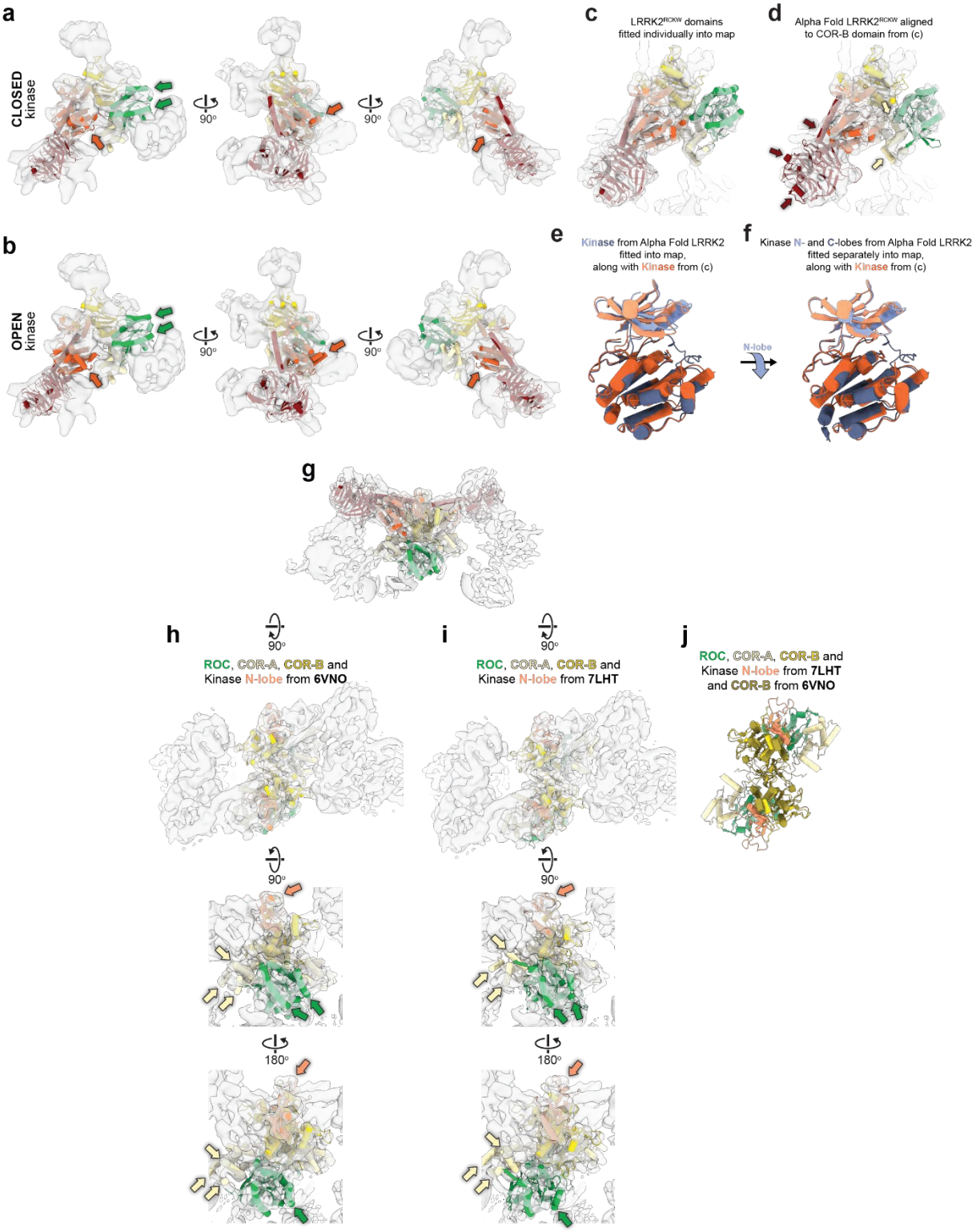
a
CLOSED kinase
90°
90°
b
OPEN kinase
90°
90°
c
LRRK2RCKW domains fitted individually into map
d
Alpha Fold LRRK2RCKW aligned to COR-B domain from (c)
e
Kinase from Alpha Fold LRRK2 fitted into map, along with Kinase from (c)
f
Kinase N- and C-lobes from Alpha Fold LRRK2 fitted separately into map, along with Kinase from (c)
N-lobe
g
h
90°
ROC, COR-A, COR-B and Kinase N-lobe from 6VNO
90°
180°
i
90°
ROC, COR-A, COR-B and Kinase N-lobe from 7LHT
90°
180°
j
ROC, COR-A, COR-B and Kinase N-lobe from 7LHT and COR-B from 6VNO

Figure A.4: Mechanism of LRRK2^{RCKW} binding to microtubules.
a, Representative images of 293T cells expressing GFP-LRRK2 (wild type or WD40 mutant as noted on top) and treated with DMSO or 500 nM MLi-2 for 2 hours (as noted at left). Scale bar is 10 μm. **b,c,** Rab10 phosphorylation in 293T cells overexpressing WT LRRK2 or LRRK2 carrying mutations in the WD40 domain. LRRK2[I2020T], which is known to increase Rab10 phosphorylation in cells, was tested as well. 293T cells were transiently co-transfected with the indicated plasmids encoding for GFP-LRRK2 (wild type or mutant) and GFP-Rab10, Thirty-six hours post-transfection the cells were lysed, immunoblotted for phospho-Rab10 (pT73), total GFP-Rab10, and total LRRK2, and developed with LI-COR Odyssey CLx imaging system. Quantification of data in (b) is shown in (c), normalized to wild-type, as mean ± s.e.m. Individual data points represent separate populations of cells obtained across at least three independent experiments. **d,** Representative images of 293T cells expressing GFP-LRRK2 (wild type or COR-B mutant as noted on top) and treated with DMSO or 500 nM MLi-2 for 2 hours (as noted at left). Scale bar is 10 μm. **e,f,** Rab10 phosphorylation in 293T cells overexpressing WT LRRK2 or LRRK2 carrying mutations in the COR-B domain. LRRK2[I2020T] was tested here as well. 293T cells were treated as in (b). Quantification of data in (e) is shown in (f), normalized to wild-type, as mean ± s.e.m. Individual data points represent separate populations of cells obtained across at least three independent experiments. **g,** Representative gel of supernatant from microtubule pelleting assay, used to generate the data shown in Figure 2.2e. **h**, Cryo-EM analysis of filament formation by LRRK2^{RCKW} mutants. Top row, cryo-EM images of an individual microtubule (left) or combinations of microtubules and LRRK2^{RCKW} mutants. Middle, Diffraction patterns calculated from the images above. Arrowheads point to layer lines arising from the microtubule (white) or from the LRRK2^{RCKW} filaments (grey). Bottom, 2D class averages from multiple images equivalent to those shown at the top. **i,** Example kymographs of single-molecule kinesin motility assays in the presence or absence of 50nM LRRK2^{RCKW} wild-type or indicated mutant. **j,** Cumulative distribution of run lengths for kinesin in the absence or presence of 50 nM LRRK2^{RCKW} (WT or carrying WD40 and/or WD40 and COR-B mutations). The run lengths were not significantly different between 50 nM wild-type and LRRK2^{RCKW} [S2345D], and were significantly between 50 nM wild-type LRRK2^{RCKW} and LRRK2^{RCKW} [R1731D/S2345D] and LRRK2^{RCKW} [R1731D] (Kruskal-Wallis test with Dunn's post hoc for multiple comparisons). Mean decay constants (tau) are shown. **k,** Comparison of 2D class averages from cryo-EM images of different LRRK2^{RCKW} mutants with the corresponding 2D projection from a LRRK2^{RCKW} molecular model (PDB: 6VNO). Two different views are shown for each mutant. **l,** Representative kinase reaction. Rab8a phosphorylation was measured via western blotting with a phospho-T72-specific Rab8a antibody, and total LRRK2^{RCKW} concentration was measured by Sypro Red staining. Phosphorylation reactions were terminated after 30 minutes. **m,** Quantification of data shown in (l). For each reaction, phospho-Rab8a band intensity (chemiluminescence) was divided by LRRK2^{RCKW} band intensity (Sypro red); for each western blot, an average normalized value was calculated for all replicates of unlabeled LRRK2^{RCKW}, and all data was then normalized to this value. **n,** Cumulative distribution of run lengths for kinesin in the absence or presence of 25 nM TMR-LRRK2^{RCKW}. The run lengths were significantly different between 0 nM and 25 nM TMR-LRRK2^{RCKW} (Mann-Whitney test). Mean decay constants (tau) are shown. Effect on kinesin motility is similar to previously shown unlabeled LRRK2^{RCKW}. **o, p,** Representative microtubule pelleting assay gel for LRRK2^{RCKW} in the presence of 100 mM and 150 mM sodium chloride. Cosedimentation was measured as depletion from supernatant. For each reaction, 200 nM LRRK2^{RCKW} was mixed with a given concentration of microtubules, microtubules were pelleted by high-speed spin, and a gel sample was taken of the supernatant. Quantification of data represented in (o) is shown in (p). Data are mean ± s.d., n=4. The solid line represents a hyperbolic curve fit to the data. **q,** Representative images of coverslip-tethered Alexa Fluor 488-labeled MTs (cyan) bound to 100 nM TMR-LRRK2^{RCKW} (magenta) in the presence of increasing concentrations of sodium chloride, used to generate the data in Figure 2.3d. **r,** Representative images of untreated (top) and

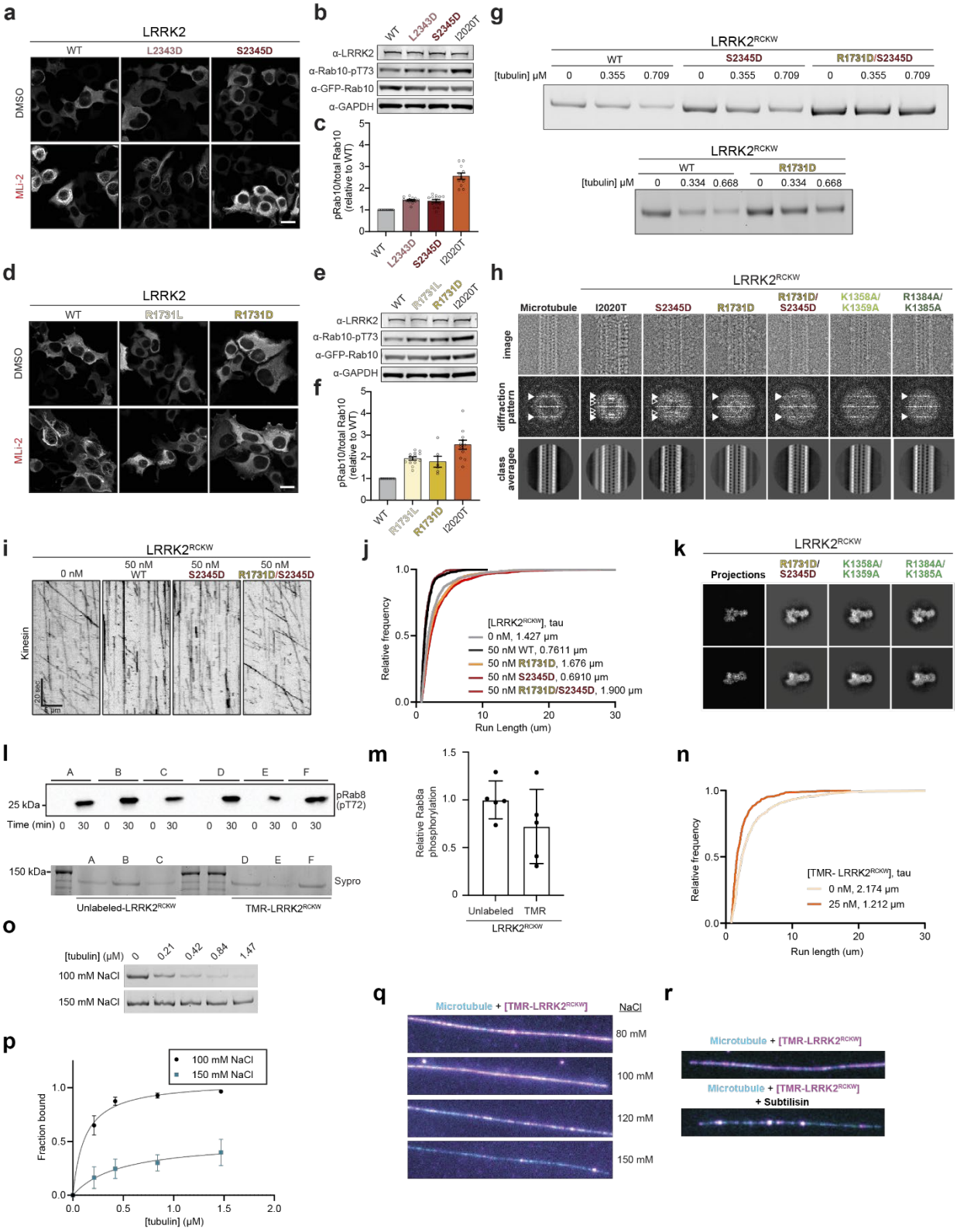

Figure A.4 continued: subtilisin-treated (bottom) Alexa Fluor 488-labeled MTs (cyan) bound to 50 nM TMR-LRRK2^{RCKW} (magenta), used to generate the data shown in Figure 2.3e.

Figure A.5: Basic residues within the LRRK2 RoC domain are not conserved in LRRK1 and are involved in LRRK2's binding to microtubules.
a, Cryo-EM structure determination of LRRK1^{RCKW}. **b,** Cumulative distribution of run lengths for kinesin in the absence or presence of 100 nM LRRK2^{RCKW} or LRRK1^{RCKW}. The run lengths were not significantly different between 0 nM and 100 nM LRRK1^{RCKW} conditions (Kruskal-Wallis test with Dunn's post hoc for multiple comparisons). **c,d,** Representative gel of supernatant from microtubule pelleting assay for 200 nM LRRK2^{RCKW} or LRRK1^{RCKW} with increasing tubulin concentrations. Quantification of data represented in (c) shown in (d). Data are mean ± s.d., n=4. The solid line represents a hyperbolic curve fit to the data. **e**, Sequence alignment of the ROC domains of LRRK2 and LRRK1 across several species made using Clustal Omega. Putative microtubule-contacting residues conserved in LRRK2 but not in LRRK1 are boxed**. f,** Close ups of the basic patches tested in this study, shown in the context of the cryo-EM maps for the "-" and "+" LRRK2^{RCKW} monomers in our reconstruction of the microtubule-associated filaments (Fig. 2.1e,f). The models shown here correspond to those in Fig. 2.5c. **g,** Example kymographs of kinesin motility in the presence of 100 nM LRRK2^{RCKW} (wild-type or K1358A/K1359A mutant). **h,** Cumulative distribution of run lengths for kinesin in the absence or presence of 100 nM LRRK2^{RCKW} (WT or carrying ROC mutation). The run lengths were significantly different between 100 nM LRRK2^{RCKW} wild-type and K1358A/K1359A mutant (Kruskal-Wallis test with Dunn's post hoc for multiple comparisons). Mean decay constants (tau) are shown. **i,** Representative images of 293T cells expressing GFP-LRRK2 (wild type or ROC mutant as noted on top) and treated with DMSO or 500 nM MLi-2 for 2 hours (as noted at left), corresponding to data plotted in Fig. 2.5f. Scale bar is 10 µm. **j,** Representative images of 293T cells expressing GFP-LRRK2 (I2020T, I2020T/ROC mutant, or I2020T/R1501W, as noted at left), corresponding to data plotted in Fig. 2.5g,i. Scale bar is 10 µm. **k,** Representative images of 293T cells expressing GFP-LRRK2 (wild type or R1501W mutant as noted on top) and treated with DMSO or 500 nM MLi-2 for 2 hours (as noted at left), corresponding to data plotted in Fig. 2.5h. Scale bar is 10 µm. **l,m,** Rab10 phosphorylation in 293T cells overexpressing WT LRRK2 or LRRK2 carrying indicated mutations in the ROC domain. LRRK2[I2020T], which is known to increase Rab10 phosphorylation in cells, was tested as well. 293T cells were transiently transfected with the indicated plasmids encoding for GFP-LRRK2 (wild type or mutant) and GFP-Rab10, Thirty-six hours post-transfection the cells were lysed, immunoblotted for phospho-Rab10 (pT73), total GFP-Rab10, and total LRRK2, and developed with LI-COR Odyssey CLx imaging system. Quantification of data in (l) is shown in (m), normalized to wild-type, as mean ± s.e.m. Individual data points represent separate populations of cells obtained across at least three independent experiments.

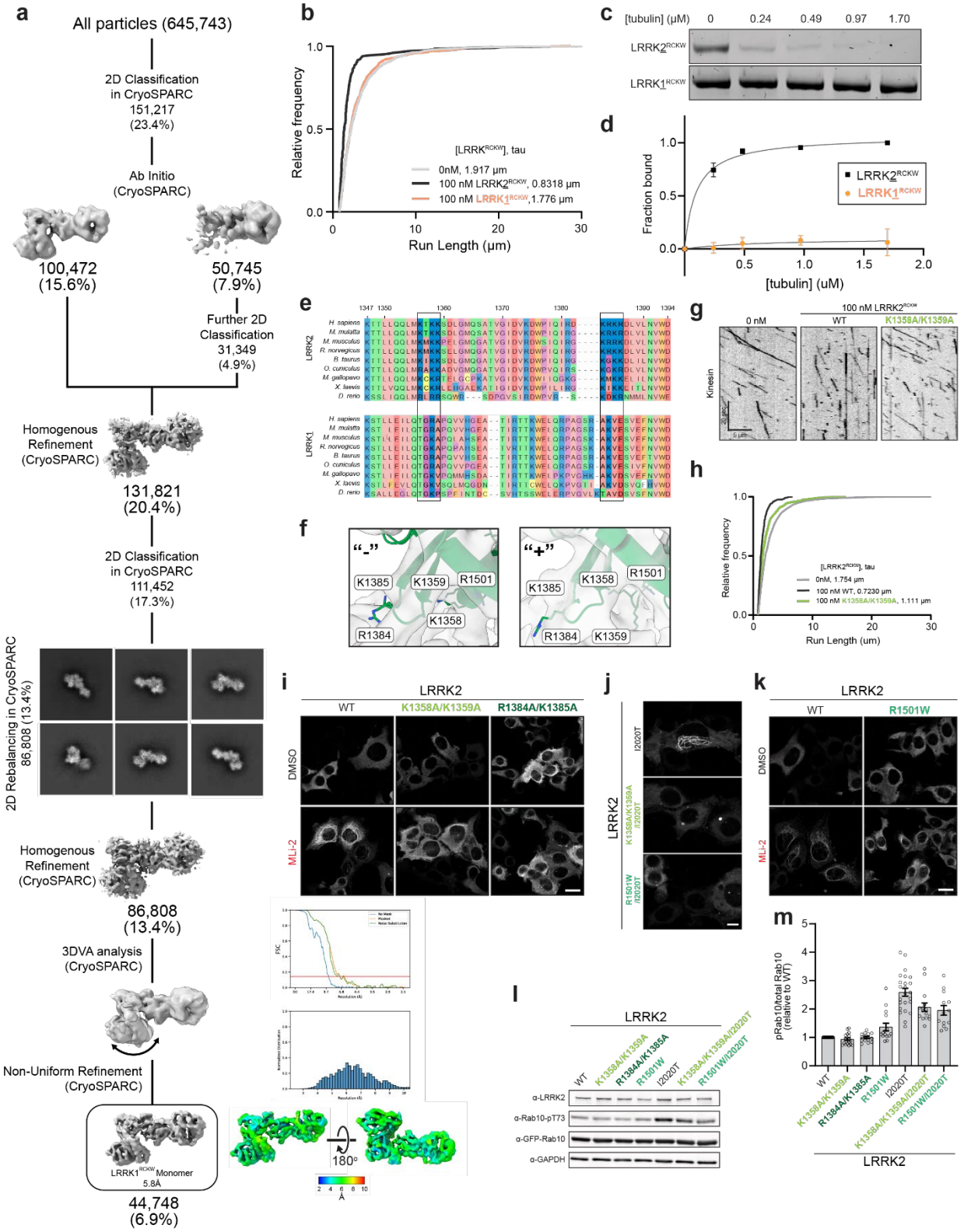
a
All particles (645,743)
2D Classification in CryoSPARC 151,217 (23.4%)
Ab Initio (CryoSPARC)
100,472 (15.6%)
50,745 (7.9%)
Further 2D Classification 31,349 (4.9%)
Homogenous Refinement (CryoSPARC)
131,821 (20.4%)
2D Classification in CryoSPARC 111,452 (17.3%)
2D Rebalancing in CryoSPARC 86,808 (13.4%)
Homogenous Refinement (CryoSPARC)
86,808 (13.4%)
3DVA analysis (CryoSPARC)
Non-Uniform Refinement (CryoSPARC)
LRRK1RCKW Monomer 5.8Å
44,748 (6.9%)
b
Relative frequency
Run Length (μm)
[LRRKRCKW], tau
0nM, 1.917 μm
100 nM LRRK2RCKW, 0.8318 μm
100 nM LRRK1RCKW,1.776 μm
c
[tubulin] (μM) 0 0.24 0.49 0.97 1.70
LRRK2RCKW
LRRK1RCKW
d
Fraction bound
[tubulin] (uM)
LRRK2RCKW
LRRK1RCKW
e
LRRK2
LRRK1
H. sapiens
M. mulatta
M. musculus
R. norvegicus
B. taurus
O. cuniculus
M. gallopavo
X. laevis
D. rerio
f
"-"
K1385
K1359
R1501
K1358
R1384
"+"
K1385
K1358
R1501
R1384
K1359
g
100 nM LRRK2RCKW
0 nM
WT
K1358A/K1359A
Kinesin
h
Relative frequency
Run Length (um)
[LRRK2RCKW], tau
0nM, 1.754 μm
100 nM WT, 0.7230 μm
100 nM K1358A/K1359A, 1.111 μm
i
LRRK2
WT
K1358A/K1359A
R1384A/K1385A
DMSO
MLi-2
j
LRRK2
I2020T
K1358A/K1359A I2020T
R1501W I2020T
k
LRRK2
WT
R1501W
DMSO
MLi-2
l
LRRK2
WT
K1358A/K1359A
R1384A/K1385A
R1501W
I2020T
K1358A/K1359A/I2020T
R1501W/I2020T
α-LRRK2
α-Rab10-pT73
α-GFP-Rab10
α-GAPDH
m
pRab10/total Rab10 (relative to WT)
WT
K1358A/K1359A
R1384A/K1385A
R1501W
I2020T
K1358A/K1359A/I2020T
R1501W/I2020T
LRRK2
180°

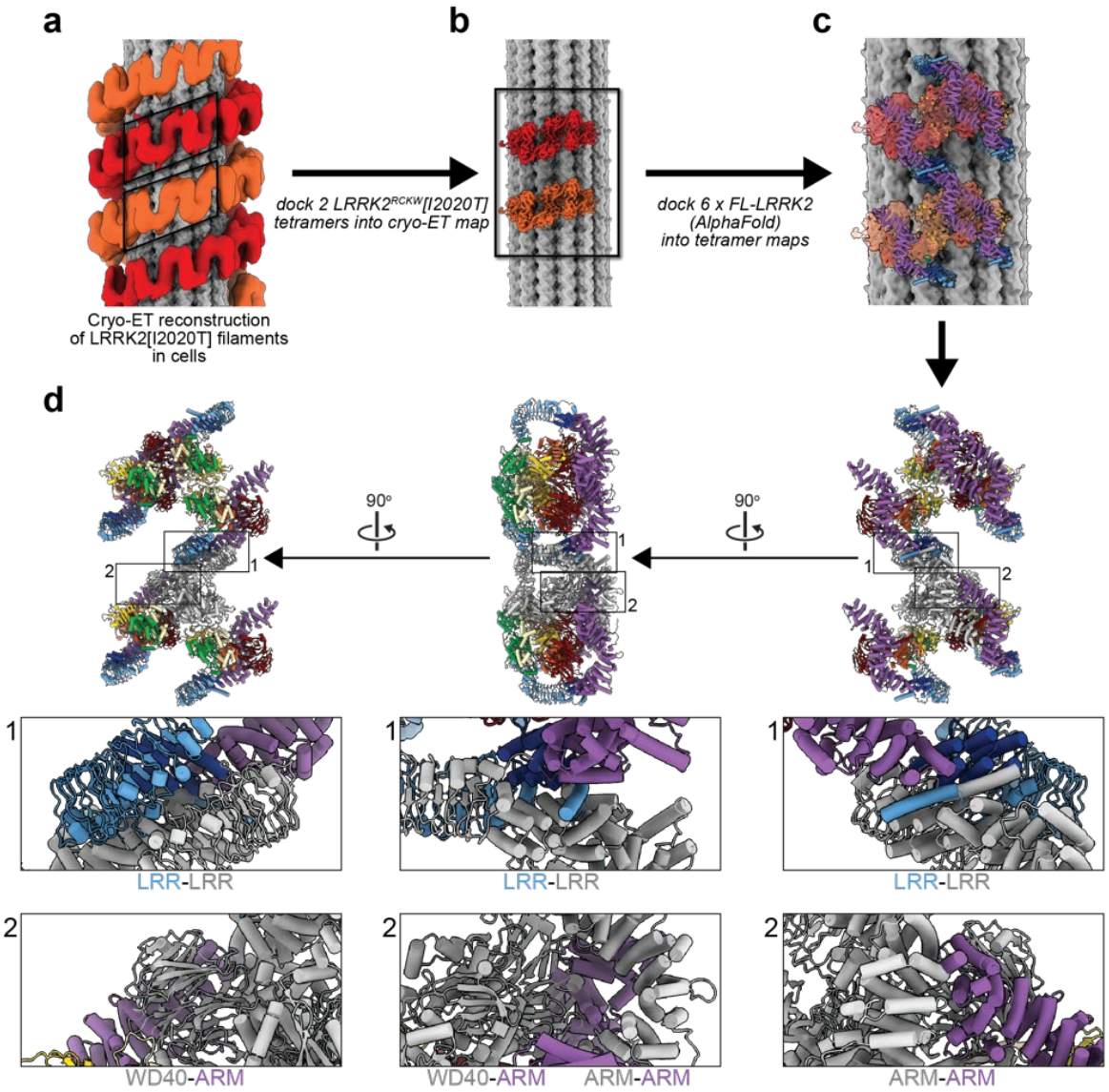

Figure A.6: Modeling of full-length LRRK2 into the cryo-ET reconstruction of microtubule-associated LRRK2[I2020T] filaments in cells.

a, Cryo-ET reconstruction of microtubule-associated LRRK2[I2020T] filaments in cells (Villa). The LRRK2 strands that form the double-helical filaments are shown in light and dark orange. For this figure, the density corresponding to the microtubule was replaced with a 10Å representation of a molecular model of a microtubule. **b**, We docked copies of our 5.9Å reconstruction of a LRRK2^{RCKW}[I2020T] tetramer from the microtubule-associated filaments (Fig. 2.1b,c) into the regions indicated by the parallelograms in (a). **c**, Next, we docked two copies of the AlphaFold model of full-length LRRK2 (AF-Q5S007), which is in the active state, as is the case with LRRK2^{RCKW}[I2020T] in our filaments, into each of the 5.9Å maps. The pairs of AlphaFold models in each map correspond to the COR-B:COR-B dimer. This panel shows a region corresponding to the rectangle in (b). **d**, Three different views of the models docked in (c). Below each model, close-ups show regions where adjacent filaments clash. These clashes involve a domain in the N-terminal repeats of one LRRK2, and either the same domain on another LRRK2, or the WD40 domain. For clarity, one of the LRRK2's is shown in grey instead of the standard rainbow coloring.

A.2 Supplementary tables for Chapter 2

Table A.1: Summary of cryo-EM data collection and cryo-EM structure determination

	LRRK2^{RCKW} + MT +MLi-2 (Helical)	**LRRK2^{RCKW} + MT +MLi-2 (Tetramer only)**	**LRRK2^{RCKW} + MT +MLi-2 (Tetramer + MT)**
	EMD-25649 EMPIAR-10925	EMD-25664 EMPIAR-10925	EMD-25658 EMPIAR-10925
Data Collection			
Microscope	Talos Arctica	Talos Arctica	Talos Arctica
Camera	K2 summit	K2 Summit	K2 Summit
Magnification	36,000	36,000	36,000
Voltage (kV)	200	200	200
Total electron exposure (e-/Å^2)	55	55	55
Defocus Range (um)	0.5-2.5	0.5-2.5	0.5-2.5
Pixel Size (Å/pixel)	1.16	1.16	1.16
Number of dataset (no.)	2	2	2
Reconstruction			
Total Extracted picks (no.)	354,271	206,649 (symmetry expanded)	206,649 (symmetry expanded)
Final Particles (no.)	14,350	133,246	133,246
Symmetry	+32.5° rot, 33.3Å rise	C1	C1
Resolution (global) (Å) FSC 0.143	18	5.9	6.6
Local resolution range (Å)	N/A	3.5-9	3.7-9.5
Map sharpening *B*-factor	N/A	-339	-326

	LRRK2^{RCKW} + MT +MLi-2 (Microtubule only)	**LRRK2^{RCKW} + MT Apo (Monomer only)**	**LRRK1^{RCKW}**
	EMD-25908 EMPIAR-10925	EMD-25674 EMPIAR-10924	EMD-25672 EMPIAR-10921
Data Collection			
Microscope	Talos Arctica	Talos Arctica	Talos Arctica
Camera	K2 summit	K2 Summit	K2 Summit
Magnification	36,000	36,000	36,000
Voltage (kV)	200	200	200
Total electron exposure (e-/Å^2)	55	50-55	55
Defocus Range (um)	0.5-2.5	0.5-2.5	1.2-1.8
Pixel Size (Å/pixel)	1.16	1.16	1.16
Number of dataset (no.)	2	2	4
Reconstruction			
Total Extracted picks (no.)	206,649 (symmetry expanded)	46,629 (symmetry expanded)	645,743
Final Particles (no.)	133,246	23,398	44,748
Symmetry	C1	C1	C1
Resolution (global) (Å) FSC 0.143	5.4	7.0	5.8
Local resolution range (Å)	2.6-9.0	4.8-10.0	3.5-10
Map sharpening *B*-factor	-235	-293	-327

Table A.1: Summary of cryo-EM data collection and cryo-EM structure determination, continued

	LRRK2^{RCKW} + MT +MLi-2 (Focused on Kinase)	**LRRK2^{RCKW} + MT +MLi-2 (Minus end)**	**LRRK2^{RCKW} + MT +MLi-2 (Plus end)**
		7THY	7THZ
	EMD-25897	EMD-25906	EMD-25907
	EMPIAR-10925	EMPIAR-10925	EMPIAR-10925
Data Collection			
Microscope	Talos Arctica	Talos Arctica	Talos Arctica
Camera	K2 summit	K2 Summit	K2 Summit
Magnification	36,000	36,000	36,000
Voltage (kV)	200	200	200
Total electron exposure (e-/Å^2)	55	55	55
Defocus Range (um)	0.5-2.5	0.5-2.5	0.5-2.5
Pixel Size (Å/pixel)	1.16	1.16	1.16
Number of dataset (no.)	2	2	2
Reconstruction			
Total Extracted picks (no.)	206,649 (symmetry expanded)	206,649 (symmetry expanded)	206,649 (symmetry expanded)
Final Particles (no.)	133,246	99,854	99,854
Symmetry	C1	C1	C1
Resolution (global) (Å) FSC 0.143	4.5	5.2	5.0
Local resolution range (Å)	3.0-8.0	2.6-9.0	2.9-7.0
Map sharpening *B*-factor	-146	-200	-200
Refinement			
Initial model used	N/A	Q5S007 (AlphaFold)	Q5S007 (AlphaFold)
Model resolution (Å)	N/A	5.4 (average)	5.3 (average)
Resolution method	N/A	Q-score	Q-score
Model resolution range (Å)	N/A	3.0-8.6	3.5-8.0
Model refinement package	N/A	Rosetta, Isolde	Rosetta, Isolde
Number of models	N/A	5	5
Nonhydrogen atoms	N/A	1584 (per model)	1584 (per model)
Protein residues	N/A	194 (per model)	194 (per model)
B factors (Å^2)			
Protein residues	N/A	-219 (average)	-216 (average)
R.m.s. deviations			
Bond Lengths (Å)	N/A	0.019 (average)	0.020 (average)
Bond angles (°)	N/A	1.907 (average)	2.023 (average)
Validation			
MolProbity score	N/A	1.49 (average)	1.54 (average)
Clashscore	N/A	3.52 (average)	3.96 (average)
Poor rotamers (%)	N/A	0 (average)	0 (average)
Ramachandran plot			
Favored (%)	N/A	94.5 (average)	94.6 (average)
Allowed (%)	N/A	4.9 (average)	4.8 (average)
Disallowed (%)	N/A	0.6 (average)	0.6 (average)
Map CC (*CCmask*)	N/A	0.63 (average)	0.61 (average)

Table A.2: Parameters observed for LRRK2^{RCKW} filaments compared to published LRRK2FL filaments.

Filament Type	Rotation (°)	Z-rise (Å)
LRRK2FL/11-pf[38]	33.3	31.5
LRRK2FL/12-pf[38]	30.3	28.8
LRRK2RCKW/11-pf (Class 1)	33.4	33.3
LRRK2RCKW/11-pf (Class 2)	32.5	33.6
LRRK2RCKW/11-pf (Class 3)	33.4	33.9
LRRK2RCKW/11-pf (Class 4)	33.4	32.0
LRRK2RCKW/12-pf (Class 1)	30.4	30.8
LRRK2RCKW/12-pf (Class 2)	30.4	31.2

Appendix A, in full, is a reprint of the material as it appears in Structural basis for Parkinson's Disease-linked LRRK2's binding to microtubules. David M. Snead*, Mariusz Matyszewski*, Andrea M. Dickey*, Yu Xuan Lin, Andres E. Leschziner, Samara L. Reck-Peterson, bioRxiv, 2022. The dissertation author was a co-author of this paper. * denotes equal contributions.

APPENDIX B: EXPLORING THE ROLE OF CARGO ADAPTORS IN BI-DIRECTIONAL MICROTUBULE-BASED MOTOR TRANSPORT

B.1 Brief introduction to microtubule-based motor transport

The microtubule cytoskeleton and its motors are responsible for the intracellular organization of organelles, vesicles, proteins, and mRNAs. Spatial and temporal distribution of intracellular components are vital for cellular development and survival. Microtubules are polarized structures with “minus-ends” generally located near the nucleus and “plus-ends” located near the cell periphery. Cellular transport along the microtubule cytoskeleton is accomplished by motor proteins, cytoplasmic dynein-1 (“dynein” here) and kinesins. Of the 45 kinesins in the human genome, ~15 of them transport cargoes towards the microtubule plus-ends while a single dynein is responsible for all minus-end directed cargo transport.

The importance of the microtubule cytoskeleton and associated motor proteins is underscored by the fact that mutations in each component of the system are linked to neurological disease in humans. Mutations in dynein cause spinal muscle atrophy, Charot Marie Tooth type 2 peripheral neuropathy, and malformation of cortical development[123–125]. Similarly, mutations in the activating adaptor BICD2 causes spinal muscle atrophy[126]. Mutations in dynactin subunits have been linked to motor neuron disease and Perry Syndrome[127,128]. Thus, it is likely that regulation of motor protein complexes, as well as their cargoes, play important roles in the development and progression of neurological disorders in humans.

In addition, non-motor microtubule-associated proteins (MAPs) help to maintain the delicate distribution of intracellular components by stabilizing and destabilizing the microtubule cytoskeleton and disrupting or enhancing the motility of motor proteins[129,130]. Mutations in MAPs are also linked to a variety of neurological diseases. Understanding the basic mechanisms of transport and how improper transport arises will deepen our understanding of these human diseases.

Dynein's function is regulated on multiple levels. Dynein holoenzyme is a 1.4 MDa homodimer composed of six polypeptide chains, each present as dimers. Human dynein does not move processively on its own, rather it requires the formation of a tripartite complex with the dynactin complex and a coiled-coil-containing activating adaptor to achieve motility[131,132] (Fig. B.1A). Dynactin is a large multi-subunit complex (1.2 MDa) that is made up of 23 subunits (constituting 11 proteins). Dynactin has been implicated in almost every dynein-dependent role in cells[133]. Though dynactin is necessary for human dynein processivity, it is not sufficient to induce motility in vitro[131,132]. The final component of the processive dynein complex is an activating adaptor. There are currently ten confirmed activating adaptors as well as multiple candidate activating adaptors. These activating adaptors strengthen the weak dynein/dynactin interaction and link dynein to its cargo. Though there is no sequence homology between all activating adaptors, they share common structural features. These features include an extended coiled-coil region (>200 residues), an N-terminal region capable of binding the dynein light intermediate chain (DLIC), and a binding site in their C-terminus to link the adaptors to their cargoes (Fig. B.1B). Additionally, these activating adaptors can act as scaffolds for opposite polarity motors.

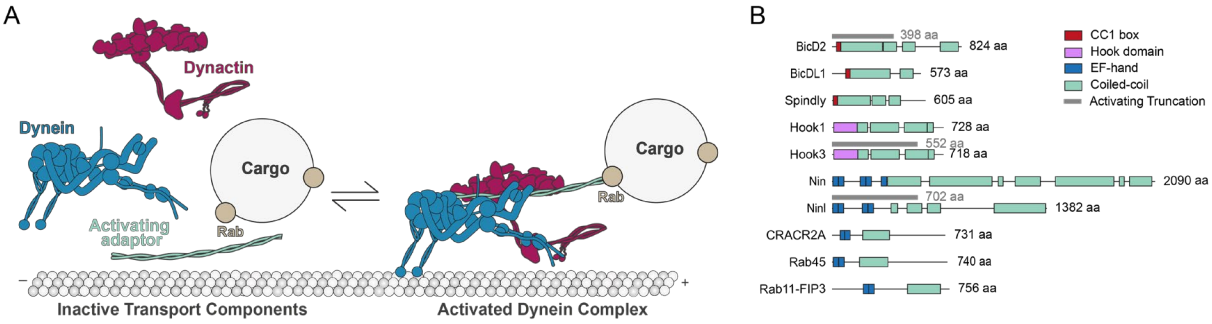

Figure B1: Dynein activation and activating adaptors
(A) Schematic of the current model of activation of dynein-mediated transport by the formation of the dynein/dynactin/activating adaptor complex. Dynein is responsible for transporting of hundreds of distinct cargoes including vesicles, organelles, and mRNAs. It remains unknown how these complexes form and if different mechanisms are used by dynein's various activating adaptors. **(B)** Domain structure of known dynein activating adaptors. These proteins share characteristic long-stretches of coiled-coil regions and proposed or known dynein light intermediate chain binding regions (CC1 box, Hook domain, amino-terminal EF-hand regions). Truncations that have previously been shown to activate dynein motility are indicated in grey.

Though dynein and kinesin motors each move cargo unidirectionally along microtubules, cargoes within the cell move bidirectionally[134–137]. Bidirectional cargo transport may be achieved by the motor "coordination model," in which small adaptors or the cargo itself can activate or inactivate opposing dyneins and kinesins[138,139]. In the following work we used the dynein activating adaptor, Hook3, as a model system to determine if a physiological scaffold can link the opposite-polarity motors dynein and KIF1C (a kinesin-3 family member). Using single-molecule in vitro reconstitution techniques we show that Hook3 can scaffold dynein/dynactin and KIF1C, resulting in motility either towards the microtubule minus or plus end, without directional switching.

B.2 Hook3 is a scaffold for the opposite-polarity microtubule-based motors cytoplasmic dynein-1 and KIF1C

B.2.1 Contributions

Agnieszka A. Kendrick, William B. Redwine, Andrea M. Dickey, and Samara L. Reck-Peterson designed the experiments. Agnieszka A. Kendrick, William B. Redwine, Andrea M. Dickey, Phuoc T. Tran, Laura Pontano Vaites, and Monica Dzieciatkowska performed the experiments. Agnieszka A. Kendrick, William B. Redwine, Andrea M. Dickey, Laura Pontano Vaites, J. Wade Harper, and Samara L. Reck-Peterson interpreted the data.

B.2.2 Abstract

The unidirectional and opposite-polarity microtubule-based motors, dynein and kinesin, drive long-distance intracellular cargo transport. Cellular observations suggest that opposite-polarity motors may be coupled. We recently identified an interaction between the cytoplasmic dynein-1 activating adaptor Hook3 and the kinesin-3 KIF1C. Here, using in vitro reconstitutions with purified components we show that KIF1C and dynein/dynactin can exist in a complex scaffolded by Hook3. Full-length Hook3 binds to and activates dynein/dynactin motility. Hook3

also binds to a short region in the “tail” of KIF1C, but unlike dynein/dynactin, this interaction does not activate KIF1C. Hook3 scaffolding allows dynein to transport KIF1C towards the microtubule minus end, and KIF1C to transport dynein towards the microtubule plus end. In cells, KIF1C can recruit Hook3 to the cell periphery, although the cellular role of the complex containing both motors remains unknown. We propose that Hook3’s ability to scaffold dynein/dynactin and KIF1C may regulate bidirectional motility, promote motor recycling, or sequester the pool of available dynein/dynactin activating adaptors.

B.2.3 Introduction

In many eukaryotic organisms microtubules and the motors that move on them, kinesins and dynein, power the long-distance transport of intracellular cargos. Microtubules are polar structures with their “minus ends” typically located near microtubule organizing centers. Cytoplasmic dynein-1 (“dynein” here) moves cargos towards the microtubule minus end, while kinesins that transport cargos over long distances, such as those in the kinesin-1, -2 and -3 families, move cargos towards the microtubule plus end[140]. The cargos of these motors include organelles, other membrane-bound compartments, and large RNA and protein complexes[92,141].

In many cases, these cargos can be observed rapidly switching directions. For example, in filamentous fungi endosomes move bidirectionally along microtubules[142–144] and also drive the bidirectional motility of hitchhiking cargos such as peroxisomes, lipid droplets, endoplasmic reticulum, and ribonucleoprotein complexes[145–147]. In human cells, examples of cargos that move bidirectionally on microtubules include lysosomes[134], secretory vesicles[135,136], autophagosomes[137], and protein aggregates[148,149]. Purified cargos, such as pigment granules[150] and neuronal transport vesicles[134] exhibit bidirectional motility along microtubules in vitro. Together, these data suggest that opposite polarity motors are present on the same cargos in many organisms and for many cargo types. There is also evidence that kinesin localizes dynein

to microtubule plus ends[151–154], suggesting that these motors could be directly coupled. Given these data, a central question is to determine how opposite polarity motors are scaffolded.

We and others have taken a “bottom-up” approach to study teams of motors by designing artificial scaffolds bearing opposite-polarity motors. For example, dynein and kinesin motors can be scaffolded by DNA origami[155] or short DNA oligomers[156]. Such approaches allow the basic biophysical properties of motor teams to be dissected. However, studies using physiological motor pairs and scaffolds are lacking, primarily because these scaffolds have not been identified or well characterized. One exception is our recent reconstitution of dynein transport to microtubule plus ends by a kinesin[107], a process that occurs in vivo in yeast cells[157]. In this system, cytoplasmic dynein-1 and the kinesin Kip2 required two additional proteins for scaffolding and both motors were regulated so that Kip2-driven plus-end-directed motility prevails[107,158].

How are opposite polarity motors scaffolded in mammalian cells? A group of proteins called “dynein activating adaptors” are emerging as candidate scaffolds[92,159]. Processive dynein motility requires an activating adaptor as well as the dynactin complex[131,132]. Examples of activating adaptors include the Hook (Hook1, Hook2, and Hook3), BicD (BicD1, BicD2, BicDL1, and BicDL2), and ninein (Nin and Ninl) families of proteins[92,97,131,132,159]. One piece of evidence supporting the role of activating adaptors as scaffolds is our recent identification of an interaction between Hook3 and the kinesin KIF1C using a proteomics approach[97]. KIF1C is a plus-end-directed member of the kinesin-3 family[160,161], which has been implicated in the plus-end-directed transport of secretory vesicles that move bidirectionally in multiple cell types[136,162]. The dynein activating adaptors BICD2 and BICDL1 may also interact with kinesin motors[136,163,164]. However, it is not known whether the interactions between dynein activating adaptors and kinesins are direct, if dynein and kinesin binding is achieved simultaneously, or if the dynein activating adaptors can support motility in both directions.

Here we use Hook3 as a model system to determine if a physiological scaffold can link the opposite polarity motors dynein and KIF1C to allow for motility in both the plus- and minus-

end directions. To do so, we perform complex in vitro reconstitutions with purified human dynein (1.4 MDa and 12 subunits), dynactin (1.1 MDa and 23 subunits), full-length Hook3 (166 KDa as a dimer; see below), full-length KIF1C (246 KDa as a dimer; see below), and microtubules. We identify the binding site for Hook3 on KIF1C and show that while Hook3 activates motility when added to dynein/dynactin, it does not activate motility when added to KIF1C. We also show that Hook3 scaffolds dynein/dynactin and KIF1C, resulting in motility towards either the microtubule plus- or minus-end without directional switching. In cells, we show that KIF1C recruits Hook3 to the cell periphery and that this requires the Hook3 binding site we identified. Together, this represents the first example of a fully reconstituted physiological scaffold with opposite polarity motors and identifies an excellent model system to continue to understand the complicated process of bidirectional motility seen in cells.

B.2.4 Results

Endogenous KIF1C and Hook3 interact specifically

We identified the Hook3-KIF1C interaction using a proximity-dependent biotinylation technique that relies on a promiscuous biotin ligase (BioID) with BioID-tagged Hook3[97,111]. KIF1C is a kinesin-3 family member that is closely related to KIF1A and KIF1B[160]. It contains an amino-terminal motor domain and carboxy-terminal “tail” domain with several regions of predicted coiled-coil, a forkhead-associated domain (FHA), and a proline-rich region[165] (Fig. B.2A). KIF1C interacts with the carboxy-terminus of Hook3[97], while dynein and dynactin interact with Hook3s amino-terminus[131] (Fig. B.2A).

Here, we began by performing a BioID experiment with BioID-tagged KIF1C to identify the protein interactome of KIF1C. To perform this experiment with near-endogenous expression levels of KIF1C (to avoid artifacts of protein overexpression), we generated KIF1C knockout 293T human cell lines using CRISPR/Cas9-based gene editing. Co-transfection of 293T cells with Cas9 and guides specific for exon 3 of the KIF1C genomic sequence or empty vector, followed by clonal

selection, yielded two clones with full depletion of KIF1C and a control cell line (Fig. B.2B). We then infected one of these cell lines (KIF1CKO, clone #1) and the control cell line with retroviral KIF1C-BioID-3XFLAG or BioID-3XFLAG plasmids driven by the murine stem cell virus (MSCV) promoter to generate stable cells expressing exogenous KIF1C-BioID or BioID alone[166]. The KIF1C protein expression levels in these cells were similar to endogenous KIF1C expression levels in 293T cells (Fig. B.2C). To perform BioID experiments, we lysed cells after growth in biotin-containing medium and isolated biotinylated proteins using streptavidin beads. Biotinylated proteins were identified by mass spectrometry and significant "hits" were determined using a label-free proteomics approach by comparison to a BioID alone control[97,167]. Proteins not present in the BioID control or with an enrichment ratio greater than 3-fold and a p-value above 0.05 relative to the control were considered significant hits. One of the top hits from this experiment was Hook3 (Fig. B.2D). We did not detect other dynein activating adaptors, except for Hook1, which was a significant hit, but had a relatively low peptide count.

To further characterize the interaction between KIF1C and Hook3, we immunoprecipitated endogenous KIF1C and Hook3 from 293T cells. Immunoblots with antibodies against Hook3 and KIF1C demonstrated that these proteins co-precipitate (Fig. B.2E). Because there are three different HOOK homologs in the human genome (HOOK1, HOOK2, and HOOK3) and because we detected both Hook3 and Hook1 in our KIF1C BioID data, we next used immunoprecipitation experiments to confirm these interactions and to determine if KIF1C interacted with the third Hook homolog, Hook2. We expressed each Hook homolog with an amino-terminal HaloTag and a carboxy-terminal 3XFLAG tag in 293T cells. Immunoprecipitation of each tagged Hook protein, followed by immunoblots for endogenous KIF1C, revealed that endogenous KIF1C co-precipitates with Hook3, but not Hook1 or Hook2 (Fig. B.2F). The presence of Hook1 in our KIF1C BioID dataset was likely due to heterodimerization of Hook1 with Hook3, rather than Hook1 interacting with KIF1C, as in our previous BioID experiments with Hook1 and Hook3, we detected Hook1 in Hook3 datasets and vice versa[97]. This led us to propose that these proteins may

Figure B.2: Endogenous Hook3 and KIF1C interact specifically.
(A) Domain organization of KIF1C and Hook3. KIF1C contains an amino-terminal kinesin motor domain and regions of predicted coiled coil (CC), a forkhead-associated domain (FHA) and proline-rich (P-rich) region in its carboxy-terminal "tail". Hook3 is largely made up of regions of predicted coiled coil and contains dynein/dynactin and KIF1C binding regions (McKenney et al., 2014; Redwine et al., 2017). The Hook domain, which is also involved in dynein/dynactin binding (Schroeder and Vale, 2016) is indicated. **(B)** 293T cells were transfected with control CRISPR-Cas9 (CTRL) or with CRISPR-Cas9-gRNA specific for KIF1C. KIF1C knockout (KIF1CKO) was confirmed in two different clones by immunoblotting with an anti-KIF1C antibody. Clone #1 was selected for further assays. ß-Actin provided a loading control. **(C)** KIF1CKO cells were infected with viral particles encoding MSCV-driven KIF1C-BioID-3XFLAG plasmid to obtain near-endogenous KIF1C-BioID protein expression levels. Immunoblots were performed using the indicated antibodies. ß-Actin provided a loading control. **(D)** A volcano plot showing enrichment versus significance of proteins identified in KIF1C-BioID experiments relative to control (BioID alone) experiments. Proteins not present in the BioID control or with an enrichment ratio greater than 3-fold and a p-value above 0.05 relative to the control (dashed red lines) were considered significant hits. KIF1C, Hook3 and Tc-Tex-1 (DYNLT1, a dynein light chain) are marked in red. **(E)** Immunoprecipitation (IP) of endogenous Hook3 and KIF1C with the indicated antibodies from 293T cells. Immunoblots were performed with anti-Hook3 or KIF1C antibodies. **(F)** Human Hook1, Hook2, and Hook3 tagged with the HaloTag on their amino-termini and 3XFLAG on their carboxy-termini were transiently transfected into 293T cells and immunoprecipitated (IP) with FLAG affinity resin. Immunoblots were performed with anti-KIF1C and FLAG antibodies. 3XFLAG-sfGFP (super folder GFP) provided a control (CTRL). Protein molecular weight markers are shown in kilodaltons on the anti-FLAG immunoblot. **(G)** Human KIF1A, KIF1B, KIF1C, KIF5A, KIF5B, and KIF5C were each tagged with BioID-3XFLAG on their carboxy-termini and stably expressed in 293T cells. Tagged proteins were immunoprecipitated (IP) with FLAG affinity resin and immunoblots were performed with anti-Hook3 and FLAG antibodies. BioID-3XFLAG provided a control (CTRL). Protein molecular weight markers are shown in kilodaltons on the anti-FLAG immunoblot.

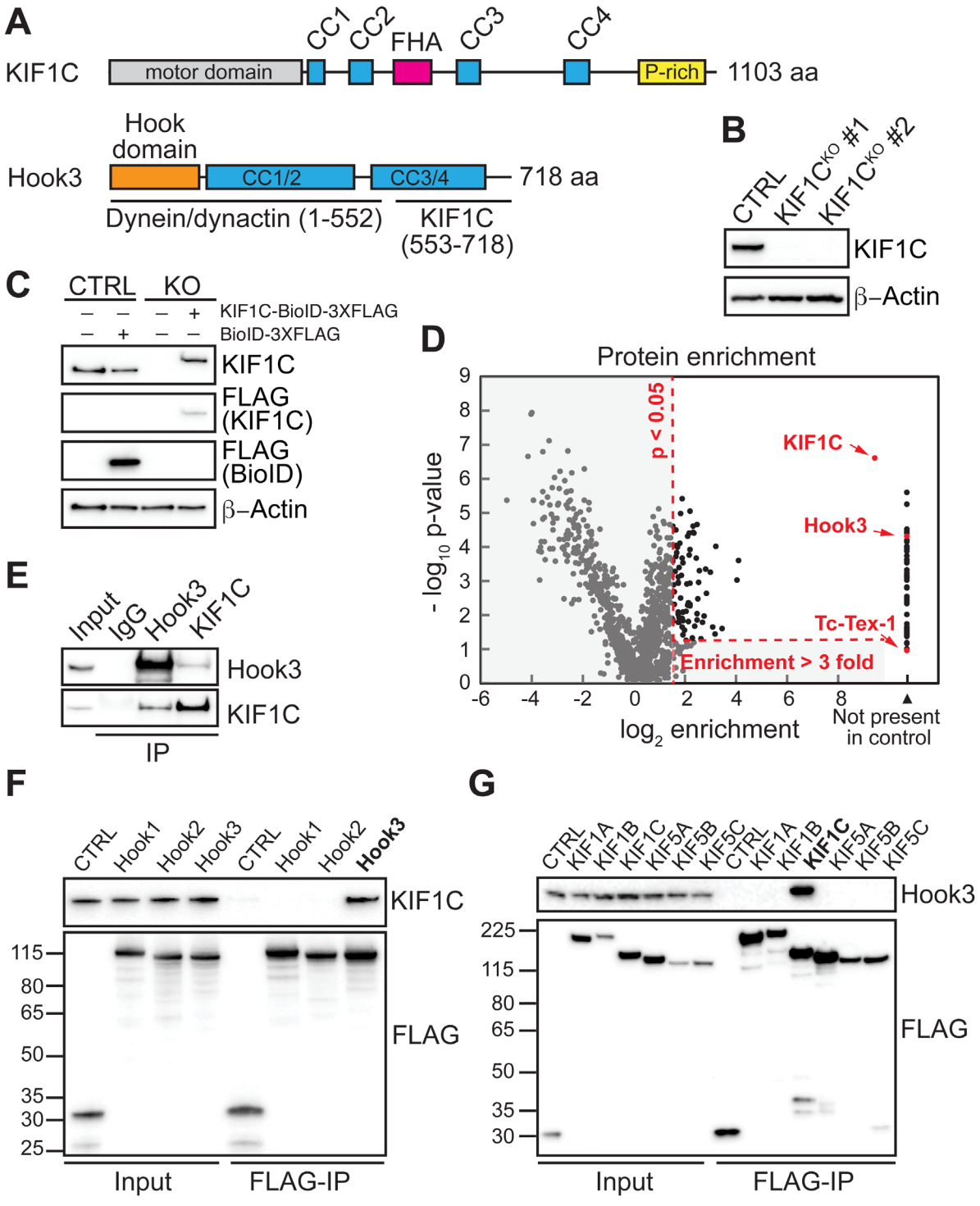
A
KIF1C
motor domain
CC1
CC2
FHA
CC3
CC4
P-rich
1103 aa
Hook3
Hook domain
CC1/2
CC3/4
718 aa
Dynein/dynactin (1-552)
KIF1C (553-718)
B
CTRL
KIF1C^KO #1
KIF1C^KO #2
KIF1C
β–Actin
C
CTRL
KO
KIF1C-BioID-3XFLAG
BioID-3XFLAG
KIF1C
FLAG (KIF1C)
FLAG (BioID)
β–Actin
D
Protein enrichment
- log10 p-value
log2 enrichment
p < 0.05
KIF1C
Hook3
Tc-Tex-1
Enrichment > 3 fold
Not present in control
E
Input
IgG
Hook3
KIF1C
Hook3
KIF1C
IP
F
CTRL
Hook1
Hook2
Hook3
KIF1C
FLAG
Input
FLAG-IP
G
CTRL
KIF1A
KIF1B
KIF1C
KIF5A
KIF5B
KIF5C
Hook3
FLAG
Input
FLAG-IP

heterodimerize under some conditions. This is also consistent with a previous study that suggested possible heterodimerization between Hook family members[168].

We next asked if Hook3 specifically interacts with KIF1C. The two most closely related kinesin-3 family members to KIF1C are KIF1A and KIF1B[160]. In addition, the kinesin-1s, KIF5A, KIF5B, and KIF5C, are well-characterized cargo-transporting plus-end-directed motors. We expressed each of these kinesins with a carboxy-terminal BioID-3XFLAG tag in 293T cells. Immunoprecipitation of each tagged kinesin, followed by immunoblots for endogenous Hook3, revealed that endogenous Hook3 co-precipitates with KIF1C, but not KIF1A, KIF1B, KIF5A, KIF5B, or KIF5C (Fig. B.2G). We conclude that endogenous Hook3 and KIF1C interact in a specific manner.

KIF1C is a processive plus-end-directed motor, whose motility is not activated by Hook3

To further explore the interaction between KIF1C and Hook3, we purified full-length KIF1C tagged with SNAP and 3XFLAG tags at its carboxy-terminus and full-length Hook3 tagged with a HaloTag at its amino-terminus and 3XFLAG tag at its carboxy-terminus from 293T cells. Each protein migrated as a single band when analyzed by SDS-PAGE (Fig. B.8A). Using total internal reflection fluorescence (TIRF) microscopy with TMR-labeled KIF1C-SNAP-3XFLAG and Alexa-405-labeled microtubules, we visualized the motile properties of KIF1C on microtubules. Single full-length KIF1C molecules moved processively towards the microtubule plus end (Fig. B.3A, Fig. B.8B-D and video 1) with an average velocity of 0.734 ± 0.223 μm/s (Fig. B.3B) and run length of 21.11 μm (Fig. B.3C). We next monitored the interaction of full-length KIF1C-TMR with full-length Hook3 (Fig. B.8A) labeled with Alexa-488 via its amino-terminal HaloTag using near-simultaneous two-color TIRF microscopy. Hook3 alone did not interact with microtubules (Fig. B.3D, left panel). In contrast, in the presence of KIF1C, Hook3 moved robustly towards microtubule plus ends and colocalized with KIF1C (Fig. B.3D, right panels and video 2). The presence of Hook3 did not alter KIF1C's dimerization state as indicated by photo-bleaching analysis (Fig. B.8C, E). KIF1C's

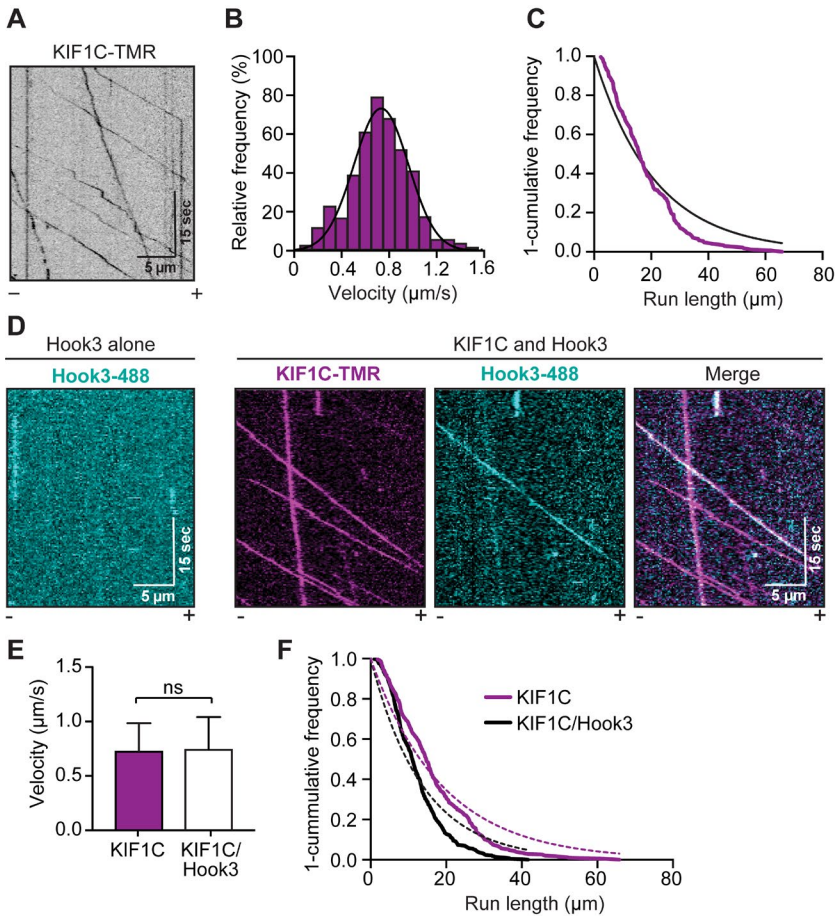

Figure B.3: KIF1C is a highly processive kinesin-3 motor whose motility is not activated by Hook3.
(A) Representative kymograph from single-molecule motility assays with full-length KIF1C tagged with SNAP and 3XFLAG and labeled with TMR via the SNAP-tag. Microtubule polarity is marked with minus (–) and plus (+). **(B)** A histogram of the velocity of single-KIF1C-TMR molecules fit to a Gaussian (black line, 0.734 ± 0.223 μm/s, mean ± SD, R^2 = 0.965). Data from three independent experiments is shown (N = 433). **(C)** Run length analysis of KIF1C-TMR. The 1-cumulative frequency distribution was fit to a one phase exponential decay (black line). The representative mean decay constant is 21.11 μm (R^2 = 0.920, N = 158). **(D)** Representative kymographs from single-molecule motility assays with full-length Hook3 tagged at the amino-terminus with an Alexa-488-labeled HaloTag and carboxy-terminus with 3XFLAG (Hook3-488; left panel). KIF1C-TMR in the presence of Hook3-488 (right panels). Colocalized runs can be seen in the merge in white. Microtubule polarity is marked with minus (–) and plus (+). **(E)** Velocity (mean ± SD) of KIF1C-TMR only runs compared to KIF1C-TMR runs in the presence of Hook3-488 (N = 433 for KIF1C only; N = 716 for KIF1C with Hook3). **(F)** Run length analysis from KIF1C-TMR only runs compared to KIF1C-TMR runs in the presence of Hook3-488. The 1-cumulative frequency distribution was fit to a one phase exponential decay (KIF1C, magenta dotted line; KIF1C with Hook3, black dotted line). The representative mean decay constant for KIF1C is 18.89 μm (r^2 = 0.932, N = 385) and for KIF1C with Hook3 is 13.77 μm (r^2 = 0.901, N = 418). Data was resampled with bootstrapping analysis and statistical significance was calculated using an unpaired t-test with Welch's correction; p= 0.0485. Representative data from three independent experiments is shown.

velocity, landing rates, and pausing frequency were unchanged in the presence of Hook3, while a slight reduction in run length was observed (Figs. B.3E, F and Figs. B.8C-G). In addition, the number of processive, diffusive, or static events for KIF1C was not significantly different in the presence or absence of Hook3 (Fig. B.8H). These data define the single-molecule motile properties of KIF1C and show that Hook3 co-migrates with processive KIF1C molecules and only minimally affects KIF1C's motile properties.

Fourteen amino acids in the tail of KIF1C are required for Hook3 binding

We next sought to identify the regions in both KIF1C and Hook3 responsible for their interaction. We began with KIF1C, generating a series of carboxy-terminal KIF1C truncation constructs, all of which contained a carboxy-terminal 3XFLAG tag (Fig. B.4A). We made constructs lacking the carboxy-terminus including the proline-rich region (KIF1C1-820), lacking the fourth coiled-coil and the proline-rich region (KIF1C1-785), and a deletion mutant that removed a short stretch of charged residues as well as two tryptophans (KIF1CΔ794-807-3XFLAG) (Fig. B.4A). We hypothesized that the amino acid content in this region might form a protein-protein interaction interface in the KIF1C tail sequence that is otherwise predicted to be mainly unstructured or coiled-coil. Overexpression of these constructs in 293T cells followed by FLAG immunoprecipitations revealed that Hook3 binding to KIF1C is lost when the 14 amino acids (794-807) between coiled-coils 3 and 4 are deleted (Fig. B.4B). To confirm the requirement of this region for the interaction between KIF1C and Hook3, we purified KIF1CΔ794-807 with carboxy-terminal SNAP- and 3XFLAG- tags from 293T cells (Fig. B.9A) and labeled it with TMR via its SNAP-tag. Purified KIF1CΔ794-807 showed similar motile properties to wild type KIF1C in a single-molecule assay (Fig. B.9B-D and video 3). However, when KIF1CΔ794-807-TMR was incubated with Hook3-488 and imaged using two-color TIRF microscopy, we observed no colocalized events, further demonstrating the importance of this region for Hook3 binding (Fig. B.4C and video 4). We also made point mutations within this 14 amino acid region, but were

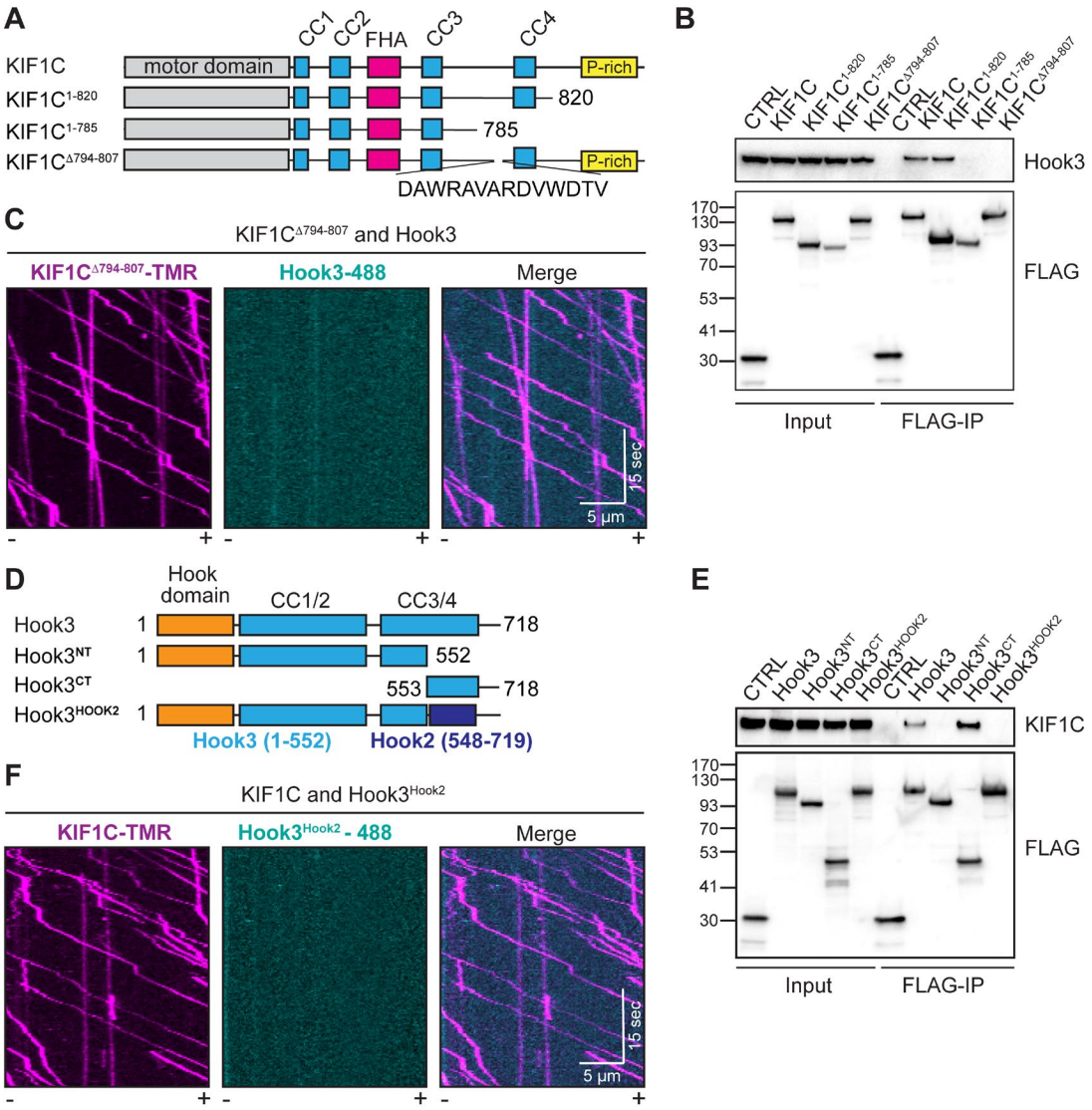

Figure B.4: Fourteen amino acids in the tail of KIF1C mediate its interaction with Hook3. **(A)** Schematic of constructs used to map the region of KIF1C that is responsible for binding to Hook3. **(B)** KIF1C-SNAP-3XFLAG constructs were transiently expressed in 293T cells and immunoprecipitated (FLAG-IP) with FLAG affinity resin. Immunoblots were performed with anti-Hook3 and anti-FLAG antibodies. 3XFLAG-sfGFP provided a control. Protein molecular weight markers are shown in kilodaltons on the anti-FLAG immunoblot. **(C)** Representative kymographs from single-molecule motility assays with purified KIF1C$^{\Delta 794\text{-}807}$-TMR in the presence of Hook3-488. Microtubule polarity is marked with minus (–) and plus (+). **(D)** Schematic of constructs used to map the region of Hook3 that is responsible for binding to KIF1C. Hook3^{NT} (AA 1-552), Hook3^{CT} (AA 553-718), Hook3^{Hook2} (a Hook3 [AA 1-552] and Hook2 [AA 548-719] chimera). **(E)** HaloTag-Hook3-3XFLAG constructs were transiently expressed in 293T cells and immunoprecipitated (FLAG-IP) with FLAG affinity resin. Immunoblots were performed with anti-KIF1C and anti-FLAG antibodies. 3XFLAG-sfGFP provided a control. Protein molecular weight markers are shown in kilodaltons on the anti-FLAG immunoblot. **(F)** Representative kymographs from single-molecule motility assays of KIF1C-TMR in the presence of Hook3^{Hook2}-488. Microtubule polarity is marked with minus (–) and plus (+).

unable to further refine the Hook3 binding site on KIF1C (Fig. B.9E). Taken together, our domain mapping identified a 14 amino acid region in the KIF1C tail that is necessary for Hook3 binding.

Next, we set out to map KIF1C's binding site on Hook3. We previously showed that the carboxy-terminal region of Hook3 (amino acids 553-718) is required for the KIF1C interaction[97]. To attempt to map this binding site more precisely, we generated a series of constructs lacking various regions in the carboxy-terminal tail of Hook3. However, these constructs failed to identify a single linear binding site (Fig. B.9F), perhaps because the KIF1C binding site on Hook3 requires a folded domain. As an alternative approach to generate a Hook3 construct that could no longer bind KIF1C, we designed a chimeric construct in which we replaced amino acids 553-718 of the Halo-Hook3-3XFLAG construct with the homologous region of Hook2 (amino acids 548-719; Fig. B.4D, Fig B.9G), which we showed could not bind KIF1C (Fig. B.2F). We then transfected this chimeric construct (Hook3Hook2), full-length Hook3, Hook3 lacking the carboxy-terminal region (Hook3NT), or Hook3 lacking the amino-terminal region (Hook3CT) into 293T cells and performed FLAG immunoprecipitations. Only full-length Hook3 or Hook3CT co-immunoprecipitated with endogenous KIF1C (Fig. 4E). To verify that this chimeric Hook3Hook2 construct does not directly interact with KIF1C, we purified it from insect cells (Fig. B.9H) and labeled it with Alexa-488 via its HaloTag. Using two-color TIRF microscopy we showed that the Hook3Hook2 chimera does not colocalize with KIF1C-TMR in a single-molecule motility assay (Fig. B.4F and video 5).

Purified full-length Hook3 is a robust dynein activating adaptor

Having shown that Hook3 and KIF1C directly interact, we next tested the dynein activating ability of Hook3 in an in vitro system. Hook3 is a well-established dynein activating adaptor[131]. However, in vitro studies are limited to analyses with a purified truncated version of Hook3 (amino acids 1-552, Hook3NT) or full-length Hook3 present in cell lysates[169], rather than purified full-length protein. In addition, since full-length BICD2, another dynein activating adaptor, exists in an

autoinhibited state[170,171], we aimed to characterize the dynein activation properties of purified full-length Hook3 and establish if full-length Hook3 is autoinhibited.

To do so, we purified human dynein and dynactin complexes separately from stable 293T cell lines expressing the dynein intermediate chain (IC2) or the dynactin subunit p62 tagged with the SNAP-tag or HaloTag, respectively, and a 3XFLAG tag[97]. We labeled IC2 with Alexa-647 and used non-fluorescently labeled dynactin for these experiments. In the absence of Hook3, the dynein/dynactin complex is largely stationary in single-molecule motility assays, exhibiting occasional diffusive events and very rare motile events (Fig. B.10A). In the absence of dynein, Hook3 and dynactin are not motile (Fig. B.10B). However, the combination of dynein, dynactin and purified full-length Hook3 led to robust activation of dynein motility towards microtubule minus ends (Fig. B.5A and video 6). The velocity (0.658 ± 0.287 μm/s, Fig. B.5B) and run length (21.65 μm, Fig. B.5C) were comparable to the values we obtained with truncated Hook3NT (Fig. B.5D-F) and were also consistent with previously reported values for truncated Hook3[97,131,172] or Hook3 present in cell lysates[169]. In addition, the chimeric Hook3Hook2 construct that does not bind KIF1C (Fig. B.4E, F) activated dynein/dynactin to a similar extent as full-length Hook3 (Fig. B.5G-I). Our analysis also showed that dynein/dynactin activated by Hook3 displayed no difference in pausing frequency or the number of processive, diffusive, or static events (Fig. B.10D, E). This suggests that purified full-length Hook3 is a robust dynein activator and is not autoinhibited in its native state.

Hook3 is a scaffold for dynein/dynactin and KIF1C

Thus far, our experiments indicate that full-length Hook3 directly associates with KIF1C and binds to and activates dynein/dynactin complexes. We next sought to determine if Hook3 could bind KIF1C and the dynein/dynactin complex simultaneously. To test this, we performed three-color TIRF microscopy experiments with purified proteins. For these experiments, dynein IC2 was labeled with Alexa-647, Hook3 with Alexa-488, and KIF1C with TMR and dynactin was

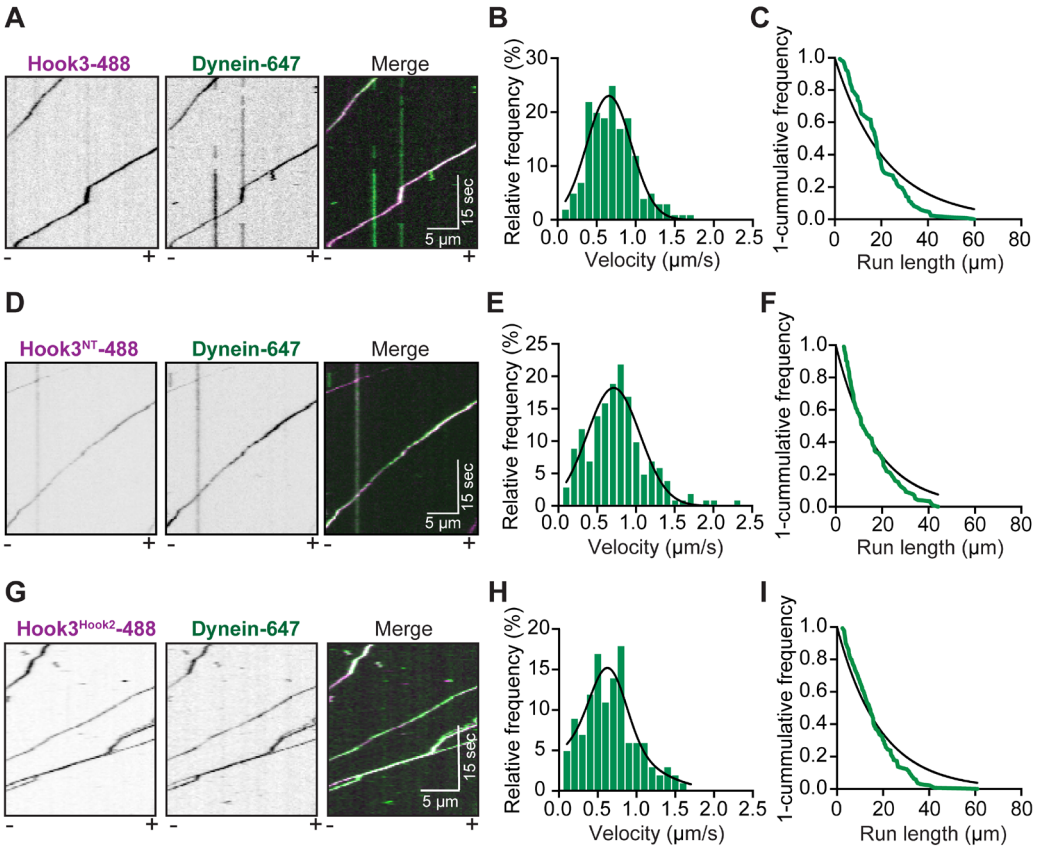

Figure B.5: Purified full-length Hook3 activates dynein motility.
(A) Representative kymographs from single-molecule motility assays with purified dynein-647 (green), unlabeled dynactin and full-length Hook3-488 (magenta). Microtubule polarity is marked with minus (–) and plus (+). **(B)** A histogram of dynein/dynactin velocity in the presence of purified full-length Hook3 fit to a Gaussian (black line, 0.658 ± 0.287 μm/s, mean ± SD, r^2 = 0.910). Representative data from three independent experiments is shown (N = 166). **(C)** Run length analysis of dynein/dynactin in the presence of full-length Hook3. The 1-cumulative frequency distribution (green line) was fit to a one phase exponential decay (black line). The representative mean decay constant is 21.65 μm (r^2 = 0.902, N = 133). **(D)** Representative kymographs from single-molecule motility assays with purified dynein-647 (green), unlabeled dynactin and Hook3$^{1\text{-}552}$-488 (magenta). Microtubule polarity is marked with minus (–) and plus (+). **(E)** A histogram of dynein/dynactin velocity in the presence of Hook3$^{1\text{-}552}$ fit to a Gaussian (black line, 0.710 ± 0.340 μm/s, mean ± SD, r^2 = 0.931). Representative data from two independent experiments is shown (N = 158). **(F)** Run length analysis of dynein/dynactin in the presence of Hook3$^{1\text{-}552}$. The 1-cumulative frequency distribution (green line) was fit to a one phase exponential decay (black line). The representative mean decay constant is 17.08 μm (r^2 = 0.938, N = 118). **(G)** Representative kymographs from single-molecule motility assays with purified dynein-647 (green), unlabeled dynactin and the Hook3^{Hook2}-488 chimera (magenta). Microtubule polarity is marked with minus (–) and plus (+). **(H)** A histogram of velocity of dynein/dynactin in the presence of the Hook3^{HOOK2} chimera fit to a Gaussian (black line, 0.606 ± 0.345 μm/s, mean ± SD, r^2 = 0.813). Representative data from three independent experiments is shown (N = 122). **(I)** Run length analysis of dynein/dynactin in the presence of the Hook3^{Hook2}-488 chimera. The 1-cumulative frequency distribution (green line) was fit to a one phase exponential decay (black line). The representative mean decay constant is 21.25 μm (r^2 = 0.934, N = 139).

unlabeled. This experimental set up allowed us to detect moving events corresponding to 1) KIF1C alone, 2) KIF1C with Hook3, 3) dynein/dynactin with Hook3, and 4) KIF1C with dynein/dynactin and Hook3 (Fig. B.6A). The presence of dynactin is inferred because it is required for dynein motility[131,132]. Complexes that contained all three labeled components (dynein-647, Hook3-488 and KIF1C-TMR) moved in either the minus- (Fig. B.6B, top panel) or plus- (Fig. B.6B, bottom panel) end directions (videos 7 and 8). The presence of these three-color colocalized events implies that Hook3 scaffolds dynein/dynactin and KIF1C to form a complex capable of moving towards the microtubule plus- or minus-end. We did not observe three-color colocalized runs when Hook3 was omitted from the mixture (Fig. B.11A) or when TMR-labeled KIF1CΔ794-807 (Fig. B.11B) or Alexa-488-labeled Hook3Hook2 (Fig. B.11C) were used as opposed to their full-length counterparts.

Next, we quantified the velocity and run length of each detectable species (Fig. B.6C and Fig. B.11D, E). Complexes containing KIF1C and dynein/dynactin scaffolded by Hook3 had slower velocities in the minus-end direction compared to complexes lacking KIF1C (Fig. B.6C). The slowing of the scaffolded complexes in the minus-end direction suggests that KIF1C may engage the microtubule when dynein is the primary driver of motility. Notably, we did not observe any runs (71 of 856 runs contained both motors) in which the moving molecules changed direction.

Because we observed more minus- versus plus-end-directed runs when both KIF1C and dynein were present in the moving complexes (Fig. B.6D) we wondered if the number of runs in either direction was dictated by the amount of each motor available for Hook3 binding. To test this, we varied that relative ratio of KIF1C to dynein in our experiments. These experiments were carried out with labeled dynein (Alexa 647) and Hook3 (Alexa 488), and unlabeled dynactin and KIF1C. We did not label KIF1C so that we could increase its concentration and still observe single-molecule events. Due to the lack of a label on KIF1C, we could detect three separate moving events: 1) plus-end-directed runs that were only Hook3/KIF1C, 2) plus-end-directed runs that

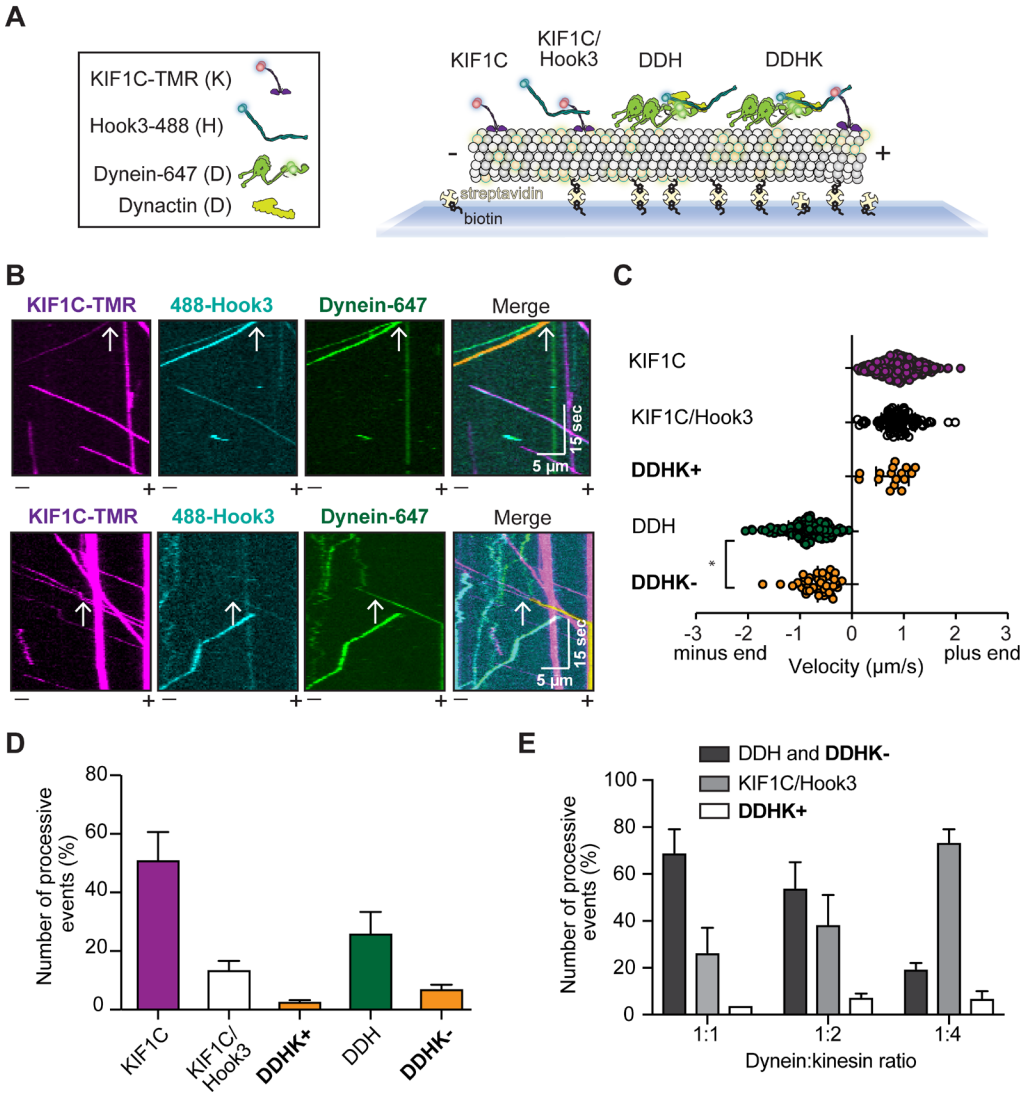

Figure B.6: Hook3 is a scaffold for opposite polarity motors.
(A) Schematic of the experimental set up for three-color single-molecule motility assays. Four different species are detectable using three-color imaging: 1) KIF1C-TMR (KIF1C), 2) KIF1C-TMR with Hook3-488 (KIF1C/Hook3), 3) Dynein-647 with dynactin and Hook3-488 (DDH), and 4) Dynein-647 with dynactin, Hook3-488, and KIF1C-TMR (DDHK). **(B)** Representative kymographs from single-molecule motility assays with purified dynein-647, unlabeled dynactin, KIF1C-TMR and Hook3-488. A three-color colocalized minus-end-directed run (top panel) and three-color colocalized plus-end-directed run (bottom panel) are marked with white arrows on each single-channel image and in the merge. The yellow signal in the merge highlights the colocalized run. Microtubule polarity is marked with minus (–) and plus (+). **(C)** Velocity analysis of the indicated complexes (KIF1C, N = 345; KIF1C/Hook3, N = 136; DDHK+, N = 18; DDH, N =304; DDHK-, N = 53). Statistical significance was calculated with a One-Way Anova with Turkey post-test; *, 0.0121. Combined data from four independent experiments is shown. **(D)** Percent processive events (mean ± SEM) reported in C. Combined data from four independent experiments is shown. **(E)** Percent processive events (mean ± SEM) in the two-color assay with purified dynein-647, unlabeled dynactin, Hook3-488, and unlabeled KIF1C. Increasing concentrations of unlabeled KIF1C are used as indicated by the dynein:KIF1C ratio. Combined data from three independent experiments is shown.

contained both dynein and KIF1C, and 3) minus-end-directed runs that contained two species: dynein/dynactin/Hook3 and dynein/dynactin/Hook3 with KIF1C. As the KIF1C concentration was increased relative to dynein we observed an increase in the percentage of plus-end-directed runs containing both dynein and KIF1C, as well as the number of Hook3/KIF1C runs. We also observed a corresponding decrease in the percentage of minus-end-directed runs (Fig. B.6E). Overall these results imply that the binding of dynein and KIF1C to Hook3 could be competitive. Velocity and run length analysis of these events were comparable to the values we obtained in the three-color experiments (Fig. B.6C and B.11D-I). These data suggest that Hook3 might have different affinities for each motor. In cells, this could result in differences in complex formation or directionality depending on local cellular concentrations of each motor.

KIF1C recruits Hook3 to the cell periphery

Thus far, our data indicate that Hook3 and KIF1C directly interact and that Hook3 can scaffold complexes containing both dynein/dynactin and kinesin. We next explored whether these interactions take place in a cellular context. To test this, we took advantage of our KIF1C 293T knockout cells (Fig. B.2B). We infected KIF1CKO cells (clone #1) with MSCV-driven retroviral KIF1C-tagRFP or KIF1CΔ794-807-tagRFP plasmids to generate stable cells expressing exogenous KIF1C-tagged proteins and used confocal immunofluorescence microscopy to image the cells. Although the KIF1C-tagRFP or KIF1CΔ794-807-tagRFP protein expression levels in these cells were higher than in control 293T cells, this approach allowed us to account for the complete pool of KIF1C in the cell (Fig. B.7A). KIF1C knockout in these cells did not alter Hook3's localization (Fig. B.12A). However, full-length wild type KIF1C recruited endogenous Hook3 to the cell periphery, and this recruitment was abolished in cells expressing KIF1C lacking the Hook3 binding region (Fig. B.7B, C). We also tested if dynactin was recruited to the cell periphery in a KIF1C-dependent manner, but did not observe relocalization of dynactin (Fig. B.12B, C).

Figure B.7: KIF1C recruits Hook3 to the cell periphery.
(A) 293T KIF1C^{KO} cells (KO) were infected with viral particles encoding MSCV-driven KIF1C-tagRFP-3XFLAG or KIF1C$^{\Delta 794\text{-}807}$-tagRFP-3XFLAG plasmids. Immunoblots were performed with the indicated antibodies. Low and high exposures with the KIF1C antibody are shown. ß-actin provided a loading control. 293T cells transfected with CRISPR-Cas9 (CTRL) were used as control cells. **(B)** Confocal microscopy of KIF1C and Hook3 localization in stable 293T cell lines expressing KIF1C-tagRFP-3XFLAG or KIF1C$^{\Delta 794\text{-}807}$-tagRFP-3XFLAG. Cells were grown on glass coverslips, fixed, and stained for endogenous Hook3 (Endo-Hook3). The tagRFP and Hook3 signals are shown in representative maximum intensity projections. The overlap of intensity profiles (arbitrary units, AU) generated from drawing a 15-µm line segment across individual z-sections is shown to the right of the images. **(C)** The mean normalized Hook3 intensity within KIF1C foci for KIF1C-tagRFP-3XFLAG (N = 25) or KIF1C$^{\Delta 794\text{-}807}$-tagRFP-3XFLAG (N = 24). Foci were determined by thresholding the KIF1C image and masks of these foci were used to measure the Hook3 intensity in the corresponding regions in maximum projection images. Box plots represent the maximum and minimum values. Statistical significance was calculated with an unpaired t-test. ****, $p<0.0001$. Representative data from three independent experiments is shown. **(D)** Confocal microscopy of KIF1C and Hook3 in U2OS cells. Cells were grown on glass coverslips, transiently co-transfected with the indicated sfGFP-tagged Hook3 (full-length Hook3, Hook3^{NT} [AA 1-552], Hook3^{CT} [AA 553-718]) or control sfGFP constructs, and KIF1C-V5. 24 hours after transfections cells were fixed and stained with V5 specific antibody. The V5 and sfGFP signals are shown in representative maximum intensity projections. The overlap of intensity profiles (arbitrary units, AU) generated from drawing a 15-µm line segment across an individual z-section is shown to the right of the images. **(E)** The mean normalized Hook3 intensity within KIF1C foci for cells transfected with different Hook3 constructs (CTRL, N = 27; Hook3, N = 28; Hook3^{NT}, N = 33; Hook3^{CT}, N = 29). Foci were determined by thresholding the KIF1C image and masks of these foci were used to measure the Hook3 intensity in these corresponding regions in maximum projection images. Box plots represent maximum and minimum values. Statistical significance was calculated with One Way Anova with Turkey post-test, ****, $p < 0.0001$. Representative data from three independent experiments is shown.

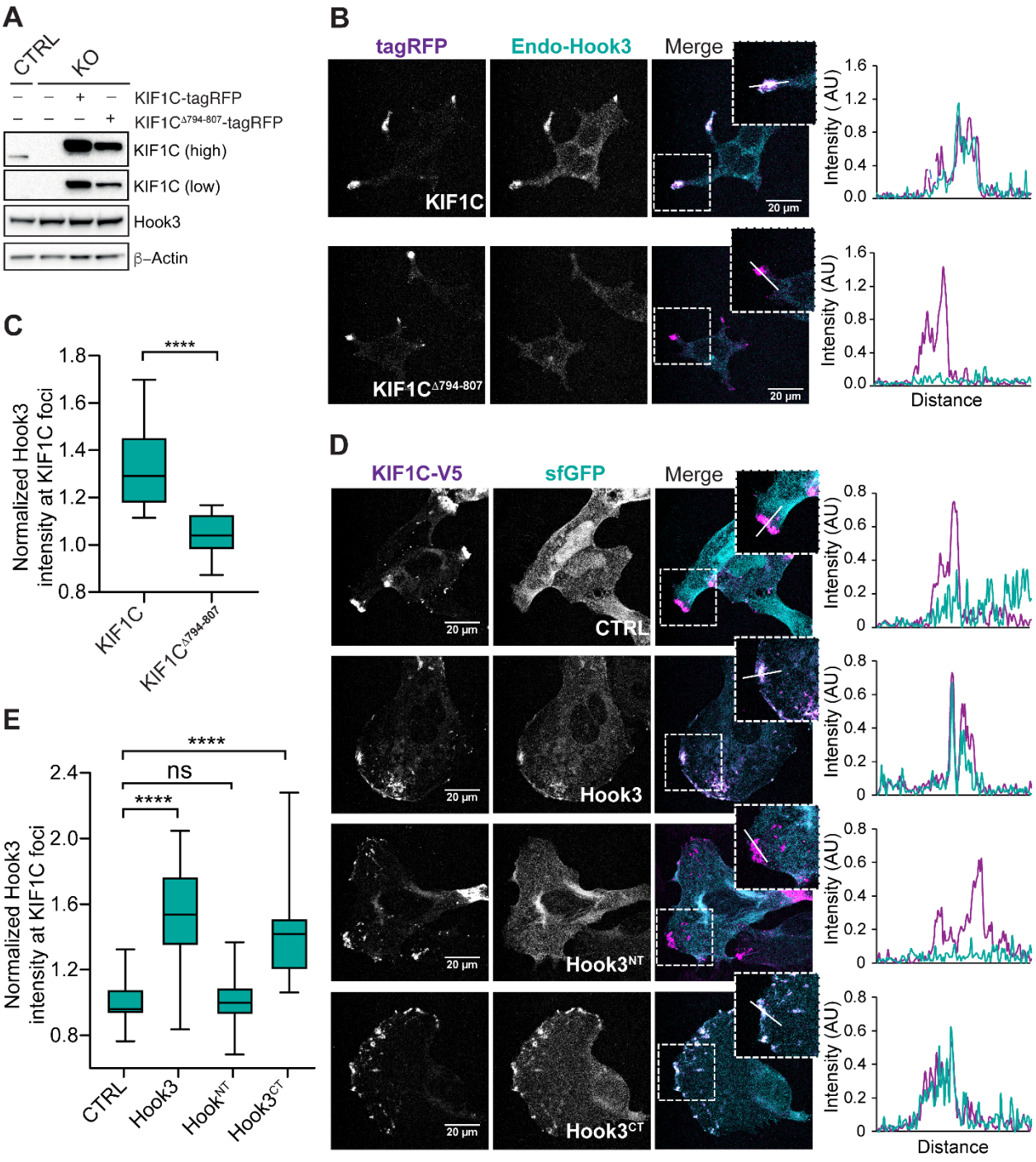
A
CTRL
KO
KIF1C-tagRFP
KIF1C^Δ794-807-tagRFP
KIF1C (high)
KIF1C (low)
Hook3
β–Actin
B
tagRFP
Endo-Hook3
Merge
KIF1C
KIF1C^Δ794-807
20 µm
Intensity (AU)
Intensity (AU)
Distance
C
Normalized Hook3 intensity at KIF1C foci
****
KIF1C
KIF1C^Δ794-807
D
KIF1C-V5
sfGFP
Merge
CTRL
Hook3
Hook3^NT
Hook3^CT
E
ns
CTRL
Hook3
Hook^NT
Hook3^CT

Next, we asked if the KIF1C binding region on Hook3 was required for KIF1C-dependent recruitment of Hook3 to the cell periphery. To do this, we co-transfected human U2OS cells with Hook3 (tagged with sfGFP) and KIF1C (tagged with V5) plasmids and visualized their localization using confocal immunofluorescence microscopy. sfGFP alone or sfGFP tagged Hook3 constructs, including full-length Hook3, Hook3NT, and Hook3CT where expressed in U2OS cells in the presence or absence of KIF1C. Expression of these constructs alone in U2OS cells lead to mainly cytoplasmic Hook3 localization, similar to endogenous Hook3 distribution in these cells (Fig. B.12D, E). However, when KIF1C was co-expressed with Hook3 or Hook3CT, Hook3 was enriched in KIF1C-V5 foci found at the cell periphery (Fig. B.7D, E). This enrichment was lost when Hook3NT, which lacks the KIF1C binding region, was co-expressed with KIF1C-V5 (Fig. B.7D, E). Together our data show that KIF1C recruits Hook3 to the cell periphery and that this recruitment depends on the binding sites we identified in both KIF1C and Hook3.

B.2.5 Discussion

Here we have shown that the dynein activating adaptor Hook3 directly scaffolds the opposite-polarity motors cytoplasmic dynein-1/dynactin and the kinesin KIF1C. In doing so, we have reported the single-molecule motile properties of KIF1C in the presence and absence of full-length Hook3. We mapped the Hook3 interacting region on KIF1C to 14 amino acids in its tail. Hook3 and KIF1C also interact in a cellular environment, as KIF1C recruits Hook3 to the cell periphery. Full-length Hook3 does not activate the motile properties of KIF1C, but is required to activate dynein/dynactin motility. Finally, we reconstituted the entire dynein/dynactin/Hook3 and KIF1C complex from pure components and characterized its motile properties. While complexes containing both motors are relatively rare, we show that dynein/dynactin can transport KIF1C and KIF1C can transport dynein.

KIF1C is a highly processive motor whose activity is not activated by Hook3

Under our analysis conditions full-length KIF1C is a highly processive motor with a characteristic run length that is greater than 15 microns. Kinesin-1s are regulated by autoinhibition via interactions between their motor and tail domains[173–175]. Several lines of evidence suggest that dimeric kinesin-3 family members are also autoinhibited[176–178]. The fact that our purified full-length KIF1C alone is a robust processive motor may indicate that it is not autoinhibited. It is also possible that KIF1C as purified from human 293T cells contains post-translational modifications that could relieve autoinhibition. High-throughput proteomics approaches suggest that KIF1C is phosphorylated, as well as mono-methylated, in multiple regions in its tail[179]. However, how phosphorylation or other candidate posttranslational modifications affect KIF1C's motor activity has not been investigated. In our experiments the addition of Hook3 had no effect on KIF1C's velocity, pausing frequency, or landing frequency, and caused a modest decrease in KIF1C's run length. This suggests that Hook3 is not required to activate KIF1C motility, but rather that Hook3 may function to link KIF1C to other proteins or cargos. In addition, our data suggest that KIF1C exists as a dimer in the presence or absence of Hook3. It is likely that KIF1C interacts with a Hook3 homodimer based on previous evidence showing that Hook proteins, as well as other dynein activating adaptors, form dimers alone or when in a complex with dynein/dynactin[172,180,181].

While we were preparing this manuscript for publication another group reported the motile properties of KIF1C on a preprint server[182]. In this study, KIF1C purified from insect cells appeared to be largely inactive as observed by single-molecule motility experiments. The addition of Hook3 or deletion of a region of KIF1C's third predicted coiled-coil domain increased the landing rate of KIF1C. In contrast, we did not observe a difference in landing rate in the presence of Hook3. The differences between our results and this work could be due to the source of the protein, posttranslational state of the protein, purification methods, or motility assay conditions. Further work will be required to differentiate among these possibilities.

Hook3 is a scaffold for bidirectional motility

Our three-color single-molecule experiments show that Hook3, KIF1C, and dynein/dynactin can exist in a complex together. Furthermore, complex formation requires the KIF1C binding site we identified, and the complex does not form when the carboxy-terminus of Hook3 is replaced by the carboxy-terminus of Hook2 (the Hook family member we showed did not bind KIF1C). Our analysis of fully reconstituted dynein/dynactin/Hook3 and KIF1C complexes indicates that KIF1C can transport dynein/dynactin towards microtubule plus ends and that dynein/dynactin can transport KIF1C towards microtubule minus ends. This suggest that opposite polarity motor binding to Hook3 is not mutually exclusive. Simultaneous Hook3 binding to both motors negatively affects dynein's motility. At the concentrations used in our assays it appears that a higher fraction of Hook3 associates with dynein than with KIF1C, which could indicate that Hook3 has a higher affinity for dynein than for KIF1C. Our analysis raises the possibility that dynein and KIF1C may compete for Hook3 binding. We also note that complexes containing both motors are relatively rare, suggesting that interaction of Hook3 with each motor could be regulated in cells. A detailed analysis of various binding affinities and complex stoichiometry will require higher purification yields of all components.

We do not observe any switches in direction, but we do observe that the presence of KIF1C can slow the velocity of dynein/dynactin/Hook3 complexes in the minus-end direction. This is consistent with a model in which KIF1C engages microtubules while being pulled by dynein towards microtubule minus ends, thus slowing dynein's velocity. Similar velocity decreases have been observed with other opposite polarity motor teams[107,155,156]. Our data suggest that if dynein and KIF1C share a common cargo that moves bidirectionally, the activity of each motor type may be regulated to achieve changes in direction. If such factors exist, our reconstituted system is likely missing them as indicated by the lack of directional switching of dynein/dynactin/Hook3/KIF1C complexes and the purity of our components.

What is the physiological function of kinesin and dynein/dynactin complexes scaffolded by Hook3?

Our data do not directly determine the physiological role of dynein/dynactin complexes scaffolded to KIF1C by Hook3, however our experiments and others in the literature suggest several possibilities. All of which will be exciting areas for future research.

First, it is possible that Hook3 scaffolds KIF1C and cytoplasmic dynein for the bidirectional motility of a shared cargo(s). Consistent with this, KIF1C cargo move bidirectionally in human epithelial cells and neurons[136,162]. Multiple cargos for KIF1C have been proposed. KIF1C is implicated in the transport of α5β1-integrins for focal adhesion and podosome formation[162,183,184]. KIF1C has also been shown to bind to Rab6[185] and KIF1C depletion leads to defects in synaptic vesicle transport[132,186]. In contrast, the most likely cargos for Hook3 are endo-lysosomal compartments (Guo et al., 2016). Hook3 is part of the FHF complex, named after its components, Fused-Toes homolog (FTS), Hook-related protein, and FTS and Hook-interacting protein (FHIP)[168,187,188]. FHF is thought to link the dynein/dynactin complex to Rab5-marked early endosomes, which move bidirectionally in both neurons and filamentous fungi[187–190].

Second, the functional role of Hook3 in scaffolding dynein and KIF1C could be to recycle one or both motors. Such recycling of dynein by kinesin has been observed in S. cerevisiae, where dynein is transported to microtubule plus ends by a kinesin and a set of accessory proteins[157]. This process is through direct protein-protein interactions, as it has been reconstituted in vitro[107]. In addition, in Drosophila oocytes, filamentous fungi, and neurons, kinesin-1 family members are required for dynein's plus-end localization[151,153,154]. If and how kinesins are recycled is less clear; one study of mammalian kinesin-1 suggests that diffusion is sufficient for its recycling[191].

Finally, a third possible function of this complex could be to sequester Hook3 from the available pool of dynein/dynactin activating adaptors. Our cellular analysis shows that KIF1C recruits Hook3 to the cell periphery in a manner that depends on the binding sites we identified in

both KIF1C and Hook3. By removing Hook3 from the cellular pool of dynein activators, KIF1C could be acting as a negative regulator of dynein/dynactin/Hook3 cargo motility. Our observation that KIF1C does not recruit dynactin to the cell periphery supports this possibility, at least in 293T cells.

Is scaffolding of dynein/dynactin and kinesin by dynein activating adaptors a general principle?

We have directly demonstrated that the dynein activating adaptor Hook3 scaffolds KIF1C and dynein/dynactin and that these complexes can move either towards the plus- or minus-ends of microtubules. Do other dynein activating adaptors perform similar functions for dynein/dynactin and other kinesins? There are hints in the literature that this may be the case. For example, interactions between KIF1C and both BICD2 and BICDL1 have also been suggested. In the case of BICD2, network analysis of genes mutated in hereditary spastic paraplegias (HSPs), a disease associated with KIF1C mutations[192], identified BICD2 as a possible KIF1C interactor[163]. This interaction was confirmed by co-immunoprecipitation with overexpressed proteins[163]. In the case of BICDL1, it was shown to interact with KIF1C via two-hybrid experiments and endogenous KIF1C co-immunoprecipitated with overexpressed BICDL1[136]. Other proteins that share a similar general domain structure to the bona fide dynein activating adaptors, such as TRAK1, TRAK2, and HAP1 are candidate dynein activating adaptors[92]. Interestingly, TRAK1, TRAK2, and HAP1 have all been shown to interact with kinesin-1 family members and dynein/dynactin subunits[193–196]. Cell biological and in vitro reconstitution experiments will be required to determine if these candidate dynein activating adaptors and other known dynein activating adaptors scaffold dynein/dynactin to kinesin family members for bidirectional motility.

B.2.6 Methods

Molecular cloning

All plasmids used in this study, unless otherwise stated were constructed by PCR and Gibson isothermal assembly. BioID G2 (Kim et al., 2014) was a kind gift of Kyle Roux (Sanford School of Medicine, University of South Dakota). P62 (isoform 1, 460 aa) was amplified from a human RPE1 cell cDNA library (generated in the Reck-Peterson lab). Hook3 (clone ID: 5106726), KIF1A (clone ID: 40037561), KIF1B (clone ID: 319918), KIF5A (clone ID: 40148192), KIF5B (clone ID: 8991995) and KIF5C (clone ID: 516562) cDNAs were obtained from Dharmacon. Hook1 (clone ID: HsCD00044030), Hook2 isoform 2 (clone ID: HsCD00326811) and KIF1C (clone ID: HsCD00336693) cDNAs were from PlasmidID (Harvard Medical School). Hook2 isoform 2 clone was mutagenized in the Reck-Peterson lab to generate Hook2 isoform 1. The Hook3Hook2 chimera construct was generated by replacing Hook3 amino acids 553-718 with Hook2 amino acids 548-719 using Gibson isothermal assembly and cloned into pLIB vector containing an amino-terminal His6-ZZ-TEV-HaloTag for expression in Sf9 cells. The pSpCas9(BB)-2A-Puro (PX459) V2.0 vector was a gift from Feng Zhang (Broad Institute of MIT and Harvard, Cambridge, MA; Addgene plasmid #62988).

Cell lines and transfections

Human 293T and U2OS cells were obtained from ATCC and maintained at 37°C with 5% CO2 in Dulbecco's Modified Eagle Medium (DMEM, Corning) supplemented with 10% fetal bovine serum (FBS, Gibco) and 1% Penicillin Streptomycin (PenStrep, Corning). Sf9 cells were obtained from Thermo Fisher and grown in Sf-900 II SFM media (Thermo Fisher). All cells were routinely tested for mycoplasma contamination and were not authenticated after purchase.

CRISPR/Cas9-mediated genome editing

Gene editing for creation of KIF1C cells was performed as described previously (Ran et al., 2013). Briefly, in vitro transcribed 20-nucleotide Alt-R crRNA (Hs.Cas9.KIF1C.1.AD) along with Alt-R CRISPR/Cas9 tracrRNA were purchased from Integrated DNA technologies (IDT). The KIF1C exon 3 crRNA sequence was 5'- TCTCACTAACGCGAGAGAAG -3'. To prepare the Alt-R crRNA and Alt-R tracrRNA duplex, reconstituted oligos (100 µM) were mixed at equimolar concentrations in a sterile PCR water and annealed at 95°C for 5 mins, following slow cooling to room temperature. To generate knockout cells, 200 ng of pX459 vector and KIF1C crRNA-tracrRNA duplex (10 nM) were diluted in OptiMEM (Gibco) and combined with 1µg/µL polyethylenimine (PEI; Polysciences Inc.) in a 4:1 ratio of PEI:DNA for transfection into 293T cells. 48 hours post-transfection, the cells were pulsed with 1µg/mL puromycin for 24 hours to allow selection of pX459-transfected cells. Following puromycin selection and recovery in DMEM without puromycin, single cell clones were plated in 96-well format by limiting dilution and cultured to allow single colonies to grow out. Clones were expanded to 12-well plates, and samples of resulting clones were screened via immunoblotting with two independent gene-specific antibodies (KIF1C, rabbit polyclonal Novus cat. No. NBP1-85978, immunogen from AA 996-1096, and rabbit polyclonal, Thermo Fisher cat. No. PA5-27657 immunogen from AA 452-758). A SURVEYOR mutation detection kit (IDT, #706020) was used to detect KIF1C edited clones.

Stable cell lines with near-endogenous protein expression generation

KIF1CKO clones were reconstituted with near-endogenous KIF1C-BioID-3XFLAG, KIF1C tagRFP-3XFLAG or KIF1C∆794-807-tagRFP-3XFLAG respectively, using a retroviral infection/MSCV-driven expression system as described previously (Sowa et al., 2009). Briefly, plasmid DNA (retroviral pMSCV with KIF1C-3XFLAG-BioID, BioID-3XFLAG, KIF1C tagRFP-3XFLAG, and KIF1C∆794-807-tagRFP-3XFLAG genes inserted) along with viral helper constructs (retroviral MSCV-vsvg, MSCV-gag/pol) were diluted in OptiMEM (Gibco) and

combined with 1µg/µL polyethylenimine (PEI; Polysciences Inc.) in a 3:1 ratio of PEI:DNA concentration. The transfection mixture was added to 293T cells, followed by incubation for 12-16 hours. Fresh DMEM was added to the cells, followed by a 24-hour incubation to allow virus production. Viral supernatant was collected, filtered, and added to recipient 293T cells along with 1µg/mL polybrene (Sigma) for infection. Stable cell lines were established by puromycin selection (0.75 µg/mL) for 48-72h. Expression of exogenous proteins was confirmed via immunoblotting with anti-KIF1C and anti-FLAG M2-HRP antibodies.

FLP/FRT stable cell line generation

Dynein (IC2-SNAPf-3XFLAG), dynactin (p62-Halo-3XFLAG), kinesin (KIF1A, KIF1B, KIF1C, KIF5A, KIF5B, and KIF5C) carboxy-terminal BIoID-3XFLAG, and BioID-3XFLAG stable cell lines were created with the FLP/FRT system and T-Rex 293T cells (Invitrogen). These lines were generated as previously described[156]. Briefly, one day before transfection cells we plated onto 10 cm dishes. Cells were transfected with 30 µL of Lipofectamine 2000 and a combination of the appropriate pcDNA5/FRT/GOI construct and Flipase expressing pOG44 plasmid (5 µg of total DNA: 9 parts pOG44 + 1 part pcDNA5/FRT/GOI). Following a 24 hour recovery, cells were grown in DMEM containing 10% FBS, 1% PenStrep, and 50 µg/mL Hygromycin B. Colonies were isolated, expanded, and screened for expression of the fusion proteins by immunoblotting with an anti-FLAG M2-HRP antibody.

Transient transfections

For small-scale immunoprecipitations from transiently transfected 293T cells, 1.5 x 106 cells were plated onto 10 cm dish one day before transfection. Transfections were performed with PEI and 2 µg of transfection grade DNA (Purelink midi prep kit, Invitrogen) per dish, with the exception of Halo-Hook3NT-3xFLAG, where 1 µg of DNA was used due to high protein expression if higher amounts of DNA were used. After 24 hours the media was exchanged to fresh DMEM

containing 10% FBS and 1% PenStrep. Cells were then grown for an additional 24 hours before lysate preparation. For large scale protein purifications, 293T cells were plated onto 30 x 15 cm dishes and grown to ~50% confluence. Cells were transiently transfected with PEI and 7.5 µg DNA per plate. The PEI /DNA mixture was added to plates containing fresh DMEM + 10% FBS (no antibiotics) and incubated overnight. The following day the cells were split 1:3 into 90 x 15 cm plates and incubated an additional 24 hours. Cells were collected by pipetting with ice cold 1X phosphate-buffered saline (PBS, pH 7.4), centrifuged, and washed twice with 1X PBS. The cells were flash frozen in liquid nitrogen prior to lysis.

For immunofluorescence, 0.01-0.03 x 106 cells were plated onto fibronectin (0.001%, Sigma) coated glass coverslips in 24-well plates and grown for 24 hours. Next day transfections were performed with Lipofectamine 2000 and 0.5 µg DNA per 24-well. The Lipofectamine/DNA mixture was added to wells containing fresh DMEM + 10% FBS (no antibiotics) and incubated overnight. The following day cells were fixed and stained.

Immunoprecipitations

Immunoprecipitation from transiently transfected cells

Transiently transfected cells were collected by decanting the media and washing the cells off the dish with ice cold 1X PBS. Cells were collected by centrifugation at 1000 x g for 3 minutes, washed again with 1X PBS, and then transferred with 1X PBS to Eppendorf tubes for lysis. After spinning 2000 rpm in a microcentrifuge for 4 min and removing the 1X PBS, cells were flash frozen for storage or immediately lysed in 500 µL of dynein lysis buffer (DLB, 30 mM HEPES, pH 7.4; 50 mM KOAc; 2 mM MgOAc; 1 mM EGTA, pH 7.5; 10% glycerol) supplemented with 1 mM DTT, 0.2% Triton X-100, 1X protease inhibitor cocktail (cOmplete Protease Inhibitor Cocktail, Roche) with gentle mixing at 4°C for 20 minutes. Lysates were then centrifuged at maximum speed in a 4°C microcentrifuge for 15 min. For each immunoprecipitation, 420 µL clarified lysate was retrieved and added to 50 µL packed volume of anti-FLAG M2 agarose slurry (Sigma) and

incubated for 2 hours at 4°C. Cells were washed four times with 1 mL of DLB, and elutions were carried out with 50 µL of DLB supplemented with 1 mg/mL 3XFLAG peptide (ApexBio).

Immunoprecipitation of endogenous proteins

Wild type 293T cells were grown to ~75% confluence and collected by pipetting with cold 1X PBS on ice. For each immunoprecipitation a single 15 cm plate was collected, washed, and resuspended in 1 mL of DLB supplemented with 1 mM DTT, 0.2% Triton X-100, 1X protease inhibitor cocktail (cOmplete Protease Inhibitor Cocktail, Roche). Resuspended cells were gently mixed at 4°C for 15 min, and then centrifuged at maximum speed in a 4°C microcentrifuge. The beads were prepared by incubating appropriate antibodies with Dynabeads Protein G (Fisher Scientific). For each immunoprecipitation sample, 100 µL of bead slurry was washed 3X with 500 µL of 1X PBS and then resuspended in 100 µL of 1X PBS. To this mixture, 4 µg of the appropriate antibody was added (Hook3, ProteinTech cat. No. 15457-1-AP, immunogen full-length protein; KIF1C, Bethyl cat. No. A301-070A, immunogen from AA 900-950; Normal Rabbit IgG, Cell Signaling cat. No. 2729) and incubated for 30 min at room temperature. The resin was washed twice with 1X PBS and then once with DLB. After removing the final wash, 1 mL of cell lysate was added to the prepared resin and incubated for 4 hours at 4°C. The beads were then washed 3 times with 1 mL DLB. To elute proteins, the resin was resuspended in 60 µL of 4X sample buffer and heated at 95°C for 5 minutes. Eluted proteins were analyzed by SDS-PAGE followed by immunoblotting.

Immunoblotting and antibodies

Lysates and eluates were run on 4-15% polyacrylamide gels (NuPage, Invitrogen). Protein gels were transferred to PVDF membranes for 1.5 hours at 110 V (constant voltage) at 4°C. The membranes were blocked with PBS + 0.05% Tween-20 (v/v, PBST) + 5% dry milk (w/v) and immunoblotted with the appropriate antibodies. All antibodies were diluted in PBST + 1% milk

(w/v). Primary antibodies were incubated overnight at 4°C, while secondary antibodies were incubated for 1 hour at room temperature. Immunoblots were visualized with Supersignal West Pico Chemiluminescent reagent (Thermo Fisher) or Supersignal West Femto Chemiluminescent reagent (Thermo Fisher) on a VersaDoc imaging system (BioRad). Image intensity histograms were adjusted in Image lab Version 6.0.1 (BioRad) and then imported into Adobe Illustrator to make figures.

Antibodies used for immunoblots were as follows:

anti-FLAG M2-HRP (Sigma cat. No. A8592, 1:5000 dilution),

anti-KIF1C (Novus Biotechnologies cat. No. NBP1-85978, immunogen from AA 996-1096 1:500 dilution),

anti-actin (Thermo Fisher cat. No. MAP-15739, immunogen: β-actin N-terminal peptide, 1:4000 dilution),

anti-Hook3 (ProteinTech cat. No. 15457-1-A, immunogen: full-length protein, 1:1000 dilution),

goat anti-rabbit HRP (Santa Cruz Biotechnology cat. No. sc-2030, 1:4000 dilution) and

goat anti-mouse HRP (Santa Cruz Biotechnology cat. No. sc-2031, 1:4000 dilution).

Immunofluorescence, confocal microscopy and image analysis

Fixation and staining

Cells of each condition were grown on fibronectin coated glass coverslips, transfected if indicated, and fixed with 4% paraformaldehyde (PFA, Thermo Fisher) in 1X PBS. Cells were washed with PBS then permeabilized and blocked with 5% normal goat serum (Cell Signaling Technology) in PBS containing 0.5% Triton X-100 (Sigma). Cells were immunostained overnight at 4°C with indicated antibodies diluted in PBS with 1% bovine serum albumin (BSA, Sigma) and 0.1% Triton X-100. The following day cells were washed with PBS and stained with appropriate secondary antibodies and Alexa Fluor 647- or 488-conjugated phalloidin (Invitrogen). Cells were

then washed with PBS and coverslips were mounted on glass slides with CitiFluor AF1 mounting media (TedPella).

Antibodies used for immunofluorescence were as follows:

anti-Hook3 (Thermos Fisher, cat. No. PA5-55172, immunogen full-length protein, 1:200 dilution), anti-dynactin (p150, BD Bioscience cat. No. 610473, immunogen from AA 3-202, 1:200 dilution), anti-V5 (Sigma, cat. No. V8137, 1:1000 dilution),

goat anti-rabbit IgG (H+L) Alexa Fluor-568 (Thermo Fisher cat. No. A11036, 1:500 dilution), goat anti-rabbit IgG (H+L) Alexa Fluor-488 (Thermo Fisher cat. No. A11008, 1:500 dilution) and goat anti-mouse IgG (H+L) Alexa Fluor-647 (Thermo Fisher cat. No. A28181, 1:500 dilution).

Confocal microscopy

Cells were imaged using a Nikon A1R HD confocal microscope with a four-line (405nm, 488nm, 561nm, and 640nm) LUN-V laser engine and DU4 detector using bandpass and longpass filters for each channel (450/50, 525/50, 595/50 and 700/75), mounted on a Nikon Ti2 using an Apo 100x 1.49 NA objective. Images stacks were acquired in resonant mode with bidirectional scanning and 2x or 4x line averaging. The lasers used were 405nm, 488nm, 561nm, and 640nm. To avoid cross-talk between channels, Z-stacks were acquired of the AlexaFluor 568 or tagRFP channel first, and the sfGFP or AlexaFluor488 and AlexaFluor 647 channels were acquired subsequently. Illumination and image acquisition was controlled by NIS Elements Advanced Research software (Nikon Instruments Inc.).

Quantification of co-localization between KIF1C, Hook3 and dynactin

The co-localization with KIF1C was measured with a multi-step automated script assembled with the GA3 module within NIS Elements (Nikon Instruments Inc.). In the first step, an intensity and size threshold using the phalloidin or sfGFP channel was used to map the area of the intracellular region. The intracellular region was defined as all cells within the image

containing KIF1C signal. Then KIF1C positive foci were identified by applying a second threshold in the red channel based on fluorescence intensity and size. Binary masks of the KIF1C positive foci that were within the intracellular masks were selected and the intensity of Hook3 or dynactin staining within the KIF1C foci and intracellular binaries were measured. The average intensity of Hook3 or dynactin under the KIF1C mask was then divided by the average intensity of Hook3 or dynactin under the intracellular mask. This normalized fluorescence intensity of Hook3 or dynactin contained within the foci was then plotted for each condition. For each condition at least 30 cells were analysed per experimnt. Data visualization and statistical analysis was performed using GraphPad Prism (8.0d; GraphPad Software). Statistical analysis was performed with unpaired t-test and one-way Anova with Turkey post-test. Maximum projection images of confocal z-stacks and plot profiles of 15 µm lines drawn through individual z-sections were generated in ImageJ (2.0) and imported into Adobe Illustrator (Ver. 21.0.1) to make figures. Brightness and contrast of all representative images were adjusted in Image J.

BioID sample preparation and mass spectrometry

Cell growth and streptavidin purification

Growth of cells and sample preparation for BioID experiments were performed as previously described with slight modifications[97]. Briefly, BioID-3XFLAG or KIF1C-BioID-3XFLAG cells were plated at ~20% confluence in 15 cm dishes as four replicates, with each replicate consisting of 8 x 15 cm plates. After 24 hours, biotin was added to the media to a final concentration of 50 µM, and the cells were allowed to grow for another 16 hours. After decanting the media, cells were dislodged from each plate by pipetting with ice-cold 1X PBS. Cells were centrifuged at 1000 x g for 2 min following two washes with ice cold 1X PBS and the cell pellets were resuspended and lysed in 16 mL RIPA buffer (50 mM Tris-HCl, pH 8.0; 150 mM NaCl; 1% (v/v) NP-40, 0.5% (w/v) sodium deoxycholate; 0.1% (w/v) SDS; 1 mM DTT; and protease inhibitors (cOmplete Protease Inhibitor Cocktail, Roche) by gentle rocking for 15 mins at 4°C. The

cell lysate was clarified via centrifugation at 66,000 x g for 30 min in a Type 70 Ti rotor (Beckman Coulter; Brea, CA) at 4°C. The clarified lysate was retrieved and combined with pre-washed 0.8 mL streptavidin-conjugated beads (Pierce Streptavidin magnetic beads) and incubated overnight at 4°C with gentle rocking. Bead/lysate mixtures were collected on a magnetic stand into a single 2 mL round-bottom microcentrifuge tube. The beads were then washed 3 times with 2 mL RIPA buffer and once with 1X PBS with immobilization and solution removal performed on a magnetic stand.

On-bead digestion

Samples were prepared for mass spectrometry (MS) as follows. After the final wash the beads were resuspended in 100 µL of 50 mM ammonium bicarbonate (Thermo Fisher) and the proteins on the beads were reduced with 10 mM DTT for 30 min at room temperature and alkylated with 55 mM iodoacetamide (Sigma) for 30 min in the dark. Protein digestion was carried out with sequencing grade modified Trypsin (Promega) at 1/50 protease/protein (wt/wt) at 37°C overnight. After trypsin digestion, the beads were washed twice with 100 µL of 80% acetonitrile (Thermo Fisher) in 1% formic acid (Thermo Fisher) and the supernatants were collected. Samples were dried in Speed-Vac (Thermo Fisher) and desalted and concentrated on Thermo Fisher Pierce C18 Tip.

MS data acquisition

On bead digested samples were analyzed on an Orbitrap Fusion mass spectrometer (Thermo Fisher) coupled to an Easy-nLC 1200 system (Thermo Fisher) through a nanoelectrospray ion source. Peptides were separated on a self-made C18 analytical column (100 µm internal diameter, x 20 cm length) packed with 2.7 µm Cortecs particles. After equilibration with 3 µL 5% acetonitrile and 0.1% formic acid mixture, the peptides were separated by a 120 min linear gradient from 6% to 42% acetonitrile with 0.1% formic acid at 400nL/min. LC

(Optima™ LC/MS, Fisher Scientific) mobile phase solvents and sample dilutions were all made in 0.1% formic acid diluted in water (Buffer A) and 0.1% formic acid in 80 % acetonitrile (Buffer B). Data acquisition was performed using the instrument supplied Xcalibur™ (version 4.1) software. Survey scans covering the mass range of 350–1800 were performed in the Orbitrap by scanning from m/z 300-1800 with a resolution of 120,000 (at m/z 200), an S-Lens RF Level of 30%, a maximum injection time of 50 milliseconds, and an automatic gain control (AGC) target value of 4e5. For MS2 scan triggering, monoisotopic precursor selection was enabled, charge state filtering was limited to 2–7, an intensity threshold of 2e4 was employed, and dynamic exclusion of previously selected masses was enabled for 45 seconds with a tolerance of 10 ppm. MS2 scans were acquired in the Orbitrap mode with a maximum injection time of 35 ms, quadrupole isolation, an isolation window of 1.6 m/z, HCD collision energy of 30%, and an AGC target value of 5e4.

MS data analysis

MS/MS spectra were extracted from raw data files and converted into .mgf files using a Proteome Discoverer Software (ver. 2.1.0.62). These .mgf files were then independently searched against human database using an in-house Mascot server (Version 2.6, Matrix Science). Mass tolerances were +/- 10 ppm for MS peaks, and +/- 25 ppm for MS/MS fragment ions. Trypsin specificity was used allowing for 1 missed cleavage. Met oxidation, protein N-terminal acetylation, N-terminal biotinylation, lysine biotinylation, and peptide N-terminal pyroglutamic acid formation were allowed as variable modifications while carbamidomethyl of Cys was set as a fixed modification. Scaffold (version 4.8, Proteome Software, Portland, OR, USA) was used to validate MS/MS based peptide and protein identifications. Peptide identifications were accepted if they could be established at greater than 95.0% probability as specified by the Peptide Prophet algorithm. Protein identifications were accepted if they could be established at greater than 99.0% probability and contained at least two identified unique peptides.

To estimate relative protein levels, Normalized Spectral Abundance Factor dNSAFs were calculated for each non- redundant protein, as described (Zhang et al., 2010). Average dNSAFs were calculated for each protein using replicates with non-zero dNSAF values. Enrichment of proteins in streptavidin affinity purifications from KIF1C-BioID-3XFLAG tagged stable cell line relative to a control BioID stable cell line was calculated for all replicates as the ratio of average dNSAF (ratio = avg. dNSAFKIF1C-BioID: avg. dNSAFBioID). The volcano plot (Fig. B.2D) was generated by plotting the log2(fold enrichment) against the –log10(p-value), where the p-value (2-tailed Student's T-test) was computed by comparing the replicate dNSAF values of KIF1C-BioID to the BioID control. Potential KIF1C interactions were included as significant if they were not present in the control samples or were >3-fold enriched in the KIF1C-BioID-3XFLAG dataset and had p-values < 0.05.

Protein purification

KIF1C

Different KIF1C constructs were purified from 293T cells transiently transfected with KIF1C-SNAPf-3XFLAG or KIF1CΔ794-807-SNAPf-3XFLAG. Frozen cell pellets from 45 plates were resuspended in 60 mL of BRB80 lysis buffer (80 mM PIPES, pH 6.8; 1 mM MgCL2; 1 mM EGTA; 10% glycerol; 50 mM KOAc) supplemented with 1 mM DTT, 0.5 mM ATP, 0.2% Triton X-100, 1X protease inhibitor cocktail (cOmplete Protease Inhibitor Cocktail, Roche) and gently mixed at 4°C for 15 min. The lysed cells were then centrifuged at 30k x rpm in a Ti70 rotor (Beckman) at 4°C for 30 min. The clarified lysate was retrieved and added to 0.7 mL packed anti-FLAG M2 agarose resin (Sigma) and incubated with gentle mixing at 4°C for 16 hours. After incubation, the lysate/resin mixture was centrifuged at 1000 rpm for 2 min at 4°C to pellet the resin, the supernatant was decanted, and the resin was transferred to a column at 4°C. The column was washed with 50 mL low salt wash buffer (80 mM PIPES, pH 6.8; 1 mM MgCL2; 1 mM EGTA; 10% glycerol; 50 mM KOAc; 1 mM DTT; 0.02% Triton X-100; 0.5 mM Pefabloc), 100 mL

high salt wash buffer (80 mM PIPES, pH 6.8; 1 mM MgCL2; 1 mM EGTA,;10% glycerol; 250 mM KOAc; 1 mM DTT; 0.02% Triton X-100; 0.5 mM Pefabloc), and finally with 150 mL of low salt wash buffer. After the final wash the resin was resuspended in an equal volume of low salt wash buffer (700 µL), moved to room temperature and 7 µL of SNAP-TMR (Promega) was added and mixed. The mixture was incubated in the dark at room temperature for 10 min. The column was returned to 4°C and washed with 100 mL of low salt wash buffer. The labeling steps were omitted when unlabeled protein was desired. The resin was resuspended in 700 µL of low salt wash buffer containing 2 mg/mL 3X-FLAG peptide (ApexBio) and incubated for 30 min at 4°C. The Purified protein was concentrated using a 100 kDa MWCO centrifugal filter (Amicon Ultra, Millipore). Each purified KIF1C construct was aliquoted and aliquots were snap frozen in liquid N2 and stored at -80°C. Protein purity was determined on a Sypro (Thermo Fisher) stained SDS-PAGE gels. The labeling efficiency of KIF1C-SNAPf-TMR was 86% and KIF1C∆794-807-SNAPf-TMR was 99%.

Full-length Hook3

Full-length wild type Hook3 (Halo-Hook3(1-718)-3XFLAG) was purified from transiently transfected 293T cells. Frozen cells (90 x 15 cm plates) were resuspended in 80 mL of DLB buffer supplemented with 1 mM DTT, 0.5 mM ATP, 0.2% Triton X-100, 1X protease inhibitor cocktail (cOmplete Protease Inhibitor Cocktail, Roche) and gently mixed at 4°C for 15 min. The lysed cells were then centrifuged at 30k x rpm in a Ti70 rotor (Beckman) at 4°C for 30 min. The clarified lysate was retrieved and added to 1.5 mL packed anti-FLAG M2 agarose (Sigma) and incubated with gentle mixing at 4°C for 16 hours. After incubation, the lysate/resin mixture was centrifuged at 1000 rpm for 2 min at 4°C to pellet the resin, the supernatant was decanted, and the resin was transferred to a column at 4°C. The column was washed with 100 mL low salt wash buffer (30 mM HEPES, pH 7.4; 50 mM KOAc; 2 mM MgOAc; 1 mM EGTA, pH 7.5; 10% glycerol; 1 mM DTT; 0.5 mM ATP; 0.5 mM Pefabloc; 0.02% Triton X-100), 100 mL high salt wash buffer (30 mM HEPES, pH 7.4; 250 mM KOAc; 2 mM MgOAc; 1 mM EGTA, pH 7.5; 10% glycerol; 1 mM DTT;

0.5 mM ATP; 0.5 mM Pefabloc; 0.02% Triton X-100), and finally with 100 mL of low salt wash buffer. The resin was then resuspended in an equal volume of low salt wash buffer (1.5 mL) and 20 µL of 1 mM Halo-Alexa488 was added and mixed. The mixture was incubated in the dark at room temperature for 10 min. The column was returned to 4°C and washed with 100 mL of low salt wash buffer. The resin was resuspended in 1000 µL of low salt wash buffer containing 2 mg/mL 3X-FLAG peptide (ApexBio) and incubated for 30 min at 4°C. The mixture was retrieved and centrifuged through a small filter column to remove the resin. The eluate was retrieved and 500 µL was loaded onto a Superose 6 Increase 10/300 GL Column connected to an AKTA FPLC (GE) and run in "GF150" buffer (25 mM HEPES, pH 7.4; 150 mM KCl; 1 mM MgCL2; 1 mM DTT). Peak fractions containing Alexa-488 labeled Halo-Hook3-3X FLAG were pooled, concentrated and buffer exchanged to GF150 + 10% glycerol using a 100 kDa MWCO centrifugal filter (Amicon Ultra, Millipore). Aliquots were snap frozen in liquid N2 and stored at -80°C. Protein purity was checked on a Sypro (Thermo Fisher) stained SDS-PAGE gel. The labeling efficiency was 91%.

Hook3^{Hook2} chimera

Hook3^{Hook2} chimera (ZZ-TEV-Halo-Hook3(1-552)-Hook2(548-719)) was purified from Baculovirus-infected Sf9 insect cells. Cell pellets from 800 mL culture were resuspended in DLB supplemented with 0.5 mM ATP, 0.2% Triton X-100, 300 mM KOAc and 1X protease inhibitor cocktail (cOmplete Protease Inhibitor Cocktail, Roche) and lysed using a Dounce homogenizer (15 strokes with loose plunger and 10 strokes with tight plunger). The lysate was clarified by centrifuging at 183,960 x g for 30 min. The clarified lysate was retrieved and added to 1.5 mL of IgG Sepharose 6 fast Flow affinity resin (GE Healthcare), pre-equilibrated in DLB buffer and incubated with gentle mixing at 4°C for 2 hours. After incubation, the lysate/resin mixture was centrifuged at 1000 rpm for 2 min at 4°C to pellet the resin, the supernatant was decanted, and the resin was transferred to a column at 4°C. The column was washed with 100 mL low salt TEV buffer (10 mM Tris-HCl, pH 8; 2 mM MgOAc; 1 mM EGTA, pH 7.5; 10% glycerol; 1 mM DTT; 250

mM KOAc), 100 mL high salt TEV buffer (10 mM Tris-HCl, pH 8; 2 mM MgOAc; 1 mM EGTA, pH 7.5; 10% glycerol; 1 mM DTT; 500 mM KOAc), and finally with 100 mL of low salt TEV buffer. The resin was then resuspended in an equal volume of low salt TEV buffer supplemented with 0.02% NP40 and TEV protease and incubated ~16 hours following labeling with 20 µL of 1 mM Halo-Alexa488. The mixture was incubated at 4°C in the dark for 2 hours. Following labeling, the mixture was retrieved and centrifuged through a small filter column to remove the resin. The eluate was retrieved and 500 µL was loaded onto a Superose 6 Increase 10/300 GL Column connected to an AKTA FPLC (GE Healthcare) and run in GF150 buffer. Peak fractions containing Alexa-488 labeled Halo-Hook3^{Hook2}-3X FLAG were pooled, concentrated and buffer exchanged to GF150 + 10% glycerol using a 100 kDa MWCO centrifugal filter (Amicon Ultra, Millipore). Aliquots were snap frozen in LN2 and stored at -80°C. Protein purity was checked on a Sypro (Thermo Fisher) stained SDS-PAGE gel. The labeling efficiency was 94%.

Hook3^{NT}

The Hook3^{NT} (Strep-Halo-Hook3(1-552)) construct was transformed into BL21-CodonPlus (DE3)-RIPL cells (Agilent). 2L of cells were grown at 37°C in LB media to a 600 nm optical density of 0.4-0.8 before the temperature was reduced to 18°C and expression was induced with 0.5 mM IPTG. After 16-18 hours, the cells were harvested via centrifugation for 6 min at 4°C at 6,000 rpm in a Beckman-Coulter JLA 8.1000 fixed angle rotor. Pellets were resuspended in 40 mL of DLB supplemented with 0.5 mM Pefabloc SC (Sigma-Aldrich) and 1mg/mL lysozyme and incubated at 4°C for 30 min. Cells were lysed via sonication (Branson Digital Sonifier) and clarified via centrifugation at 66,000 x g for 30 min in a Type 70 Ti rotor (Beckman) at 4°C. Supernatant was loaded onto a 5 mL StrepTrap column (GE Healthcare) and washed with 50-100 mL of lysis buffer. Strep-Halo-Hook3NT was eluted with 25-50 mL of elution buffer (DLB with 3 mM d-Desthiobiotin). Elution was then applied to a size exclusion chromatography Superose 6 Increase 10/300 GL column (GE Healthcare) that had been equilibrated with GF150 buffer. Peak fractions containing

Alexa-488 Strep-Halo-Hook3NT were pooled and concentrated using a 100 kDa MWCO centrifugal filter (Amicon Ultra, Millipore). Aliquots were snap frozen in liquid N2 and stored at -80°C. Protein purity was assayed by SDS-PGAE and Sypro (Thermo Fisher) staining. The labeling efficiency was 75%.

Dynein and dynactin

Dynein (IC2-SNAPf-3XFLAG) and dynactin (p62-Halo-3XFLAG) were purified from stable cell line as previously described (Redwine et al., 2017). Briefly, frozen pellets from 293T cells (80 x 15 cm plates, dynein and 160 x 15 cm plates, dynactin) were resuspended in DLB supplemented with 0.5 mM ATP, 0.2% Triton X-100 and 1X protease inhibitor cocktail (cOmplete Protease Inhibitor Cocktail, Roche) and gently mixed at 4°C for 15 min. The lysed cells were then centrifuged at 30,000 rpm in a Ti70 rotor (Beckman) at 4°C for 30 min. The clarified lysate was retrieved and added to 1.5 mL (dynein) or 3 mL (dynactin) packed anti-FLAG M2 agarose resin (Sigma) and incubated with gentle mixing at 4°C for 16 hours. After incubation, the lysate/resin mixture was centrifuged at 1000 rpm for 2 minutes at 4°C to pellet the resin and the supernatant was decanted. The resin was transferred to a column at 4°C and the column was washed with 100 mL low salt wash buffer (30 mM HEPES, pH 7.4; 50 mM KOAc; 2 mM MgOAc; 1 mM EGTA, pH 7.5; 10% glycerol; 1 mM DTT; 0.5 mM ATP; 0.5 mM Pefabloc; 0.02% Triton X-100), 100 mL high salt wash buffer (30 mM HEPES, pH 7.4; 250 mM KOAc; 2 mM MgOAc; 1 mM EGTA, pH 7.5; 10% glycerol; 1 mM DTT; 0.5 mM ATP; 0.5 mM Pefabloc; 0.02% Triton X-100), and finally with 50 mL of low salt wash buffer. After the final wash the resin was resuspended in an equal volume of low salt wash buffer, moved to room temperature and 15 µL of 1 mM SNAP-Alexa-647 was added and mixed. The mixture was incubated in the dark at room temperature for 10 min. The column was returned to 4°C and washed with 100 mL of low salt wash buffer. The labeling steps were omitted when unlabeled protein was desired. The resin was resuspended in 800 µL of low salt wash buffer containing 2 mg/mL 3X-FLAG peptide (ApexBio) and incubated for 30 min

at 4°C. The mixture was retrieved and centrifuged through a small filter column to remove the resin. The eluate was next loaded onto a Mono Q 5/50 GL 1 mL column on an AKTA FPLC (GE Healthcare). The column was washed with 5 mL of Buffer A (50 mM Tris-HCl, pH 8.0; 2 mM MgOAc; 1 mM EGTA; 1 mM DTT) and then subjected to a 26 mL linear gradient from 35-100% Buffer B mixed with Buffer A (Buffer B = 50 mM Tris-HCl, pH 8.0; 1 M KOAc; 2 mM MgOAc; 1 mM EGTA; 1 mM DTT), followed by 5 mL additional 100% Buffer B. Fractions containing pure dynein (~60-70% Buffer B) or pure dynactin (~75-80% Buffer B) were pooled and buffer exchanged through iterative rounds of dilution and concentration on a 100 kDa MWCO centrifugal filter (Amicon Ultra, Millipore) using GF150 buffer with 10% glycerol. Purity was evaluated on SDS-PAGE gels and protein aliquots were snap frozen in liquid N2 and stored at -80°C. The labeling efficiency of dynein-Alexa647 was 97%.

Microtubule preparation

Microtubules were polymerized from tubulin prepared from bovine brain as previously described (Waterman-Storer, 2001). Purified tubulin was labeled with Alexa Fluor 405 NHS Ester (Thermo Fisher), Alexa Fluor 488 NHS Ester (Thermo Fisher), N-ethylmaleimide (NEM, Thermo Fisher) or biotin ester (biotin-X, Thermo Fisher) by serious of polymerization and depolymerization steps. To make biotinylated Alexa405- or Alexa488- microtubules fluorophore labeled tubulin (10 μM) was mixed with biotin-tubulin (10 μM) and unlabeled tubulin (10 μM). The tubulin mixture was incubated on ice for 10 min following an addition of equal volume of polymerization buffer (2X BRB80 supplemented with 2 mM DTT, 2 mM MgGTP and 20% DMSO) and incubation for 30 min at 37°C. After incubation, equal volume of BRB80 supplemented with 1 mM DTT and 20 μM taxol was added to the mixture and microtubules were incubated for additional 10 min at 37°C. Microtubules were used for up to two weeks after polymerization and diluted 1:150-1:200 prior to single-molecule assays.

Polarity marked microtubules were prepared according to previously described protocol with slight modifications[107]. Brightly-labeled, biotinylated microtubule seeds were polymerized by mixing Alexa405-tubulin (10 μM), biotin-tubulin (10 μM) and unlabeled tubulin (10 μM) with 0.5 mM GMP-CPP (Jena Bioscience) in BRB80 supplemented with 1 mM DTT and incubating for 30 min at 37°C. Following the addition of 10X volume of BRB80, polymerized seeds were pelleted in a benchtop centrifuge (15 min at 16,100 x g) and resuspended in a volume of BRB80 equal to the original polymerization volume. GMP-CPP seeds were then mixed with 1:5 diluted dim mix containing 12 μM 405-tubulin, 15 μM unlabeled tubulin, 10 μM biotin tubulin and 15 μM NEM-tubulin and incubated for 30 min at 37°C. After incubation equal volume of BRB80 supplemented with 1 mM DTT and 20 μM taxol was added to the mixture and microtubules were incubated for additional 30 min at 37°C to generate polarity-marked microtubules. 1:25 diluted polarity marked microtubules were flowed into flow chambers and single molecule-motility analysis were performed as described below.

TIRF microscopy

Imaging was performed with an inverted microscope (Nikon, Ti-E Eclipse) equipped with a 100x 1.49 N.A. oil immersion objective (Nikon, Plano Apo). The xy position of the stage was controlled by ProScan linear motor stage controller (Prior). The microscope was equipped with an MLC400B laser launch (Agilent) equipped with 405 nm (30 mW), 488 nm (90 mW), 561 nm (90 mW), and 640 nm (170 mW) laser lines. The excitation and emission paths were filtered using appropriate single bandpass filter cubes (Chroma). The emitted signals were detected with an electron multiplying CCD camera (Andor Technology, iXon Ultra 888). Illumination and image acquisition was controlled by NIS Elements Advanced Research software (Nikon).

Single-molecule motility assays

Single-molecule motility assays were performed in flow chambers using the TIRF microscopy set up described above. Biotinylated and PEGylated coverslips (Microsurfaces) were used to reduce non-specific binding. Microtubules contained ~10% biotin-tubulin for attachment to streptavidin-coated cover slip and ~10% Alexa Fluor 405 or 488 (Thermo Fisher) tubulin for visualization. Imaging buffer was DLB supplemented with 20 μM taxol, 1 mg/mL casein, 1 mM Mg-ATP, 71.5 mM βME (beta mercaptoethanol) and an oxygen scavenger system, 0.4% glucose, 45 μg/ml glucose catalase (Sigma-Aldrich), and 1.15 mg/ml glucose oxidase (Sigma-Aldrich). Images were recorded every 0.3-0.4 sec for 3 min. Movies showing significant drift were not analyzed.

For two-color motility assays of KIF1C with Hook3, 1.125 nM KIF1C-SNAPf-AlexaTMR was mixed with 2.25 nM Hook3-Alexa488 or 2.25 nM Hook3Hook2-Alexa488. The two-color motility measurements of dynein, dynactin and different Hook3 constructs were all performed with 450 pM dynein-Alexa647, 900 pM unlabeled dynactin and 3.25 pM Hook3 (Hook3NT-Alexa488, Hook3-Alexa488 or Hook3Hook2-Alexa488). The three-color single-molecule motility experiments were performed with 450 pM dynein-Alexa647, 900 pM unlabeled dynactin, 130 nM Hook3 (Hook3-Alexa488 or Hook3Hook2-Alexa488) and 0.45 nM KIF1C (KIF1C-SNAPf-TMR or KIF1CΔ794-807-SNAPf-TMR). Two-color motility measurements with increasing concentrations of KIF1C were performed with 450 pM dynein-Alexa647, 900 pM unlabeled dynactin, 3.25 pM Hook3 and the following concentrations of unlabeled KIF1C: 450 pM, 900 pM or 1.8 nM. Each protein mixture was incubated on ice for 10 min prior to TIRF imaging. The order of protein addition or preincubation of Hook3 with KIF1C before dynein and dynactin addition did not affect complex behavior.

Bleaching analysis

Bleach step analysis was performed in a flow chamber, as described above with biotin-Alexa488-microtubules immobilized to the coverslips. 560 pM KIF1C-TMR in the presence or absence of 1.125 nM Hook3-488 was flowed into the chamber in the presence of DLB supplemented with 1mM AMP-PNP (Sigma), 100 μM Taxol and 0.1 mg/ml casein. Images were acquired every 100 ms for 160 s using 562 nm laser at 50% power. Images were analyzed in Image J with Plot Profile function. Steps were manually counted from individual spot profiles.

TIRF data analysis

The velocity of moving particles was calculated form kymographs generated in ImageJ as described previously[107]. Velocities were only calculated from molecules that moved processively for greater than 5 frames. Non-motile or diffusive events were not considered in velocity calculation. Processive events were defined as events that move unidirectionally and do not exhibit directional changes greater than 600 nm. Diffusive events were defined as events that exhibit at least one bidirectional movement greater than 600 nm in each direction. Single-molecule movements that change apparent behavior (e.g. shift from non-motile to processive) were considered as multi-velocity events and counted as multiple events. For run length analysis the length of each track in a multi-velocity event was combined to calculate total run length. Pausing frequency was calculated by measuring the number of pauses in multi-velocity events and dividing this number by the total run length of the multi-velocity event. Landing rates were calculated by counting the number of processive events that start after the first frame and end before the last frame of each movie and dividing this number by the microtubule length and total movie time.

Data visualization and statistical analyses were performed using GraphPad Prism (8.0d; GraphPad Software), Excel (version 16.20; Microsoft), XLSTAT (2019.1.3.; Addinsoft), and ImageJ (2.0). Brightness and contrast were adjusted in Image J for all videos and kymographs. In addition, images in Fig. B.6B, were manually colored (yellow) in Photoshop (Photoshop CC

version 20) to highlight the three-color colocalized runs. For run length analysis data was plotted as a 1-cumulative probability distribution and fit to a one phase exponential decay function (least squares fit). Statistical analyses for velocities, pausing frequency, and landing rates were performed using unpaired t-test with Welch's correction. Errors for run length analysis of KIF1C and KIF1C/Hook3 were generated using a bootstrapping method (each run length value was resampled 200 times) and statistical significance was analyzed using unpaired t-test with Welch's correction. Statistical comparisons of the plus-end and minus-end moving events was performed using one-way Anova with Turkey post-test. Exact value of N and evaluation of statistical significance are described in the corresponding figures and figure legends. All experiments were analyzed from at least three independent replicates, unless otherwise stated.

Sequence alignment

Protein sequences of different Hook isoforms were obtained from UniProt. Sequence alignments were performed with Clustal Omega web services[197] and annotated using Jalview[198].

B.2.7 Supplementary Data

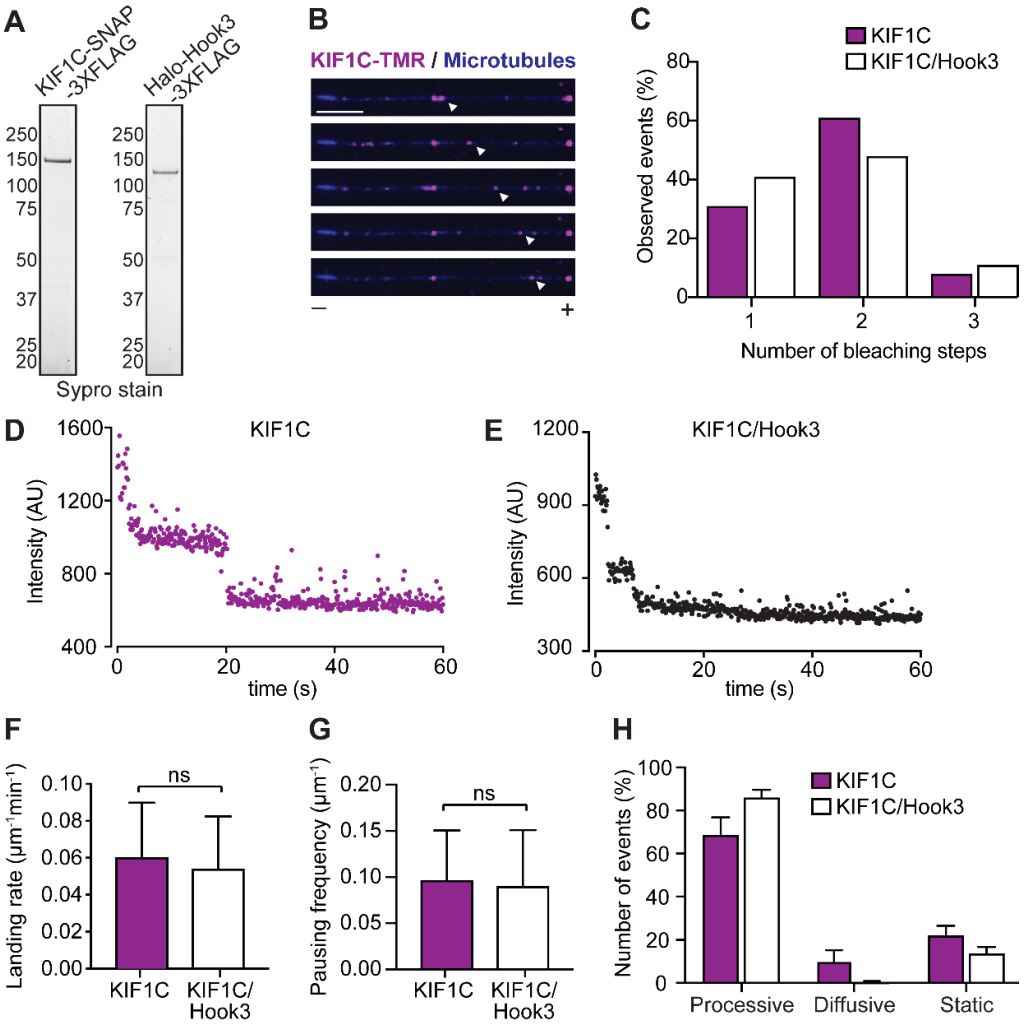

Figure B.8: KIF1C is a processive motor whose motility is not activated by Hook3. **(A)** SDS-PAGE of purified KIF1C-SNAP-3XFLAG and Halo-Hook3-3XFLAG used for motility assays. **(B)** KIF1C-TMR (magenta) motility on polarity marked microtubules. The blue seed made with GMPCPP tubulin marks the microtubule minus end. Scale bar is 2 μm. **(C)** The number of photobleaching steps on microtubules for KIF1C-TMR-only or KIF1C-TMR with Hook3-488 in the presence of AMP-PNP. (KIF1C, N = 100; KIF1C + Hook3, N = 102). Representative data from two independent experiments is shown. **(D)** Example of a two-step photobleaching event for KIF1C. **(E)** Example of a two-step photobleaching event for KIF1C in the presence of Hook3. **(F)** Landing rate (mean ± SD; N = 27 for KIF1C, N = 64 for KIF1C + Hook3) from KIF1C-TMR-only runs compared to KIF1C-TMR runs collected in the presence of Hook3-488. Statistical significance was calculated using an unpaired t-test with Welch's correction; ns, no significance. Representative data from three independent experiments is shown. **(G)** Pausing frequency (mean ± SD, N = 130 for KIF1C, N = 175 for KIF1C + Hook3) from KIF1C-TMR-only runs compared to KIF1C-TMR runs collected in the presence of Hook3-488. Statistical significance was calculated using an unpaired t-test with Welch's correction; ns, no significance. Representative data from three independent experiments is shown. **(H)** Percent processive, diffusive and static events ± SEM in KIF1C-TMR-only runs compared to KIF1C-TMR runs collected in the presence of Hook3-488. Combined data from three independent experiments is shown.

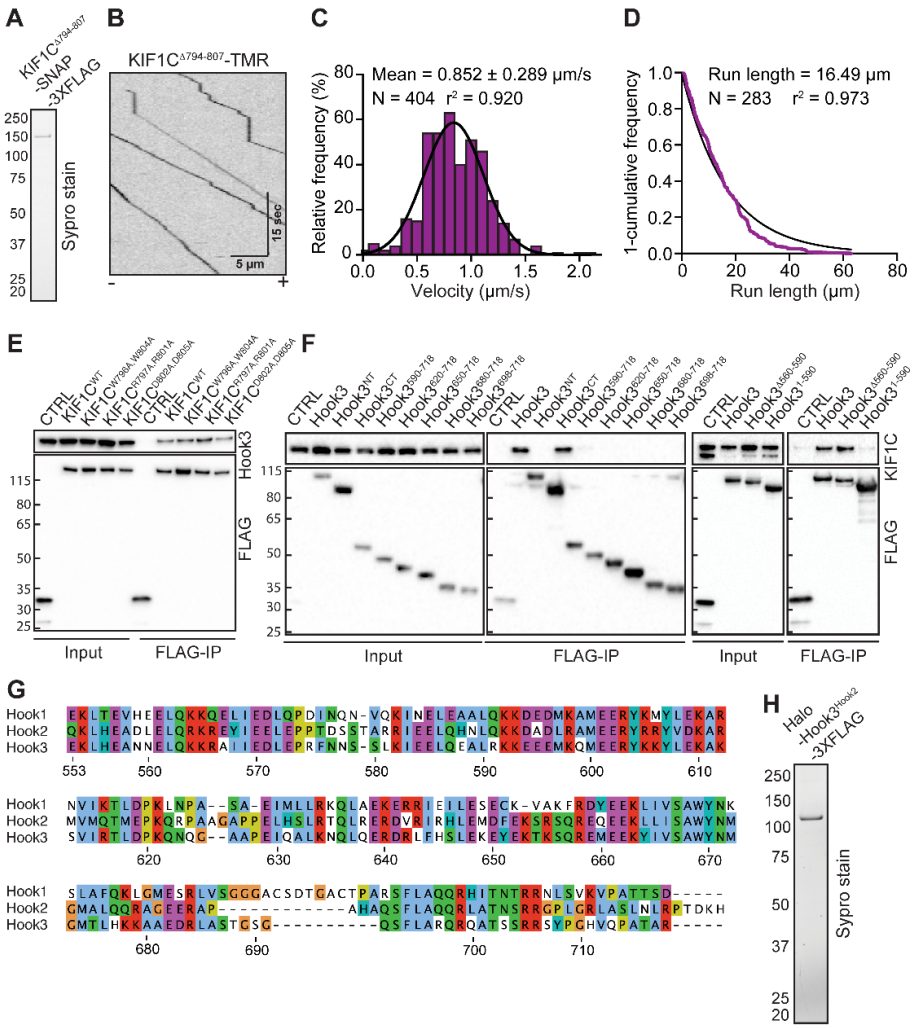

Figure B.9: Mapping of the Hook3 and KIF1C interaction sites.
(A) SDS-PAGE of purified KIF1C$^{\Delta 794\text{-}807}$-SNAP-3XFLAG used for motility assays. **(B)** Representative kymograph from single-molecule motility assays with purified full-length KIF1C$^{\Delta 794\text{-}807}$-SNAP-3XFLAG labeled with TMR. Microtubule polarity is marked with minus (–) and plus (+). **(C)** Single-molecule velocity of KIF1C$^{\Delta 794\text{-}807}$-TMR. A Gaussian fit (black line) to the data from three independent experiments is shown. **(D)** Run length analysis of KIF1C$^{\Delta 794\text{-}807}$-TMR. The 1-cumulative frequency distribution (magenta line) was fit to a one phase exponential decay (black line). Representative mean decay constant (run length) from three independent experiments is reported. **(E)** Indicated KIF1C-3XFLAG constructs were transiently expressed in 293T cells and immunoprecipitated (FLAG-IP) with FLAG affinity resin. Immunoblots were performed with Hook3 and FLAG antibodies. 3XFLAG-sfGFP provided a control (CTRL). Protein molecular weight markers are shown in kilodaltons on the anti-FLAG immunoblot. **(F)** Indicated HaloTag-Hook3-3XFLAG constructs were transiently expressed in 293T cells and immunoprecipitated (FLAG-IP) with FLAG affinity resin. Immunoblots were performed with KIF1C and FLAG antibodies. 3XFLAG-sfGFP provided a control (CTRL). Protein molecular weight markers are shown in kilodaltons on anti-FLAG immunoblots. **(G)** Sequence alignment of the carboxy-terminal regions of the three human hook homologs (Hook3, AA 552-718, Hook2, AA 548-719, and Hook1 AA 556-728) made using Clustal Omega. **(H)** SDS-PAGE of purified Halo tagged Hook3^{Hook2}-3XFLAG used for motility assays.

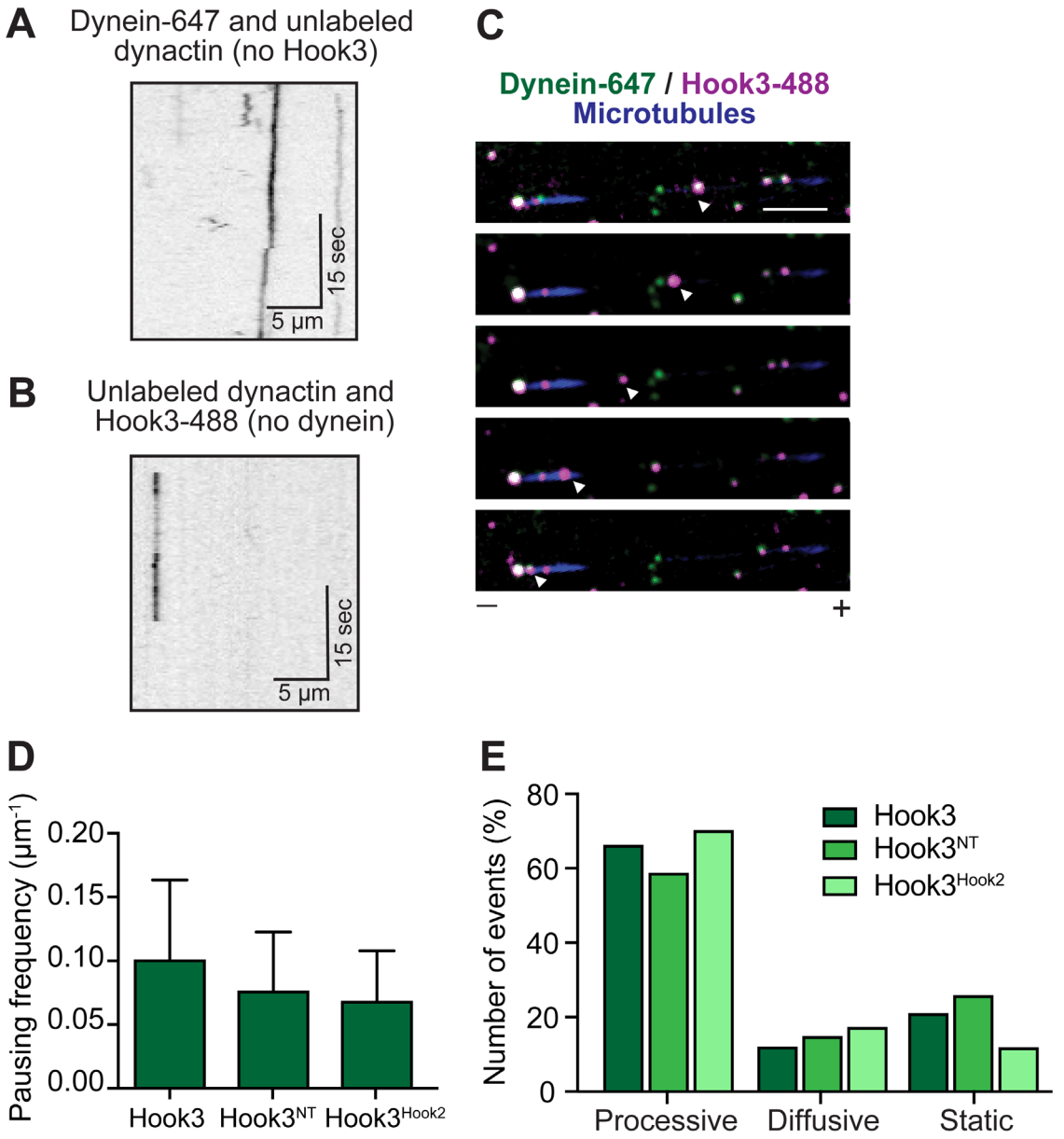

Figure B.10: Purified full-length Hook3, the Hook3 amino terminus, and a Hook3-Hook2 chimera activate dynein motility.

(A) Representative kymograph from single-molecule motility assays with dynein-647 and unlabeled dynactin in the absence of Hook3. **(B)** Representative kymograph from single-molecule motility assays with unlabeled dynactin and Hook3-488 in the absence of dynein. **(C)** Dynein-647 (green) motility in the presence of full-length Hook3-488 (magenta) and unlabeled dynactin on polarity marked microtubules. The blue seed made with GMPCPP tubulin marks the microtubule minus end. Microtubule polarity is marked with minus (–) and plus (+). Scale bar is 2 µm. **(D)** Pausing frequency ± SD of dynein/dynactin complexes in the presence of the indicated activating adaptors (Hook3, N = 72; Hook3^{NT}, N = 24; Hook3^{Hook2}, N = 53). Representative data from at least two independent experiments is shown. **(E)** The number of processive, diffusive, and static events for dynein/dynactin complexes in the presence of the indicated activating adaptors. Representative data from at least two independent experiments is shown.

Figure B.11: Hook3 is a scaffold for opposite polarity motors.
(A) Representative kymographs from single-molecule motility assays with purified dynein-647, unlabeled dynactin and KIF1C-TMR. No Hook3 is present in the sample mixture as represented by the lack of signal in 488-channel. Microtubule polarity is marked with minus (–) and plus (+). **(B)** Representative kymographs from single-molecule motility assays with purified dynein-647, unlabeled dynactin, KIF1C$^{\Delta 794\text{-}807}$-TMR, and Hook3-488. Microtubule polarity is marked with minus (–) and plus (+). **(C)** Representative kymographs from single-molecule motility assays with purified dynein-647, unlabeled dynactin, KIF1C-TMR, and Hook3^{Hook2}-488 chimera. Microtubule polarity is marked with minus (–) and plus (+). **(D)** Run length analysis of all minus-end-directed events reported in Figure B.5D. The 1-cumulative frequency distribution was fit to a one phase exponential decay (not shown). Mean decay constants (run length) are reported. **(E)** Run length analysis of all plus-end-directed events reported in Figure B.5D. The 1-cumulative frequency distribution was fit to a one phase exponential decay (not shown). Representative mean decay constants (run length) are reported. Note that the N value for DDHK+ is too low for an accurate fit. **(F)** Velocity ± SD of the indicated complexes (1:1 ratio: DDH and DDHK-, N =171; KIF1C/Hook3, N = 70; DDHK+, N = 9. 1:2 ratio: DDH and DDHK-, N =161; KIF1C/Hook3, N = 137; DDHK+, N = 22. 1:4 ratio: DDH and DDHK-, N = 59; KIF1C/Hook3, N = 214; DDHK+, N = 22). Combined data from two independent experiments is shown. **(G-I)** Run length analysis of the indicated complexes. The 1-cumulative frequency distribution was fit to a one phase exponential decay (not shown). Representative mean decay constants (run length) are reported. Note that the N value for DDHK+ is too low for an accurate fit.

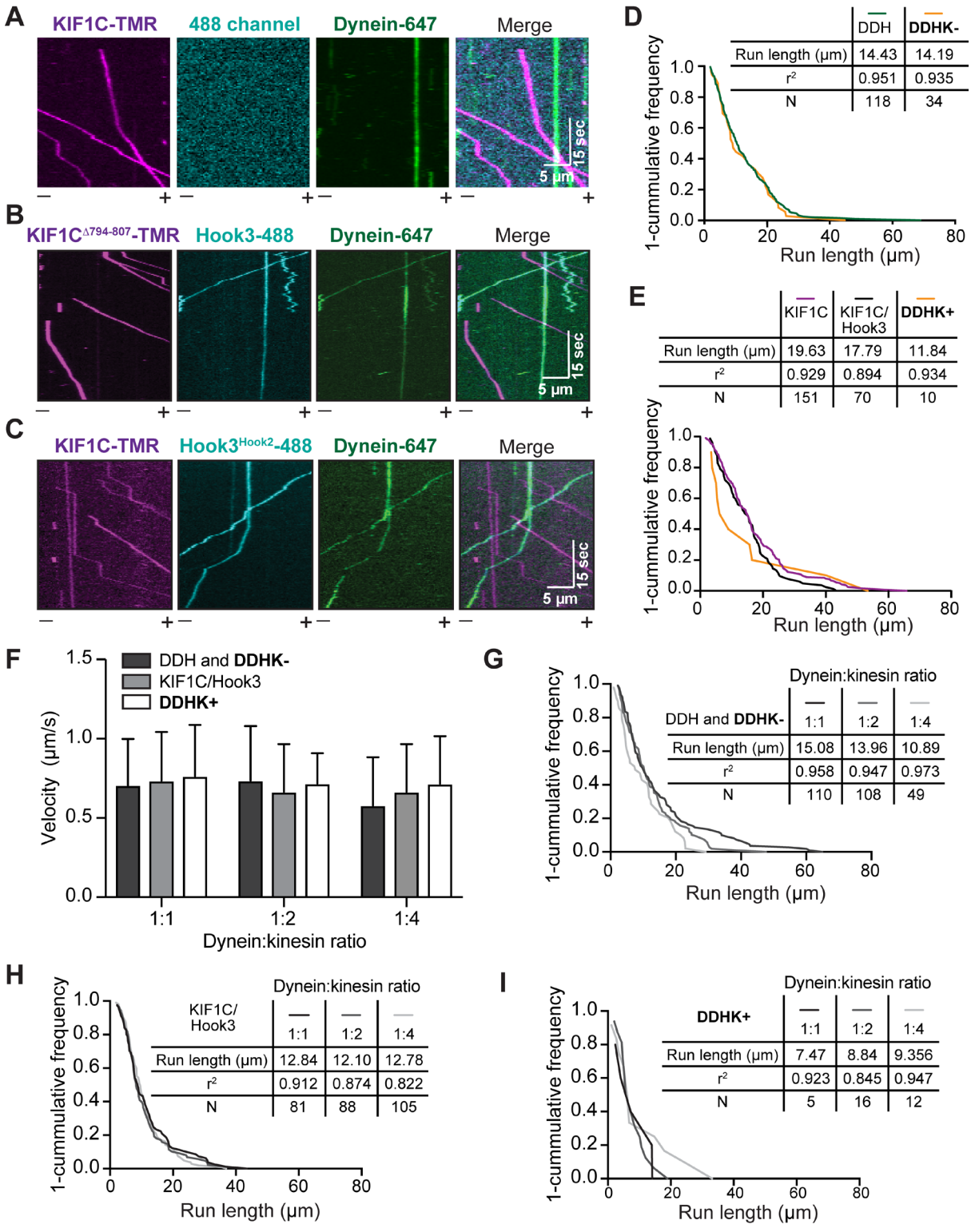
A
KIF1C-TMR
488 channel
Dynein-647
Merge
15 sec
5 µm
B
KIF1C$^{\Delta 794-807}$-TMR
Hook3-488
Dynein-647
Merge
C
KIF1C-TMR
Hook3^{Hook2}-488
Dynein-647
Merge
D
DDH
DDHK-
Run length (µm) 14.43 14.19
r² 0.951 0.935
N 118 34
1-cummulative frequency
Run length (µm)
E
KIF1C
KIF1C/ Hook3
DDHK+
Run length (µm) 19.63 17.79 11.84
r² 0.929 0.894 0.934
N 151 70 10
F
DDH and DDHK-
KIF1C/Hook3
DDHK+
Velocity (µm/s)
1:1
1:2
1:4
Dynein:kinesin ratio
G
Dynein:kinesin ratio
DDH and DDHK- 1:1 1:2 1:4
Run length (µm) 15.08 13.96 10.89
r² 0.958 0.947 0.973
N 110 108 49
H
Dynein:kinesin ratio
KIF1C/ Hook3 1:1 1:2 1:4
Run length (µm) 12.84 12.10 12.78
r² 0.912 0.874 0.822
N 81 88 105
I
Dynein:kinesin ratio
DDHK+ 1:1 1:2 1:4
Run length (µm) 7.47 8.84 9.356
r² 0.923 0.845 0.947
N 5 16 12

Figure B.12: Dynactin localization is unaffected by KIF1C expression.
(A) Confocal microscopy of endogenous Hook3 in control and KIF1C knockout 293T cells. 293T Cas9 control (CTRL) and KIF1C^{KO} cells were grown on glass coverslips, fixed, and stained for endogenous Hook3 (Endo-Hook3). The Hook3 signal is shown in representative maximum intensity projections. **(B)** Confocal microscopy of KIF1C and dynactin localization in 293T KIF1C-tagRFP-3XFLAG and KIF1C$^{\Delta 794\text{-}807}$-tagRFP-3XFLAG stable cell lines. 293T KIF1C tagRFP-3XFLAG or KIF1C$^{\Delta 794\text{-}807}$-tagRFP-3XFLAG cells were grown on glass coverslips, fixed, and stained for endogenous dynactin (Endo-dynactin). The tagRFP and dynactin signals are shown in representative maximum intensity projections. **(C)** The mean normalized dynactin intensity within KIF1C foci for cells stably transfected with different KIF1C constructs (KIF1C-tagRFP-3XFLAG, N = 21 or KIF1C$^{\Delta 794\text{-}807}$-tagRFP-3XFLAG, N = 26). Foci were determined by thresholding the KIF1C image and masks of these foci were used to measure the dynactin intensity in these corresponding regions in maximum projection images. Box plots represent maximum and minimum values. Statistical significance was calculated with unpaired t test; ns, no significance. Representative data from three independent experiments is shown. **(D)** Confocal microscopy of Hook3 in U2OS cells. Cells were grown on glass coverslips and transiently transfected with the indicated sfGFP-tagged Hook3 (full-length Hook3, Hook3^{NT} [AA 1-552], Hook3^{CT} [AA 553-718]) or control sfGFP constructs. 24 hours after the transfections the cells were fixed and stained with a V5 specific antibody. The V5 and sfGFP signals are shown in representative maximum intensity projections. **(E)** Confocal microscopy of endogenous Hook3 in U2OS cells. Cells were grown on glass coverslips, fixed, and stained for endogenous Hook3 (Endo-Hook3). The Hook3 signal is shown in representative maximum intensity projections.

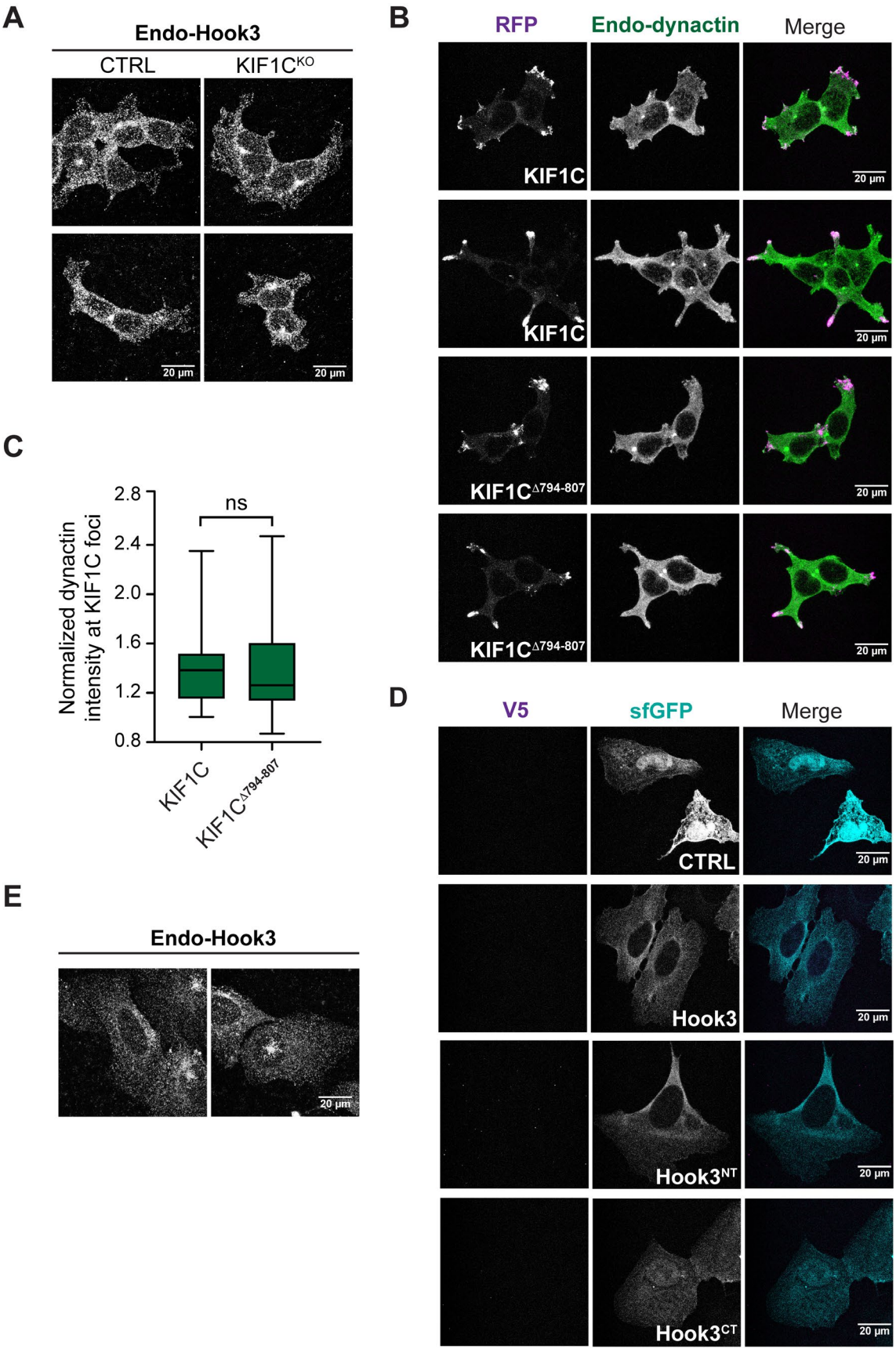
A
Endo-Hook3
CTRL
KIF1C^KO
20 µm
20 µm
B
RFP
Endo-dynactin
Merge
KIF1C
KIF1C
KIF1C^Δ794-807
KIF1C^Δ794-807
20 µm
C
Normalized dynactin intensity at KIF1C foci
2.8
2.4
2.0
1.6
1.2
0.8
ns
KIF1C
KIF1C^Δ794-807
D
V5
sfGFP
Merge
CTRL
Hook3
Hook3^NT
Hook3^CT
20 µm
E
Endo-Hook3
20 µm

Video Legends

Video 1. KIF1C motility on microtubules. KIF1C-TMR (magenta) moving on 405-labeled microtubules (blue). Images were collected using TIRF microscopy. Frames were taken every 400 ms for 180 s. Video frame rate is 24 frames/s. Scale bar is 5 μm.

Video 2. KIF1C motility on microtubules in the presence of Hook3. KIF1C-TMR (magenta) mixed with Hook3-488 (cyan) moving on 405-labeled microtubules (blue). Images were collected using near-simultaneous TIRF microscopy. Frames were taken every 400 ms for 180 s. Video frame rate is 24 frames/s. Scale bar is 5 μm.

Video 3. KIF1C$^{\Delta 794\text{-}807}$ motility on microtubules. KIF1C$^{\Delta 794\text{-}807}$-TMR (magenta) moving on 405-labeled microtubules (blue). Images were collected using TIRF microscopy. Frames were taken every 400 ms for 180 s. Video frame rate is 24 frames/s. Scale bar is 5 μm.

Video 4. KIF1C$^{\Delta 794\text{-}807}$ motility on microtubules in the presence of Hook3. KIF1C$^{\Delta 794\text{-}807}$-TMR (magenta) mixed with Hook3-488 (cyan) moving on 405-labeled microtubules (blue). Images were collected using near-simultaneous TIRF microscopy. Frames were taken every 400 ms for 180 s. Video frame rate is 24 frames/s. Scale bar is 5 μm.

Video 5. KIF1C motility on microtubules in the presence of Hook3^{Hook2}. KIF1C-TMR (magenta) mixed with Hook3^{Hook2}-488 (cyan) moving on 405-labeled microtubules (blue). Images were collected using near-simultaneous TIRF microscopy. Frames were taken every 400 ms for 180 s. Video frame rate is 24 frames/s. Scale bar is 5 μm.

Video 6. Motility of dynein, dynactin and Hook3 on microtubules. Dynein-647 (magenta), unlabeled dynactin and Hook3-488 (cyan) movement on 405-labeled microtubules (blue). Images were collected using near-simultaneous TIRF microscopy. Frames were taken every 400 ms for 180 s. Video frame rate is 24 frames/s. Scale bar is 5 μm.

Video 7. Example of motility of dynein, dynactin, Hook3, and KIF1C on microtubules. Dynein-647 (green), unlabeled dynactin, Hook3-488, and KIF1C-TMR (magenta) movement on 405-labeled microtubules (blue). Hook3-488 channel was omitted in the merge image for easier viewing. White arrow follows a run colocalized in dynein, Hook3 and KIF1C channel. Images were collected using near-simultaneous three-color TIRF microscopy. Frames were taken every 400 ms for 180 s. Video frame rate is 24 frames/s. Scale bar is 5 μm.

Video 8. Example of motility of dynein, dynactin, Hook3, and KIF1C on microtubules. Dynein-647 (green), unlabeled dynactin, Hook3-488, and KIF1C-TMR (magenta) movement on 405-labeled microtubules (blue). Hook3-488 channel was omitted in the merge image for easier viewing. White arrow follows a run colocalized in dynein, Hook3 and KIF1C channels. Images were collected using near-simultaneous three-color TIRF microscopy. Frames were taken every 400 ms for 180 s. Video frame rate is 24 frames/s. Scale bar is 5 μm.

B.2.8 Acknowledgements

We thank Jenna Chistensen, Zaw Htet, John Salogiannis, and Andres Leschziner for critically reading the manuscript, members of the Reck-Peterson laboratory for many lively discussions, and Eric Griffis and the Nikon Imaging Center at the University of California, San Diego, where we collected data and received help with image analysis. Samara L. Reck-Peterson is funded by the Howard Hughes Medical Institute and the National Institutes of Health (R01GM121772). Agnieszka A. Kendrick was funded by the National Institutes of Health (F32GM125224) and is currently funded by the American Cancer Society (PF-18-190-01-CCG). J. Wade Harper is funded by the National Institutes of Health (R37NS083524 and RO1NS110395) and a generous gift from Edward “Ned” Goodnow. J. Wade Harper is a consultant and founder of Rheostat Therapeutics and a consultant for X-Chem Inc. The other authors declare no competing financial interests.

Appendix B, in part, is a reprint of the material as it appears in Hook3 is a scaffold for the opposite-polarity microtubule-based motors cytoplasmic dynein-1 and KIF1C. Agnieszka A. Kendrick, Andrea M. Dickey*, William B. Redwine*, Phuoc Tien Tran, Laura Pontano Vaites, Monika Dzieciatkowska, J. Wade Harper, Samara L. Reck-Peterson, Journal of Cell Biology, 2019. The dissertation author was a co-author of this paper. * denotes equal contributions.

REFERENCES

1. Funayama, M., Hasegawa, K., Kowa, H., Saito, M., Tsuji, S. & Obata, F. A new locus for Parkinson's disease (PARK8) maps to chromosome 12p11.2–q13.1. *Annals of Neurology* 51, 296–301 (2002).

2. Zimprich, A., Müller-Myhsok, B., Farrer, M., Leitner, P., Sharma, M., Hulihan, M., Lockhart, P., Strongosky, A., Kachergus, J., Calne, D. B., Stoessl, J., Uitti, R. J., Pfeiffer, R. F., Trenkwalder, C., Homann, N., Ott, E., Wenzel, K., Asmus, F., Hardy, J., Wszolek, Z. & Gasser, T. The PARK8 Locus in Autosomal Dominant Parkinsonism: Confirmation of Linkage and Further Delineation of the Disease-Containing Interval. *Am J Hum Genet* 74, 11–19 (2004).

3. Goedert, M., Spillantini, M. G., Del Tredici, K. & Braak, H. 100 years of Lewy pathology. *Nat Rev Neurol* 9, 13–24 (2013).

4. de Lau, L. M. & Breteler, M. M. Epidemiology of Parkinson's disease. *The Lancet Neurology* 5, 525–535 (2006).

5. Parkinson, J. An essay on the shaking palsy. 1817. *J Neuropsychiatry Clin Neurosci* 14, 223–236; discussion 222 (2002).

6. Berwick, D. C., Heaton, G. R., Azeggagh, S. & Harvey, K. LRRK2 Biology from structure to dysfunction: research progresses, but the themes remain the same. *Mol Neurodegeneration* 14, 49 (2019).

7. Simón-Sánchez, J., Schulte, C., Bras, J. M., Sharma, M., Gibbs, J. R., Berg, D., Paisan-Ruiz, C., Lichtner, P., Scholz, S. W., Hernandez, D. G., Krüger, R., Federoff, M., Klein, C., Goate, A., Perlmutter, J., Bonin, M., Nalls, M. A., Illig, T., Gieger, C., Houlden, H., Steffens, M., Okun, M. S., Racette, B. A., Cookson, M. R., Foote, K. D., Fernandez, H. H., Traynor, B. J., Schreiber, S., Arepalli, S., Zonozi, R., Gwinn, K., van der Brug, M., Lopez, G., Chanock, S. J., Schatzkin, A., Park, Y., Hollenbeck, A., Gao, J., Huang, X., Wood, N. W., Lorenz, D., Deuschl, G., Chen, H., Riess, O., Hardy, J. A., Singleton, A. B. & Gasser, T. Genome-wide association study reveals genetic risk underlying Parkinson's disease. *Nat Genet* 41, 1308–1312 (2009).

8. Satake, W., Nakabayashi, Y., Mizuta, I., Hirota, Y., Ito, C., Kubo, M., Kawaguchi, T., Tsunoda, T., Watanabe, M., Takeda, A., Tomiyama, H., Nakashima, K., Hasegawa, K., Obata, F., Yoshikawa, T., Kawakami, H., Sakoda, S., Yamamoto, M., Hattori, N., Murata, M., Nakamura, Y. & Toda, T. Genome-wide association study identifies common variants at four loci as genetic risk factors for Parkinson's disease. *Nat Genet* 41, 1303–1307 (2009).

9. West, A. B., Moore, D. J., Biskup, S., Bugayenko, A., Smith, W. W., Ross, C. A., Dawson, V. L. & Dawson, T. M. Parkinson's disease-associated mutations in leucine-rich repeat kinase 2 augment kinase activity. *Proc Natl Acad Sci U S A* 102, 16842–16847 (2005).

10. Gloeckner, C. J., Kinkl, N., Schumacher, A., Braun, R. J., O'Neill, E., Meitinger, T., Kolch, W., Prokisch, H. & Ueffing, M. The Parkinson disease causing LRRK2 mutation I2020T is associated with increased kinase activity. *Human Molecular Genetics* 15, 223–232 (2006).

11. Steger, M., Tonelli, F., Ito, G., Davies, P., Trost, M., Vetter, M., Wachter, S., Lorentzen, E., Duddy, G., Wilson, S., Baptista, M. A., Fiske, B. K., Fell, M. J., Morrow, J. A., Reith, A. D.,

Alessi, D. R. & Mann, M. Phosphoproteomics reveals that Parkinson's disease kinase LRRK2 regulates a subset of Rab GTPases. *eLife* 5, e12813 (2016).

12. Sheng, Z., Zhang, S., Bustos, D., Kleinheinz, T., Le Pichon, C. E., Dominguez, S. L., Solanoy, H. O., Drummond, J., Zhang, X., Ding, X., Cai, F., Song, Q., Li, X., Yue, Z., van der Brug, M. P., Burdick, D. J., Gunzner-Toste, J., Chen, H., Liu, X., Estrada, A. A., Sweeney, Z. K., Scearce-Levie, K., Moffat, J. G., Kirkpatrick, D. S. & Zhu, H. Ser1292 autophosphorylation is an indicator of LRRK2 kinase activity and contributes to the cellular effects of PD mutations. *Sci Transl Med* 4, 164ra161 (2012).

13. Di Maio, R., Hoffman, E. K., Rocha, E. M., Keeney, M. T., Sanders, L. H., De Miranda, B. R., Zharikov, A., Van Laar, A., Stepan, A. F., Lanz, T. A., Kofler, J. K., Burton, E. A., Alessi, D. R., Hastings, T. G. & Greenamyre, J. T. LRRK2 activation in idiopathic Parkinson's disease. *Sci Transl Med* 10, eaar5429 (2018).

14. Hui, K. Y., Fernandez-Hernandez, H., Hu, J., Schaffner, A., Pankratz, N., Hsu, N.-Y., Chuang, L.-S., Carmi, S., Villaverde, N., Li, X., Rivas, M., Levine, A. P., Bao, X., Labrias, P. R., Haritunians, T., Ruane, D., Gettler, K., Chen, E., Li, D., Schiff, E. R., Pontikos, N., Barzilai, N., Brant, S. R., Bressman, S., Cheifetz, A. S., Clark, L. N., Daly, M. J., Desnick, R. J., Duerr, R. H., Katz, S., Lencz, T., Myers, R. H., Ostrer, H., Ozelius, L., Payami, H., Peter, Y., Rioux, J. D., Segal, A. W., Scott, W. K., Silverberg, M. S., Vance, J. M., Ubarretxena-Belandia, I., Foroud, T., Atzmon, G., Pe'er, I., Ioannou, Y., McGovern, D. P. B., Yue, Z., Schadt, E. E., Cho, J. H. & Peter, I. Functional variants in the LRRK2 gene confer shared effects on risk for Crohn's disease and Parkinson's disease. *Sci Transl Med* 10, eaai7795 (2018).

15. Kumar, V., Mack, D. R., Marcil, V., Israel, D., Krupoves, A., Costea, I., Lambrette, P., Grimard, G., Dong, J., Seidman, E. G., Amre, D. K. & Levy, E. Genome-wide association study signal at the 12q12 locus for Crohn's disease may represent associations with the MUC19 gene. *Inflamm Bowel Dis* 19, 1254–1259 (2013).

16. Witoelar, A., Jansen, I. E., Wang, Y., Desikan, R. S., Gibbs, J. R., Blauwendraat, C., Thompson, W. K., Hernandez, D. G., Djurovic, S., Schork, A. J., Bettella, F., Ellinghaus, D., Franke, A., Lie, B. A., McEvoy, L. K., Karlsen, T. H., Lesage, S., Morris, H. R., Brice, A., Wood, N. W., Heutink, P., Hardy, J., Singleton, A. B., Dale, A. M., Gasser, T., Andreassen, O. A. & Sharma, M. Genome-wide Pleiotropy Between Parkinson Disease and Autoimmune Diseases. *JAMA Neurol* 74, 780–792 (2017).

17. Saunders-Pullman, R., Barrett, M. J., Stanley, K. M., Luciano, M. S., Shanker, V., Severt, L., Hunt, A., Raymond, D., Ozelius, L. J. & Bressman, S. B. LRRK2 G2019S mutations are associated with an increased cancer risk in Parkinson disease. *Mov Disord* 25, 2536–2541 (2010).

18. Blanca Ramírez, M., Ordóñez, A. J. L., Fdez, E., Madero-Pérez, J., Gonnelli, A., Drouyer, M., Chartier-Harlin, M.-C., Taymans, J.-M., Bubacco, L., Greggio, E. & Hilfiker, S. GTP binding regulates cellular localization of Parkinson's disease-associated LRRK2. *Human Molecular Genetics* 26, 2747–2767 (2017).

19. West, A. B., Moore, D. J., Choi, C., Andrabi, S. A., Li, X., Dikeman, D., Biskup, S., Zhang, Z., Lim, K.-L., Dawson, V. L. & Dawson, T. M. Parkinson's disease-associated mutations in LRRK2 link enhanced GTP-binding and kinase activities to neuronal toxicity. *Hum Mol Genet* 16, 223–232 (2007).

20. Guo, L., Gandhi, P. N., Wang, W., Petersen, R. B., Wilson-Delfosse, A. L. & Chen, S. G. The Parkinson's disease-associated protein, leucine-rich repeat kinase 2 (LRRK2), is an authentic GTPase that stimulates kinase activity. *Exp Cell Res* 313, 3658–3670 (2007).

21. Taymans, J.-M., Vancraenenbroeck, R., Ollikainen, P., Beilina, A., Lobbestael, E., De Maeyer, M., Baekelandt, V. & Cookson, M. R. LRRK2 kinase activity is dependent on LRRK2 GTP binding capacity but independent of LRRK2 GTP binding. *PLoS One* 6, e23207 (2011).

22. Ito, G., Okai, T., Fujino, G., Takeda, K., Ichijo, H., Katada, T. & Iwatsubo, T. GTP binding is essential to the protein kinase activity of LRRK2, a causative gene product for familial Parkinson's disease. *Biochemistry* 46, 1380–1388 (2007).

23. Xiong, Y., Coombes, C. E., Kilaru, A., Li, X., Gitler, A. D., Bowers, W. J., Dawson, V. L., Dawson, T. M. & Moore, D. J. GTPase activity plays a key role in the pathobiology of LRRK2. *PLoS Genet* 6, e1000902 (2010).

24. Greggio, E., Taymans, J.-M., Zhen, E. Y., Ryder, J., Vancraenenbroeck, R., Beilina, A., Sun, P., Deng, J., Jaffe, H., Baekelandt, V., Merchant, K. & Cookson, M. R. The Parkinson's disease kinase LRRK2 autophosphorylates its GTPase domain at multiple sites. *Biochem Biophys Res Commun* 389, 449–454 (2009).

25. Webber, P. J., Smith, A. D., Sen, S., Renfrow, M. B., Mobley, J. A. & West, A. B. Autophosphorylation in the leucine-rich repeat kinase 2 (LRRK2) GTPase domain modifies kinase and GTP-binding activities. *J Mol Biol* 412, 94–110 (2011).

26. Greggio, E., Zambrano, I., Kaganovich, A., Beilina, A., Taymans, J.-M., Daniëls, V., Lewis, P., Jain, S., Ding, J., Syed, A., Thomas, K. J., Baekelandt, V. & Cookson, M. R. The Parkinson Disease-associated Leucine-rich Repeat Kinase 2 (LRRK2) Is a Dimer That Undergoes Intramolecular Autophosphorylation *. *Journal of Biological Chemistry* 283, 16906–16914 (2008).

27. Bae, E.-J. & Lee, S.-J. The LRRK2-RAB axis in regulation of vesicle trafficking and α-synuclein propagation. *Biochim Biophys Acta Mol Basis Dis* 1866, 165632 (2020).

28. Hur, E.-M., Jang, E.-H. & Lee, G. R. J. & B. D. LRRK2 and membrane trafficking: nexus of Parkinson's disease. *BMB Reports* 52, 533–539 (2019).

29. Bonet-Ponce, L. & Cookson, M. R. LRRK2 recruitment, activity, and function in organelles. *FEBS J* (2021). doi:10.1111/febs.16099

30. Eguchi, T., Kuwahara, T., Sakurai, M., Komori, T., Fujimoto, T., Ito, G., Yoshimura, S.-I., Harada, A., Fukuda, M., Koike, M. & Iwatsubo, T. LRRK2 and its substrate Rab GTPases are sequentially targeted onto stressed lysosomes and maintain their homeostasis. *Proc Natl Acad Sci U S A* 115, E9115–E9124 (2018).

31. Bonet-Ponce, L., Beilina, A., Williamson, C. D., Lindberg, E., Kluss, J. H., Saez-Atienzar, S., Landeck, N., Kumaran, R., Mamais, A., Bleck, C. K. E., Li, Y. & Cookson, M. R. LRRK2 mediates tubulation and vesicle sorting from lysosomes. *Sci Adv* 6, eabb2454 (2020).

32. Henry, A. G., Aghamohammadzadeh, S., Samaroo, H., Chen, Y., Mou, K., Needle, E. & Hirst, W. D. Pathogenic LRRK2 mutations, through increased kinase activity, produce enlarged

lysosomes with reduced degradative capacity and increase ATP13A2 expression. *Hum Mol Genet* 24, 6013–6028 (2015).

33. Hockey, L. N., Kilpatrick, B. S., Eden, E. R., Lin-Moshier, Y., Brailoiu, G. C., Brailoiu, E., Futter, C. E., Schapira, A. H., Marchant, J. S. & Patel, S. Dysregulation of lysosomal morphology by pathogenic LRRK2 is corrected by TPC2 inhibition. *J Cell Sci* 128, 232–238 (2015).

34. Pfeffer, S. R. Rab GTPases: master regulators that establish the secretory and endocytic pathways. *Mol Biol Cell* 28, 712–715 (2017).

35. Purlyte, E., Dhekne, H. S., Sarhan, A. R., Gomez, R., Lis, P., Wightman, M., Martinez, T. N., Tonelli, F., Pfeffer, S. R. & Alessi, D. R. Rab29 activation of the Parkinson's disease-associated LRRK2 kinase. *The EMBO Journal* 37, 1–18 (2018).

36. Gomez, R. C., Wawro, P., Lis, P., Alessi, D. R. & Pfeffer, S. R. Membrane association but not identity is required for LRRK2 activation and phosphorylation of Rab GTPases. *J Cell Biol* 218, 4157–4170 (2019).

37. Kett, L. R., Boassa, D., Ho, C. C.-Y., Rideout, H. J., Hu, J., Terada, M., Ellisman, M. & Dauer, W. T. LRRK2 Parkinson disease mutations enhance its microtubule association. *Human Molecular Genetics* 21, 890–899 (2012).

38. Watanabe, R., Buschauer, R., Böhning, J., Audagnotto, M., Lasker, K., Lu, T.-W., Boassa, D., Taylor, S. & Villa, E. The In Situ Structure of Parkinson's Disease-Linked LRRK2. *Cell* 182, 1508-1518.e16 (2020).

39. Deniston, C. K., Salogiannis, J., Mathea, S., Snead, D. M., Lahiri, I., Matyszewski, M., Donosa, O., Watanabe, R., Böhning, J., Shiau, A. K., Knapp, S., Villa, E., Reck-Peterson, S. L. & Leschziner, A. E. Structure of LRRK2 in Parkinson's disease and model for microtubule interaction. *Nature* 588, 344–349 (2020).

40. Leschziner, A. E. & Reck-Peterson, S. L. Structural Biology of LRRK2 and its Interaction with Microtubules. *Movement Disorders* 36, 2494–2504 (2021).

41. Steger, M., Diez, F., Dhekne, H. S., Lis, P., Nirujogi, R. S., Karayel, O., Tonelli, F., Martinez, T. N., Lorentzen, E., Pfeffer, S. R., Alessi, D. R. & Mann, M. Systematic proteomic analysis of LRRK2-mediated Rab GTPase phosphorylation establishes a connection to ciliogenesis. *Elife* 6, e31012 (2017).

42. Dhekne, H. S., Yanatori, I., Gomez, R. C., Tonelli, F., Diez, F., Schüle, B., Steger, M., Alessi, D. R. & Pfeffer, S. R. A pathway for Parkinson's Disease LRRK2 kinase to block primary cilia and Sonic hedgehog signaling in the brain. *eLife* 7, e40202 (2018).

43. Madero-Pérez, J., Fernández, B., Lara Ordóñez, A. J., Fdez, E., Lobbestael, E., Baekelandt, V. & Hilfiker, S. RAB7L1-Mediated Relocalization of LRRK2 to the Golgi Complex Causes Centrosomal Deficits via RAB8A. *Frontiers in Molecular Neuroscience* 11, (2018).

44. Madero-Pérez, J., Fdez, E., Fernández, B., Lara Ordóñez, A. J., Blanca Ramírez, M., Gómez-Suaga, P., Waschbüsch, D., Lobbestael, E., Baekelandt, V., Nairn, A. C., Ruiz-Martínez, J., Aiastui, A., López de Munain, A., Lis, P., Comptdaer, T., Taymans, J.-M., Chartier-

Harlin, M.-C., Beilina, A., Gonnelli, A., Cookson, M. R., Greggio, E. & Hilfiker, S. Parkinson disease-associated mutations in LRRK2 cause centrosomal defects via Rab8a phosphorylation. *Mol Neurodegener* 13, 3 (2018).

45. Davies, P., Hinkle, K. M., Sukar, N. N., Sepulveda, B., Mesias, R., Serrano, G., Alessi, D. R., Beach, T. G., Benson, D. L., White, C. L., Cowell, R. M., Das, S. S., West, A. B. & Melrose, H. L. Comprehensive characterization and optimization of anti-LRRK2 (leucine-rich repeat kinase 2) monoclonal antibodies. *Biochem J* 453, 101–113 (2013).

46. Berger, Z., Smith, K. A. & Lavoie, M. J. Membrane localization of LRRK2 is associated with increased formation of the highly active LRRK2 dimer and changes in its phosphorylation. *Biochemistry* 49, 5511–5523 (2010).

47. Nichols, R. J., Dzamko, N., Morrice, N. A., Campbell, D. G., Deak, M., Ordureau, A., Macartney, T., Tong, Y., Shen, J., Prescott, A. R. & Alessi, D. R. 14-3-3 binding to LRRK2 is disrupted by multiple Parkinson's disease-associated mutations and regulates cytoplasmic localization. *Biochemical Journal* 430, 393–404 (2010).

48. Dzamko, N., Deak, M., Hentati, F., Reith, A. D., Prescott, A. R., Alessi, D. R. & Nichols, R. J. Inhibition of LRRK2 kinase activity leads to dephosphorylation of Ser910/Ser935, disruption of 14-3-3 binding and altered cytoplasmic localization. *Biochemical Journal* 430, 405–413 (2010).

49. Stevers, L. M., de Vries, R. M. J. M., Doveston, R. G., Milroy, L.-G., Brunsveld, L. & Ottmann, C. Structural interface between LRRK2 and 14-3-3 protein. *Biochemical Journal* 474, 1273–1287 (2017).

50. Muda, K., Bertinetti, D., Gesellchen, F., Hermann, J. S., von Zweydorf, F., Geerlof, A., Jacob, A., Ueffing, M., Gloeckner, C. J. & Herberg, F. W. Parkinson-related LRRK2 mutation R1441C/G/H impairs PKA phosphorylation of LRRK2 and disrupts its interaction with 14-3-3. *Proceedings of the National Academy of Sciences* 111, E34–E43 (2014).

51. Schapansky, J., Nardozzi, J. D., Felizia, F. & LaVoie, M. J. Membrane recruitment of endogenous LRRK2 precedes its potent regulation of autophagy. *Human Molecular Genetics* 23, 4201–4214 (2014).

52. Kalogeropulou, A. F., Freemantle, J. B., Lis, P., Vides, E. G., Polinski, N. K. & Alessi, D. R. Endogenous Rab29 does not impact basal or nigericin and monensin stimulated LRRK2 pathway activity. 2020.06.08.139675 (2020). doi:10.1101/2020.06.08.139675

53. Deng, X., Dzamko, N., Prescott, A., Davies, P., Liu, Q., Yang, Q., Lee, J.-D., Patricelli, M. P., Nomanbhoy, T. K., Alessi, D. R. & Gray, N. S. Characterization of a selective inhibitor of the Parkinson's disease kinase LRRK2. *Nature Chemical Biology* 7, 203–205 (2011).

54. Schmidt, S. H., Knape, M. J., Boassa, D., Mumdey, N., Kornev, A. P., Ellisman, M. H., Taylor, S. S. & Herberg, F. W. The dynamic switch mechanism that leads to activation of LRRK2 is embedded in the DFGψ motif in the kinase domain. *PNAS* 116, 14979–14988 (2019).

55. Horgan, C. P. & McCaffrey, M. W. Rab GTPases and microtubule motors. *Biochemical Society Transactions* 39, 1202–1206 (2011).

56. Deng, J., Lewis, P. A., Greggio, E., Sluch, E., Beilina, A. & Cookson, M. R. Structure of the ROC domain from the Parkinson's disease-associated leucine-rich repeat kinase 2 reveals a dimeric GTPase. *Proc Natl Acad Sci U S A* 105, 1499–1504 (2008).

57. Zhang, P., Fan, Y., Ru, H., Wang, L., Magupalli, V. G., Taylor, S. S., Alessi, D. R. & Wu, H. Crystal structure of the WD40 domain dimer of LRRK2. *PNAS* 116, 1579–1584 (2019).

58. Guaitoli, G., Raimondi, F., Gilsbach, B. K., Gómez-Llorente, Y., Deyaert, E., Renzi, F., Li, X., Schaffner, A., Jagtap, P. K. A., Boldt, K., von Zweydorf, F., Gotthardt, K., Lorimer, D. D., Yue, Z., Burgin, A., Janjic, N., Sattler, M., Versées, W., Ueffing, M., Ubarretxena-Belandia, I., Kortholt, A. & Gloeckner, C. J. Structural model of the dimeric Parkinson's protein LRRK2 reveals a compact architecture involving distant interdomain contacts. *Proc Natl Acad Sci U S A* 113, E4357-4366 (2016).

59. Sejwal, K., Chami, M., Rémigy, H., Vancraenenbroeck, R., Sibran, W., Sütterlin, R., Baumgartner, P., McLeod, R., Chartier-Harlin, M.-C., Baekelandt, V., Stahlberg, H. & Taymans, J.-M. Cryo-EM analysis of homodimeric full-length LRRK2 and LRRK1 protein complexes. *Scientific Reports* 7, 8667 (2017).

60. Myasnikov, A., Zhu, H., Hixson, P., Xie, B., Yu, K., Pitre, A., Peng, J. & Sun, J. Structural analysis of the full-length human LRRK2. *Cell* 184, 3519-3527.e10 (2021).

61. Snead, D. M., Matyszewski, M., Dickey, A. M., Lin, Y. X., Leschziner, A. E. & Reck-Peterson, S. L. Structural basis for Parkinson's Disease-linked LRRK2's binding to microtubules. 2022.01.21.477284 (2022). doi:10.1101/2022.01.21.477284

62. Marín, I., van Egmond, W. N. & van Haastert, P. J. M. The Roco protein family: a functional perspective. *FASEB J* 22, 3103–3110 (2008).

63. Zimprich, A., Biskup, S., Leitner, P., Lichtner, P., Farrer, M., Lincoln, S., Kachergus, J., Hulihan, M., Uitti, R. J., Calne, D. B., Stoessl, A. J., Pfeiffer, R. F., Patenge, N., Carbajal, I. C., Vieregge, P., Asmus, F., Müller-Myhsok, B., Dickson, D. W., Meitinger, T., Strom, T. M., Wszolek, Z. K. & Gasser, T. Mutations in LRRK2 Cause Autosomal-Dominant Parkinsonism with Pleomorphic Pathology. *Neuron* 44, 601–607 (2004).

64. Paisán-Ruíz, C., Jain, S., Evans, E. W., Gilks, W. P., Simón, J., van der Brug, M., de Munain, A. L., Aparicio, S., Gil, A. M., Khan, N., Johnson, J., Martinez, J. R., Nicholl, D., Carrera, I. M., Peňa, A. S., de Silva, R., Lees, A., Martí-Massó, J. F., Pérez-Tur, J., Wood, N. W. & Singleton, A. B. Cloning of the Gene Containing Mutations that Cause PARK8-Linked Parkinson's Disease. *Neuron* 44, 595–600 (2004).

65. Dodson, M. W., Zhang, T., Jiang, C., Chen, S. & Guo, M. Roles of the Drosophila LRRK2 homolog in Rab7-dependent lysosomal positioning. *Hum Mol Genet* 21, 1350–1363 (2012).

66. Manzoni, C., Mamais, A., Dihanich, S., McGoldrick, P., Devine, M. J., Zerle, J., Kara, E., Taanman, J.-W., Healy, D. G., Marti-Masso, J.-F., Schapira, A. H., Plun-Favreau, H., Tooze, S., Hardy, J., Bandopadhyay, R. & Lewis, P. A. Pathogenic Parkinson's disease mutations across the functional domains of LRRK2 alter the autophagic/lysosomal response to starvation. *Biochem Biophys Res Commun* 441, 862–866 (2013).

67. Orenstein, S. J., Kuo, S.-H., Tasset, I., Arias, E., Koga, H., Fernandez-Carasa, I., Cortes, E., Honig, L. S., Dauer, W., Consiglio, A., Raya, A., Sulzer, D. & Cuervo, A. M. Interplay of LRRK2 with chaperone-mediated autophagy. *Nat Neurosci* 16, 394–406 (2013).

68. Godena, V. K., Brookes-Hocking, N., Moller, A., Shaw, G., Oswald, M., Sancho, R. M., Miller, C. C. J., Whitworth, A. J. & De Vos, K. J. Increasing microtubule acetylation rescues axonal transport and locomotor deficits caused by LRRK2 Roc-COR domain mutations. *Nat Commun* 5, 5245 (2014).

69. Hsieh, C.-H., Shaltouki, A., Gonzalez, A. E., Bettencourt da Cruz, A., Burbulla, L. F., St Lawrence, E., Schüle, B., Krainc, D., Palmer, T. D. & Wang, X. Functional Impairment in Miro Degradation and Mitophagy Is a Shared Feature in Familial and Sporadic Parkinson's Disease. *Cell Stem Cell* 19, 709–724 (2016).

70. Blanca Ramírez, M., Lara Ordóñez, A. J., Fdez, E. & Hilfiker, S. LRRK2: from kinase to GTPase to microtubules and back. *Biochemical Society Transactions* 45, 141–146 (2017).

71. Schmidt, S. H., Weng, J.-H., Aoto, P. C., Boassa, D., Mathea, S., Silletti, S., Hu, J., Wallbott, M., Komives, E. A., Knapp, S., Herberg, F. W. & Taylor, S. S. Conformation and dynamics of the kinase domain drive subcellular location and activation of LRRK2. *Proc Natl Acad Sci U S A* 118, e2100844118 (2021).

72. Gandhi, P. N., Wang, X., Zhu, X., Chen, S. G. & Wilson-Delfosse, A. L. The Roc domain of leucine-rich repeat kinase 2 is sufficient for interaction with microtubules. *J Neurosci Res* 86, 1711–1720 (2008).

73. Wang, Y., Huynh, W., Skokan, T. D., Lu, W., Weiss, A. & Vale, R. D. CRACR2a is a calcium-activated dynein adaptor protein that regulates endocytic traffic. *J Cell Biol* 218, 1619–1633 (2019).

74. Etoh, K. & Fukuda, M. Rab10 regulates tubular endosome formation through KIF13A and KIF13B motors. *J Cell Sci* 132, jcs226977 (2019).

75. Niwa, S., Tanaka, Y. & Hirokawa, N. KIF1Bβ- and KIF1A-mediated axonal transport of presynaptic regulator Rab3 occurs in a GTP-dependent manner through DENN/MADD. *Nat Cell Biol* 10, 1269–1279 (2008).

76. Christensen, J. R., Kendrick, A. A., Truong, J. B., Aguilar-Maldonado, A., Adani, V., Dzieciatkowska, M. & Reck-Peterson, S. L. Cytoplasmic dynein-1 cargo diversity is mediated by the combinatorial assembly of FTS-Hook-FHIP complexes. *Elife* 10, e74538 (2021).

77. Tunyasuvunakool, K., Adler, J., Wu, Z., Green, T., Zielinski, M., Žídek, A., Bridgland, A., Cowie, A., Meyer, C., Laydon, A., Velankar, S., Kleywegt, G. J., Bateman, A., Evans, R., Pritzel, A., Figurnov, M., Ronneberger, O., Bates, R., Kohl, S. A. A., Potapenko, A., Ballard, A. J., Romera-Paredes, B., Nikolov, S., Jain, R., Clancy, E., Reiman, D., Petersen, S., Senior, A. W., Kavukcuoglu, K., Birney, E., Kohli, P., Jumper, J. & Hassabis, D. Highly accurate protein structure prediction for the human proteome. *Nature* 596, 590–596 (2021).

78. Jumper, J., Evans, R., Pritzel, A., Green, T., Figurnov, M., Ronneberger, O., Tunyasuvunakool, K., Bates, R., Žídek, A., Potapenko, A., Bridgland, A., Meyer, C., Kohl, S. A. A., Ballard, A. J., Cowie, A., Romera-Paredes, B., Nikolov, S., Jain, R., Adler, J., Back, T.,

Petersen, S., Reiman, D., Clancy, E., Zielinski, M., Steinegger, M., Pacholska, M., Berghammer, T., Bodenstein, S., Silver, D., Vinyals, O., Senior, A. W., Kavukcuoglu, K., Kohli, P. & Hassabis, D. Highly accurate protein structure prediction with AlphaFold. *Nature* 596, 583–589 (2021).

79. Janke, C. & Magiera, M. M. The tubulin code and its role in controlling microtubule properties and functions. *Nat Rev Mol Cell Biol* 21, 307–326 (2020).

80. Serrano, L., Avila, J. & Maccioni, R. B. Controlled proteolysis of tubulin by subtilisin: localization of the site for MAP2 interaction. *Biochemistry* 23, 4675–4681 (1984).

81. Civiero, L. & Bubacco, L. Human leucine-rich repeat kinase 1 and 2: intersecting or unrelated functions? *Biochem Soc Trans* 40, 1095–1101 (2012).

82. Howaldt, A., Hennig, A. F., Rolvien, T., Rössler, U., Stelzer, N., Knaus, A., Böttger, S., Zustin, J., Geißler, S., Oheim, R., Amling, M., Howaldt, H.-P. & Kornak, U. Adult Osteosclerotic Metaphyseal Dysplasia With Progressive Osteonecrosis of the Jaws and Abnormal Bone Resorption Pattern Due to a LRRK1 Splice Site Mutation. *J Bone Miner Res* 35, 1322–1332 (2020).

83. Miryounesi, M., Nikfar, A., Changi-Ashtiani, M., Shahrooei, M., Dinmohammadi, H., Shahani, T., Zarvandi, S., Bahrami, T., Momenilandi, M. & Rokni-Zadeh, H. A novel homozygous LRRK1 stop gain mutation in a patient suspected with osteosclerotic metaphyseal dysplasia. *Annals of Human Genetics* 84, 102–106 (2020).

84. Guo, L., Girisha, K. M., Iida, A., Hebbar, M., Shukla, A., Shah, H., Nishimura, G., Matsumoto, N., Nismath, S., Miyake, N. & Ikegawa, S. Identification of a novel LRRK1 mutation in a family with osteosclerotic metaphyseal dysplasia. *J Hum Genet* 62, 437–441 (2017).

85. Iida, A., Xing, W., Docx, M. K. F., Nakashima, T., Wang, Z., Kimizuka, M., Van Hul, W., Rating, D., Spranger, J., Ohashi, H., Miyake, N., Matsumoto, N., Mohan, S., Nishimura, G., Mortier, G. & Ikegawa, S. Identification of biallelic LRRK1 mutations in osteosclerotic metaphyseal dysplasia and evidence for locus heterogeneity. *J Med Genet* 53, 568–574 (2016).

86. Masuzugawa, S., Nishioka, K., Imai, Y., Ogata, J., Shojima, Y., Li, Y., Yoshino, H. & Hattori, N. A novel rare variant of LRRK2 associated with familial Parkinson's disease: p.R1501W. *Parkinsonism & Related Disorders* 76, 46–48 (2020).

87. Ryan, K. J., White, C. C., Patel, K., Xu, J., Olah, M., Replogle, J. M., Frangieh, M., Cimpean, M., Winn, P., McHenry, A., Kaskow, B. J., Chan, G., Cuerdon, N., Bennett, D. A., Boyd, J. D., Imitola, J., Elyaman, W., De Jager, P. L. & Bradshaw, E. M. A human microglia-like cellular model for assessing the effects of neurodegenerative disease gene variants. *Sci Transl Med* 9, eaai7635 (2017).

88. Atashrazm, F., Hammond, D., Perera, G., Bolliger, M. F., Matar, E., Halliday, G. M., Schüle, B., Lewis, S. J. G., Nichols, R. J. & Dzamko, N. LRRK2-mediated Rab10 phosphorylation in immune cells from Parkinson's disease patients. *Movement Disorders* 34, 406–415 (2019).

89. Cook, D. A., Kannarkat, G. T., Cintron, A. F., Butkovich, L. M., Fraser, K. B., Chang, J., Grigoryan, N., Factor, S. A., West, A. B., Boss, J. M. & Tansey, M. G. LRRK2 levels in immune cells are increased in Parkinson's disease. *NPJ Parkinsons Dis* 3, 11 (2017).

90. Bonifacino, J. S. & Neefjes, J. Moving and positioning the endolysosomal system. *Curr Opin Cell Biol* 47, 1–8 (2017).

91. Kruppa, A. J. & Buss, F. Motor proteins at the mitochondria-cytoskeleton interface. *J Cell Sci* 134, jcs226084 (2021).

92. Reck-Peterson, S. L., Redwine, W. B., Vale, R. D. & Carter, A. P. The cytoplasmic dynein transport machinery and its many cargoes. *Nat Rev Mol Cell Biol* 19, 382–398 (2018).

93. Boecker, C. A., Goldsmith, J., Dou, D., Cajka, G. G. & Holzbaur, E. L. F. Increased LRRK2 kinase activity alters neuronal autophagy by disrupting the axonal transport of autophagosomes. *Curr Biol* 31, 2140-2154.e6 (2021).

94. Boecker, C. A. & Holzbaur, E. L. F. Hyperactive LRRK2 kinase impairs the trafficking of axonal autophagosomes. *Autophagy* 17, 2043–2045 (2021).

95. Rzomp, K. A., Scholtes, L. D., Briggs, B. J., Whittaker, G. R. & Scidmore, M. A. Rab GTPases are recruited to chlamydial inclusions in both a species-dependent and species-independent manner. *Infect Immun* 71, 5855–5870 (2003).

96. Woehlke, G., Ruby, A. K., Hart, C. L., Ly, B., Hom-Booher, N. & Vale, R. D. Microtubule interaction site of the kinesin motor. *Cell* 90, 207–216 (1997).

97. Redwine, W. B., DeSantis, M. E., Hollyer, I., Htet, Z. M., Tran, P. T., Swanson, S. K., Florens, L., Washburn, M. P. & Reck-Peterson, S. L. The human cytoplasmic dynein interactome reveals novel activators of motility. *Elife* 6, e28257 (2017).

98. Suloway, C., Pulokas, J., Fellmann, D., Cheng, A., Guerra, F., Quispe, J., Stagg, S., Potter, C. S. & Carragher, B. Automated molecular microscopy: The new Leginon system. *Journal of Structural Biology* 151, 41–60 (2005).

99. Zheng, S. Q., Palovcak, E., Armache, J.-P., Verba, K. A., Cheng, Y. & Agard, D. A. MotionCor2: anisotropic correction of beam-induced motion for improved cryo-electron microscopy. *Nat Methods* 14, 331–332 (2017).

100. Rohou, A. & Grigorieff, N. CTFFIND4: Fast and accurate defocus estimation from electron micrographs. *J Struct Biol* 192, 216–221 (2015).

101. Zivanov, J., Nakane, T., Forsberg, B. O., Kimanius, D., Hagen, W. J., Lindahl, E. & Scheres, S. H. New tools for automated high-resolution cryo-EM structure determination in RELION-3. *Elife* 7, e42166 (2018).

102. Cook, A. D., Manka, S. W., Wang, S., Moores, C. A. & Atherton, J. A microtubule RELION-based pipeline for cryo-EM image processing. *J Struct Biol* 209, 107402 (2020).

103. Punjani, A. & Fleet, D. J. 3D variability analysis: Resolving continuous flexibility and discrete heterogeneity from single particle cryo-EM. *J Struct Biol* 213, 107702 (2021).

104. Wagner, T., Merino, F., Stabrin, M., Moriya, T., Antoni, C., Apelbaum, A., Hagel, P., Sitsel, O., Raisch, T., Prumbaum, D., Quentin, D., Roderer, D., Tacke, S., Siebolds, B., Schubert, E., Shaikh, T. R., Lill, P., Gatsogiannis, C. & Raunser, S. SPHIRE-crYOLO is a fast and accurate fully automated particle picker for cryo-EM. *Commun Biol* 2, 218 (2019).

105. Waterhouse, A., Bertoni, M., Bienert, S., Studer, G., Tauriello, G., Gumienny, R., Heer, F. T., de Beer, T. A. P., Rempfer, C., Bordoli, L., Lepore, R. & Schwede, T. SWISS-MODEL: homology modelling of protein structures and complexes. *Nucleic Acids Res* 46, W296–W303 (2018).

106. Pettersen, E. F., Goddard, T. D., Huang, C. C., Meng, E. C., Couch, G. S., Croll, T. I., Morris, J. H. & Ferrin, T. E. UCSF ChimeraX: Structure visualization for researchers, educators, and developers. *Protein Sci* 30, 70–82 (2021).

107. Roberts, A. J., Goodman, B. S. & Reck-Peterson, S. L. Reconstitution of dynein transport to the microtubule plus end by kinesin. *eLife* 3, e02641 (2014).

108. Lis, P., Burel, S., Steger, M., Mann, M., Brown, F., Diez, F., Tonelli, F., Holton, J. L., Ho, P. W., Ho, S.-L., Chou, M.-Y., Polinski, N. K., Martinez, T. N., Davies, P. & Alessi, D. R. Development of phospho-specific Rab protein antibodies to monitor in vivo activity of the LRRK2 Parkinson's disease kinase. *Biochem J* 475, 1–22 (2018).

109. Waterhouse, A. M., Procter, J. B., Martin, D. M. A., Clamp, M. & Barton, G. J. Jalview Version 2--a multiple sequence alignment editor and analysis workbench. *Bioinformatics* 25, 1189–1191 (2009).

110. Beylina, A., Langston, R. G., Rosen, D., Reed, X. & Cookson, M. R. Generation of fourteen isogenic cell lines for Parkinson's disease-associated leucine-rich repeat kinase (LRRK2). *Stem Cell Research* 53, 102354 (2021).

111. Roux, K. J., Kim, D. I., Raida, M. & Burke, B. A promiscuous biotin ligase fusion protein identifies proximal and interacting proteins in mammalian cells. *J Cell Biol* 196, 801–810 (2012).

112. Kim, D. I., Birendra, K. C., Zhu, W., Motamedchaboki, K., Doye, V. & Roux, K. J. Probing nuclear pore complex architecture with proximity-dependent biotinylation. *Proc Natl Acad Sci U S A* 111, E2453-2461 (2014).

113. Roberts, A. W., Popov, L. M., Mitchell, G., Ching, K. L., Licht, D. J., Golovkine, G., Barton, G. M. & Cox, J. S. Cas9+ conditionally-immortalized macrophages as a tool for bacterial pathogenesis and beyond. *eLife* 8, e45957 (2019).

114. Beilina, A., Rudenko, I. N., Kaganovich, A., Civiero, L., Chau, H., Kalia, S. K., Kalia, L. V., Lobbestael, E., Chia, R., Ndukwe, K., Ding, J., Nalls, M. A., Consortium, I. P. D. G., Consortium, N. A. B. E., Olszewski, M., Hauser, D. N., Kumaran, R., Lozano, A. M., Baekelandt, V., Greene, L. E., Taymans, J.-M., Greggio, E. & Cookson, M. R. Unbiased screen for interactors of leucine-rich repeat kinase 2 supports a common pathway for sporadic and familial Parkinson disease. *PNAS* 111, 2626–2631 (2014).

115. MacLeod, D. A., Rhinn, H., Kuwahara, T., Zolin, A., Di Paolo, G., McCabe, B. D., Marder, K. S., Honig, L. S., Clark, L. N., Small, S. A. & Abeliovich, A. RAB7L1 Interacts with LRRK2 to

Modify Intraneuronal Protein Sorting and Parkinson's Disease Risk. *Neuron* 77, 425–439 (2013).

116. Minoura, I., Hachikubo, Y., Yamakita, Y., Takazaki, H., Ayukawa, R., Uchimura, S. & Muto, E. Overexpression, purification, and functional analysis of recombinant human tubulin dimer. *FEBS Lett* 587, 3450–3455 (2013).

117. Manning, G., Whyte, D. B., Martinez, R., Hunter, T. & Sudarsanam, S. The Protein Kinase Complement of the Human Genome. *Science* 298, 1912–1934 (2002).

118. Monfrini, E. & Di Fonzo, A. in *Leucine-Rich Repeat Kinase 2 (LRRK2)* (ed. Rideout, H. J.) 3–30 (Springer International Publishing, 2017). doi:10.1007/978-3-319-49969-7_1

119. Maio, R. D., Hoffman, E. K., Rocha, E. M., Keeney, M. T., Sanders, L. H., Miranda, B. R. D., Zharikov, A., Laar, A. V., Stepan, A. F., Lanz, T. A., Kofler, J. K., Burton, E. A., Alessi, D. R., Hastings, T. G. & Greenamyre, J. T. LRRK2 activation in idiopathic Parkinson's disease. *Science Translational Medicine* 10, (2018).

120. Taylor, M. & Alessi, D. R. Advances in elucidating the function of leucine-rich repeat protein kinase-2 in normal cells and Parkinson's disease. *Current Opinion in Cell Biology* 63, 102–113 (2020).

121. Xing, W., Liu, J., Cheng, S., Vogel, P., Mohan, S. & Brommage, R. Targeted disruption of leucine-rich repeat kinase 1 but not leucine-rich repeat kinase 2 in mice causes severe osteopetrosis. *Journal of Bone and Mineral Research* 28, 1962–1974 (2013).

122. Brommage, R., Liu, J., Hansen, G. M., Kirkpatrick, L. L., Potter, D. G., Sands, A. T., Zambrowicz, B., Powell, D. R. & Vogel, P. High-throughput screening of mouse gene knockouts identifies established and novel skeletal phenotypes. *Bone Research* 2, 1–30 (2014).

123. Weedon, M. N., Hastings, R., Caswell, R., Xie, W., Paszkiewicz, K., Antoniadi, T., Williams, M., King, C., Greenhalgh, L., Newbury-Ecob, R. & Ellard, S. Exome sequencing identifies a DYNC1H1 mutation in a large pedigree with dominant axonal Charcot-Marie-Tooth disease. *Am. J. Hum. Genet.* 89, 308–312 (2011).

124. Jamuar, S. S., Lam, A.-T. N., Kircher, M., D'Gama, A. M., Wang, J., Barry, B. J., Zhang, X., Hill, R. S., Partlow, J. N., Rozzo, A., Servattalab, S., Mehta, B. K., Topcu, M., Amrom, D., Andermann, E., Dan, B., Parrini, E., Guerrini, R., Scheffer, I. E., Berkovic, S. F., Leventer, R. J., Shen, Y., Wu, B. L., Barkovich, A. J., Sahin, M., Chang, B. S., Bamshad, M., Nickerson, D. A., Shendure, J., Poduri, A., Yu, T. W. & Walsh, C. A. Somatic mutations in cerebral cortical malformations. *N. Engl. J. Med.* 371, 733–743 (2014).

125. Harms, M. B., Ori-McKenney, K. M., Scoto, M., Tuck, E. P., Bell, S., Ma, D., Masi, S., Allred, P., Al-Lozi, M., Reilly, M. M., Miller, L. J., Jani-Acsadi, A., Pestronk, A., Shy, M. E., Muntoni, F., Vallee, R. B. & Baloh, R. H. Mutations in the tail domain of DYNC1H1 cause dominant spinal muscular atrophy. *Neurology* 78, 1714–1720 (2012).

126. Peeters, K., Litvinenko, I., Asselbergh, B., Almeida-Souza, L., Chamova, T., Geuens, T., Ydens, E., Zimoń, M., Irobi, J., De Vriendt, E., De Winter, V., Ooms, T., Timmerman, V., Tournev, I. & Jordanova, A. Molecular defects in the motor adaptor BICD2 cause proximal

spinal muscular atrophy with autosomal-dominant inheritance. *Am. J. Hum. Genet.* 92, 955–964 (2013).

127. Farrer, M. J., Hulihan, M. M., Kachergus, J. M., Dächsel, J. C., Stoessl, A. J., Grantier, L. L., Calne, S., Calne, D. B., Lechevalier, B., Chapon, F., Tsuboi, Y., Yamada, T., Gutmann, L., Elibol, B., Bhatia, K. P., Wider, C., Vilariño-Güell, C., Ross, O. A., Brown, L. A., Castanedes-Casey, M., Dickson, D. W. & Wszolek, Z. K. DCTN1 mutations in Perry syndrome. *Nat. Genet.* 41, 163–165 (2009).

128. Araki, E., Tsuboi, Y., Daechsel, J., Milnerwood, A., Vilarino-Guell, C., Fujii, N., Mishima, T., Oka, T., Hara, H., Fukae, J. & Farrer, M. J. A novel DCTN1 mutation with late-onset parkinsonism and frontotemporal atrophy. *Mov. Disord.* 29, 1201–1204 (2014).

129. Ebneth, A., Godemann, R., Stamer, K., Illenberger, S., Trinczek, B., Mandelkow, E.-M. & Mandelkow, E. Overexpression of Tau Protein Inhibits Kinesin-dependent Trafficking of Vesicles, Mitochondria, and Endoplasmic Reticulum: Implications for Alzheimer's Disease. *J Cell Biol* 143, 777–794 (1998).

130. Semenova, I., Ikeda, K., Resaul, K., Kraikivski, P., Aguiar, M., Gygi, S., Zaliapin, I., Cowan, A. & Rodionov, V. Regulation of microtubule-based transport by MAP4. *Mol Biol Cell* 25, 3119–3132 (2014).

131. McKenney, R. J., Huynh, W., Tanenbaum, M. E., Bhabha, G. & Vale, R. D. Activation of cytoplasmic dynein motility by dynactin-cargo adapter complexes. *Science* 345, 337–341 (2014).

132. Schlager, M. A., Hoang, H. T., Urnavicius, L., Bullock, S. L. & Carter, A. P. In vitro reconstitution of a highly processive recombinant human dynein complex. *EMBO J.* 33, 1855–1868 (2014).

133. Schroer, T. A. Dynactin. *Annu. Rev. Cell Dev. Biol.* 20, 759–779 (2004).

134. Hendricks, A. G., Perlson, E., Ross, J. L., Schroeder, H. W., Tokito, M. & Holzbaur, E. L. F. Motor coordination via a tug-of-war mechanism drives bidirectional vesicle transport. *Curr Biol* 20, 697–702 (2010).

135. Barkus, R. V., Klyachko, O., Horiuchi, D., Dickson, B. J. & Saxton, W. M. Identification of an axonal kinesin-3 motor for fast anterograde vesicle transport that facilitates retrograde transport of neuropeptides. *Mol Biol Cell* 19, 274–283 (2008).

136. Schlager, M. A., Kapitein, L. C., Grigoriev, I., Burzynski, G. M., Wulf, P. S., Keijzer, N., de Graaff, E., Fukuda, M., Shepherd, I. T., Akhmanova, A. & Hoogenraad, C. C. Pericentrosomal targeting of Rab6 secretory vesicles by Bicaudal-D-related protein 1 (BICDR-1) regulates neuritogenesis. *EMBO J* 29, 1637–1651 (2010).

137. Maday, S., Wallace, K. E. & Holzbaur, E. L. F. Autophagosomes initiate distally and mature during transport toward the cell soma in primary neurons. *J Cell Biol* 196, 407–417 (2012).

138. Schlager, M. A. & Hoogenraad, C. C. Basic mechanisms for recognition and transport of synaptic cargos. *Mol Brain* 2, 25 (2009).

139. Gross, S. P., Welte, M. A., Block, S. M. & Wieschaus, E. F. Coordination of opposite-polarity microtubule motors. *J Cell Biol* 156, 715–724 (2002).

140. Vale, R. D. The molecular motor toolbox for intracellular transport. *Cell* 112, 467–480 (2003).

141. Hirokawa, N. & Noda, Y. Intracellular transport and kinesin superfamily proteins, KIFs: structure, function, and dynamics. *Physiol Rev* 88, 1089–1118 (2008).

142. Abenza, J. F., Pantazopoulou, A., Rodríguez, J. M., Galindo, A. & Peñalva, M. A. Long-Distance Movement of Aspergillus nidulans Early Endosomes on Microtubule Tracks. *Traffic* 10, 57–75 (2009).

143. Egan, M. J., Tan, K. & Reck-Peterson, S. L. Lis1 is an initiation factor for dynein-driven organelle transport. *J Cell Biol* 197, 971–982 (2012).

144. Wedlich-Söldner, R., Straube, A., Friedrich, M. W. & Steinberg, G. A balance of KIF1A-like kinesin and dynein organizes early endosomes in the fungus Ustilago maydis. *EMBO J* 21, 2946–2957 (2002).

145. Baumann, S., Pohlmann, T., Jungbluth, M., Brachmann, A. & Feldbrügge, M. Kinesin-3 and dynein mediate microtubule-dependent co-transport of mRNPs and endosomes. *J Cell Sci* 125, 2740–2752 (2012).

146. Guimaraes, S. C., Schuster, M., Bielska, E., Dagdas, G., Kilaru, S., Meadows, B. R. A., Schrader, M. & Steinberg, G. Peroxisomes, lipid droplets, and endoplasmic reticulum 'hitchhike' on motile early endosomes. *J Cell Biol* 211, 945–954 (2015).

147. Salogiannis, J., Egan, M. J. & Reck-Peterson, S. L. Peroxisomes move by hitchhiking on early endosomes using the novel linker protein PxdA. *J Cell Biol* 212, 289–296 (2016).

148. Encalada, S. E., Szpankowski, L., Xia, C. & Goldstein, L. S. B. Stable kinesin and dynein assemblies drive the axonal transport of mammalian prion protein vesicles. *Cell* 144, 551–565 (2011).

149. Kamal, A., Stokin, G. B., Yang, Z., Xia, C. H. & Goldstein, L. S. Axonal transport of amyloid precursor protein is mediated by direct binding to the kinesin light chain subunit of kinesin-I. *Neuron* 28, 449–459 (2000).

150. Rogers, S. L., Tint, I. S., Fanapour, P. C. & Gelfand, V. I. Regulated bidirectional motility of melanophore pigment granules along microtubules in vitro. *Proc Natl Acad Sci U S A* 94, 3720–3725 (1997).

151. Brendza, R. P., Serbus, L. R., Saxton, W. M. & Duffy, J. B. Posterior localization of dynein and dorsal-ventral axis formation depend on kinesin in Drosophila oocytes. *Curr Biol* 12, 1541–1545 (2002).

152. Carvalho, P., Gupta, M. L., Hoyt, M. A. & Pellman, D. Cell cycle control of kinesin-mediated transport of Bik1 (CLIP-170) regulates microtubule stability and dynein activation. *Dev Cell* 6, 815–829 (2004).

153. Twelvetrees, A. E., Pernigo, S., Sanger, A., Guedes-Dias, P., Schiavo, G., Steiner, R. A., Dodding, M. P. & Holzbaur, E. L. F. The Dynamic Localization of Cytoplasmic Dynein in Neurons Is Driven by Kinesin-1. *Neuron* 90, 1000–1015 (2016).

154. Zhang, J., Li, S., Fischer, R. & Xiang, X. Accumulation of cytoplasmic dynein and dynactin at microtubule plus ends in Aspergillus nidulans is kinesin dependent. *Mol Biol Cell* 14, 1479–1488 (2003).

155. Derr, N. D., Goodman, B. S., Jungmann, R., Leschziner, A. E., Shih, W. M. & Reck-Peterson, S. L. Tug-of-war in motor protein ensembles revealed with a programmable DNA origami scaffold. *Science* 338, 662–665 (2012).

156. Belyy, V., Schlager, M. A., Foster, H., Reimer, A. E., Carter, A. P. & Yildiz, A. The mammalian dynein-dynactin complex is a strong opponent to kinesin in a tug-of-war competition. *Nat Cell Biol* 18, 1018–1024 (2016).

157. Moore, J. K., Stuchell-Brereton, M. D. & Cooper, J. A. Function of dynein in budding yeast: mitotic spindle positioning in a polarized cell. *Cell Motil Cytoskeleton* 66, 546–555 (2009).

158. DeSantis, M. E., Cianfrocco, M. A., Htet, Z. M., Tran, P. T., Reck-Peterson, S. L. & Leschziner, A. E. Lis1 Has Two Opposing Modes of Regulating Cytoplasmic Dynein. *Cell* 170, 1197-1208.e12 (2017).

159. Olenick, M. A. & Holzbaur, E. L. F. Dynein activators and adaptors at a glance. *J Cell Sci* 132, jcs227132 (2019).

160. Dorner, C., Ciossek, T., Müller, S., Møller, P. H., Ullrich, A. & Lammers, R. Characterization of KIF1C, a new kinesin-like protein involved in vesicle transport from the Golgi apparatus to the endoplasmic reticulum. *J Biol Chem* 273, 20267–20275 (1998).

161. Rogers, K. R., Weiss, S., Crevel, I., Brophy, P. J., Geeves, M. & Cross, R. KIF1D is a fast non-processive kinesin that demonstrates novel K-loop-dependent mechanochemistry. *EMBO J* 20, 5101–5113 (2001).

162. Theisen, U., Straube, E. & Straube, A. Directional persistence of migrating cells requires Kif1C-mediated stabilization of trailing adhesions. *Dev Cell* 23, 1153–1166 (2012).

163. Novarino, G., Fenstermaker, A. G., Zaki, M. S., Hofree, M., Silhavy, J. L., Heiberg, A. D., Abdellateef, M., Rosti, B., Scott, E., Mansour, L., Masri, A., Kayserili, H., Al-Aama, J. Y., Abdel-Salam, G. M. H., Karminejad, A., Kara, M., Kara, B., Bozorgmehri, B., Ben-Omran, T., Mojahedi, F., El Din Mahmoud, I. G., Bouslam, N., Bouhouche, A., Benomar, A., Hanein, S., Raymond, L., Forlani, S., Mascaro, M., Selim, L., Shehata, N., Al-Allawi, N., Bindu, P. S., Azam, M., Gunel, M., Caglayan, A., Bilguvar, K., Tolun, A., Issa, M. Y., Schroth, J., Spencer, E. G., Rosti, R. O., Akizu, N., Vaux, K. K., Johansen, A., Koh, A. A., Megahed, H., Durr, A., Brice, A., Stevanin, G., Gabriel, S. B., Ideker, T. & Gleeson, J. G. Exome sequencing links corticospinal motor neuron disease to common neurodegenerative disorders. *Science* 343, 506–511 (2014).

164. Splinter, D., Tanenbaum, M. E., Lindqvist, A., Jaarsma, D., Flotho, A., Yu, K. L., Grigoriev, I., Engelsma, D., Haasdijk, E. D., Keijzer, N., Demmers, J., Fornerod, M., Melchior, F., Hoogenraad, C. C., Medema, R. H. & Akhmanova, A. Bicaudal D2, dynein, and kinesin-1

associate with nuclear pore complexes and regulate centrosome and nuclear positioning during mitotic entry. *PLoS Biol* 8, e1000350 (2010).

165. Miki, H., Okada, Y. & Hirokawa, N. Analysis of the kinesin superfamily: insights into structure and function. *Trends Cell Biol* 15, 467–476 (2005).

166. Behrends, C., Sowa, M. E., Gygi, S. P. & Harper, J. W. Network organization of the human autophagy system. *Nature* 466, 68–76 (2010).

167. Zhang, Y., Wen, Z., Washburn, M. P. & Florens, L. Refinements to label free proteome quantitation: how to deal with peptides shared by multiple proteins. *Anal Chem* 82, 2272–2281 (2010).

168. Xu, L., Sowa, M. E., Chen, J., Li, X., Gygi, S. P. & Harper, J. W. An FTS/Hook/p107(FHIP) complex interacts with and promotes endosomal clustering by the homotypic vacuolar protein sorting complex. *Mol Biol Cell* 19, 5059–5071 (2008).

169. Olenick, M. A., Tokito, M., Boczkowska, M., Dominguez, R. & Holzbaur, E. L. F. Hook Adaptors Induce Unidirectional Processive Motility by Enhancing the Dynein-Dynactin Interaction. *J Biol Chem* 291, 18239–18251 (2016).

170. Hoogenraad, C. C., Akhmanova, A., Howell, S. A., Dortland, B. R., De Zeeuw, C. I., Willemsen, R., Visser, P., Grosveld, F. & Galjart, N. Mammalian Golgi-associated Bicaudal-D2 functions in the dynein-dynactin pathway by interacting with these complexes. *EMBO J* 20, 4041–4054 (2001).

171. Stuurman, N., Häner, M., Sassea, B., Hübner, W., Suterd, B. & Aebi, U. Interactions between coiled-coil proteins: Drosophila lamin Dm0 binds to the Bicaudal-D protein. *European Journal of Cell Biology* 78, 278–287 (1999).

172. Schroeder, C. M. & Vale, R. D. Assembly and activation of dynein-dynactin by the cargo adaptor protein Hook3. *J Cell Biol* 214, 309–318 (2016).

173. Friedman, D. S. & Vale, R. D. Single-molecule analysis of kinesin motility reveals regulation by the cargo-binding tail domain. *Nat Cell Biol* 1, 293–297 (1999).

174. Hackney, D. D. & Stock, M. F. Kinesin's IAK tail domain inhibits initial microtubule-stimulated ADP release. *Nat Cell Biol* 2, 257–260 (2000).

175. Stock, M. F., Guerrero, J., Cobb, B., Eggers, C. T., Huang, T. G., Li, X. & Hackney, D. D. Formation of the compact confomer of kinesin requires a COOH-terminal heavy chain domain and inhibits microtubule-stimulated ATPase activity. *J Biol Chem* 274, 14617–14623 (1999).

176. Farkhondeh, A., Niwa, S., Takei, Y. & Hirokawa, N. Characterizing KIF16B in neurons reveals a novel intramolecular 'stalk inhibition' mechanism that regulates its capacity to potentiate the selective somatodendritic localization of early endosomes. *J Neurosci* 35, 5067–5086 (2015).

177. Hammond, J. W., Cai, D., Blasius, T. L., Li, Z., Jiang, Y., Jih, G. T., Meyhofer, E. & Verhey, K. J. Mammalian Kinesin-3 motors are dimeric in vivo and move by processive motility upon release of autoinhibition. *PLoS Biol* 7, e72 (2009).

178. Yamada, K. H., Hanada, T. & Chishti, A. H. The effector domain of human Dlg tumor suppressor acts as a switch that relieves autoinhibition of kinesin-3 motor GAKIN/KIF13B. *Biochemistry* 46, 10039–10045 (2007).

179. Hornbeck, P. V., Zhang, B., Murray, B., Kornhauser, J. M., Latham, V. & Skrzypek, E. PhosphoSitePlus, 2014: mutations, PTMs and recalibrations. *Nucleic Acids Res* 43, D512-520 (2015).

180. Lee, I.-G., Olenick, M. A., Boczkowska, M., Franzini-Armstrong, C., Holzbaur, E. L. F. & Dominguez, R. A conserved interaction of the dynein light intermediate chain with dynein-dynactin effectors necessary for processivity. *Nat Commun* 9, 986 (2018).

181. Urnavicius, L., Zhang, K., Diamant, A. G., Motz, C., Schlager, M. A., Yu, M., Patel, N. A., Robinson, C. V. & Carter, A. P. The structure of the dynactin complex and its interaction with dynein. *Science* 347, 1441–1446 (2015).

182. Siddiqui, N., Zwetsloot, A. J., Bachmann, A., Roth, D., Hussain, H., Brandt, J., Kaverina, I. & Straube, A. PTPN21 and Hook3 relieve KIF1C autoinhibition and activate intracellular transport. *Nat Commun* 10, 2693 (2019).

183. Efimova, N., Grimaldi, A., Bachmann, A., Frye, K., Zhu, X., Feoktistov, A., Straube, A. & Kaverina, I. Podosome-regulating kinesin KIF1C translocates to the cell periphery in a CLASP-dependent manner. *J Cell Sci* 127, 5179–5188 (2014).

184. Kopp, P., Lammers, R., Aepfelbacher, M., Woehlke, G., Rudel, T., Machuy, N., Steffen, W. & Linder, S. The kinesin KIF1C and microtubule plus ends regulate podosome dynamics in macrophages. *Mol Biol Cell* 17, 2811–2823 (2006).

185. Lee, P. L., Ohlson, M. B. & Pfeffer, S. R. Rab6 regulation of the kinesin family KIF1C motor domain contributes to Golgi tethering. *Elife* 4, (2015).

186. Lipka, J., Kapitein, L. C., Jaworski, J. & Hoogenraad, C. C. Microtubule-binding protein doublecortin-like kinase 1 (DCLK1) guides kinesin-3-mediated cargo transport to dendrites. *EMBO J* 35, 302–318 (2016).

187. Bielska, E., Schuster, M., Roger, Y., Berepiki, A., Soanes, D. M., Talbot, N. J. & Steinberg, G. Hook is an adapter that coordinates kinesin-3 and dynein cargo attachment on early endosomes. *J Cell Biol* 204, 989–1007 (2014).

188. Yao, X., Wang, X. & Xiang, X. FHIP and FTS proteins are critical for dynein-mediated transport of early endosomes in Aspergillus. *Mol Biol Cell* 25, 2181–2189 (2014).

189. Guo, X., Farías, G. G., Mattera, R. & Bonifacino, J. S. Rab5 and its effector FHF contribute to neuronal polarity through dynein-dependent retrieval of somatodendritic proteins from the axon. *Proc Natl Acad Sci U S A* 113, E5318-5327 (2016).

190. Zhang, J., Qiu, R., Arst, H. N., Peñalva, M. A. & Xiang, X. HookA is a novel dynein-early endosome linker critical for cargo movement in vivo. *J Cell Biol* 204, 1009–1026 (2014).

191. Blasius, T. L., Reed, N., Slepchenko, B. M. & Verhey, K. J. Recycling of kinesin-1 motors by diffusion after transport. *PLoS One* 8, e76081 (2013).

192. Dor, T., Cinnamon, Y., Raymond, L., Shaag, A., Bouslam, N., Bouhouche, A., Gaussen, M., Meyer, V., Durr, A., Brice, A., Benomar, A., Stevanin, G., Schuelke, M. & Edvardson, S. KIF1C mutations in two families with hereditary spastic paraparesis and cerebellar dysfunction. *J Med Genet* 51, 137–142 (2014).

193. Engelender, S., Sharp, A. H., Colomer, V., Tokito, M. K., Lanahan, A., Worley, P., Holzbaur, E. L. & Ross, C. A. Huntingtin-associated protein 1 (HAP1) interacts with the p150Glued subunit of dynactin. *Hum Mol Genet* 6, 2205–2212 (1997).

194. Li, S.-H., Gutekunst, C.-A., Hersch, S. M. & Li, X.-J. Interaction of Huntingtin-Associated Protein with Dynactin P150Glued. *J. Neurosci.* 18, 1261–1269 (1998).

195. Twelvetrees, A. E., Yuen, E. Y., Arancibia-Carcamo, I. L., MacAskill, A. F., Rostaing, P., Lumb, M. J., Humbert, S., Triller, A., Saudou, F., Yan, Z. & Kittler, J. T. Delivery of GABAARs to synapses is mediated by HAP1-KIF5 and disrupted by mutant huntingtin. *Neuron* 65, 53–65 (2010).

196. van Spronsen, M., Mikhaylova, M., Lipka, J., Schlager, M. A., van den Heuvel, D. J., Kuijpers, M., Wulf, P. S., Keijzer, N., Demmers, J., Kapitein, L. C., Jaarsma, D., Gerritsen, H. C., Akhmanova, A. & Hoogenraad, C. C. TRAK/Milton motor-adaptor proteins steer mitochondrial trafficking to axons and dendrites. *Neuron* 77, 485–502 (2013).

197. McWilliam, H., Li, W., Uludag, M., Squizzato, S., Park, Y. M., Buso, N., Cowley, A. P. & Lopez, R. Analysis Tool Web Services from the EMBL-EBI. *Nucleic Acids Res* 41, W597-600 (2013).

198. Biasini, M., Bienert, S., Waterhouse, A., Arnold, K., Studer, G., Schmidt, T., Kiefer, F., Gallo Cassarino, T., Bertoni, M., Bordoli, L. & Schwede, T. SWISS-MODEL: modelling protein tertiary and quaternary structure using evolutionary information. *Nucleic Acids Res* 42, W252-258 (2014).